Doctoral Dissertation
Doctoral Program in Mechanical Engineering (33° cycle)

Design of Additive Manufactured Structural Shells for Harsh Environment Probes

Enrico Ossola

* * * * *

Supervisors
Prof. Eugenio Brusa
Prof. Raffaella Sesana

Politecnico di Torino
July 22, 2021

I hereby declare that, the contents and organisation of this dissertation constitute my own original work and does not compromise in any way the rights of third parties, including those relating to the security of personal data.

....
Enrico Ossola
Turin, July 22, 2021

Summary

Design methodologies for complex systems, where multiple components are interacting together, or multi-physical phenomena are involved, are currently one of the most interesting field of study of Machine Design. Indeed, the development of new technologies and materials, together with improved predictive models and simulations tools, are bringing the industry to develop new, high performance products, designed to fulfill multiple functions, acting as systems rather than single components.

In this context, Additive Manufacturing represents one of the most disruptive technologies, not only because of the great design freedom offered by the novel fabrication processes, but also because of the new digital approach, involving the entire design and manufacturing process, starting from the digital Computer-Aided Design model and ending with the physical product. The novelty of the technology requires to re-think the design process, that has to evolve as an iterative process through the design, optimization, verification and validation steps, involving experimental testing at specimen, component, and system level.

Thermo-structural systems for special applications, such as the exploration of harsh environments, represent well suited candidates for investigating both the potential benefits of new technologies, and new design methodologies, starting from practical applications. The object of the study has been provided in a collaboration framework between the Department of Mechanical and Aerospace Engineering (`DIMEAS`) of Polytechnic of Torino (Italy), and the `NASA` Jet Propulsion Laboratory / California Institute of Technology, under the `JPL` Visiting Student Research Program and it is represented by a concept of a Venus surface lander.

The harsh environmental conditions of the surface of the planet pose unique challenges for both the structural and the thermal control systems, which need to withstand very high external pressures, up to 93 bar, and extreme temperatures, up to 462°C. Past landing missions used metallic spherical shells produced by conventional manufacturing techniques, such as spin forming, protected by insulating or phase change materials, to mitigate the effects of the extreme temperatures, for the duration of the mission. At that time, the fabrication techniques limited

the design freedom to simple geometries, such as plain shells, without internal ribbing systems. Since Additive Manufacturing has come to the fore, new design opportunities have become available. Novel concepts and architectures for Venus landing probes have recently been proposed by Jet Propulsion Laboratory, including integrated thermo-structural systems, in which thermal control devices, such as evaporators, are embedded within the primary structure, potentially resulting in a increased lifetime of the probe.

The present work has the objective to propose an Additive Manufactured lightweight layout for the primary structure of a concept of a Venus lander, in which a periodic pattern of stiffening ribs is used to improve the mechanical performance of the system. Moreover, a prototype for laboratory testing of the evaporator, to be embedded within the primary structure, has been structurally optimized, by recurring to lattice structure infill.

The complexity of the geometry of the primary structure under study, together with the extreme loading conditions and the uncertainties of the novel manufacturing processes, requires a modeling that starts with simple analytical and numerical tools, evolves through an optimization phase, and it involves experimental testing, aimed at the validation of the models. In this context, a novel analytical optimization method for isogrid-stiffened spherical shells has been developed and validated through an experimental campaign.

A preliminary activity on the evaporator, to be embedded within the structural shell, has been performed, working on a proof case for laboratory testing. A design methodology for optimizing the structure, based on structural and thermal requirements has been proposed, including experimental activities at specimen level, aimed to assess manufacturing limitations in fabricating small struts. Unfortunately, the research activities have been affected by Covid-19 events, and the planned experimental testing on the evaporator level has been delayed.

The challenging application provided the opportunity to study the potential benefits of Additive Manufacturing, and also to investigate design methodologies to fully exploit these benefits. The space field, together with the collaboration with the Jet Propulsion Laboratory, has proved to be an excellent testing ground, benefiting from a consolidated experience in system engineering and verification and validation processes.

Acknowledgements

Contents

List of Figures

XI

List of Tables

Chapter 1

Introduction

Among the methodological aspects of Mechanical Design, the development of systems deriving from the integration of interacting elements is currently object of research, especially when multi-physical phenomena or new materials are involved. In this context, space probes for the exploration of harsh environments, such as the surface of Venus, pose unique challenges, due to the simultaneous presence of very high external pressure loading and extreme temperatures.

New technologies, such as Additive Manufacturing, could open unprecedented opportunities, as they significantly extended the design freedom, enabling the fabrication of very complex geometries, as well as new architected materials. Potential benefits ranges from lightweight components with improved performances, to monolithic assemblies and multi-functional systems, as, for instance, structural shells with integrated cooling channels.

Design procedures shall be re-evaluated, to fully exploit the potential of the new technologies, shifting the focus from a component level to a system level.

1.1 The technical domain: Exploration of harsh environments in Space

Are we alone in the Universe? Since the last century, the progress in technology and space exploration has provided the means to scientifically address one of the most complex enigmas of mankind. In this picture, life-science missions have been in the `NASA` agenda since its foundation, being the search for life beyond Earth one of the most ambitious targets [1].

The scientific community agrees in defining chemistry, energy and water as the three fundamental ingredients for life as we know it [2]. Indeed, life requires some essential chemical elements to develop, such as carbon, hydrogen, nitrogen,

oxygen, phosphorus and sulfur. However, chemical elements are not sufficient by themselves, if they don't interact each other by chemical reactions. Hence, the second fundamental ingredient is energy, which may arise from the light coming from stars, or from radiations from neighbor planets, or from geothermal processes. Finally, there is water. Being a polar molecule, water can interact with a large variety of molecules, dissolving and transporting chemicals elements and facilita ting the reactions. For instance, liquid water on Earth provides to the living organisms the medium to transfer nutrients from outside and to reject the waste products, being one of the main actors in sustaining the life processes.

An emerging area of interest for NASA and for the scientific community is represented by the "Icy" or "Ocean Worlds", which are Solar System bodies that definitely, provisionally, or potentially host globe-girdling layers of liquid water within their interiors, under a thick layer of ice [3]. In particular, a high priority have recently been placed on the science exploration of Jupiter's Europa and Saturn's Enceladus, which are supposed to host the combination of water, chemistry and energy essential for life, and several mission concepts are under study, including the exploration of the internal oceans.

Closer to Earth and very similar to it by size, mass, and composition, Venus is characterized by extreme environmental conditions [4], which make the planet unlikely to harbor life. However, in the past Venus may have been more similar to Earth than now, with milder environmental conditions and probably hosting water oceans, until a severe greenhouse effect made the water evaporating and warmed up the planet. This makes Venus an interesting target for space exploration. Moreover, the recent detection of phosphine in its atmosphere [5, 6] has turn the spotlight on Venus, as this molecule could be related to some biological processes. Atmospheric and landing probes [7] would supply the technological means to scientists to study Venus atmosphere and evolution, providing a direct detection of biosignatures, and also a better understanding of Venus evolution, that will help in predict possible future scenarios of Earth.

In-situ missions to Venus and to the Ocean Worlds pose unique technological and engineering challenges, also because of the extreme environmental conditions. Indeed, the exploration of the internal liquid oceans of Europa and Enceladus requires thermal systems providing the energy to to melt trough the ice crust and keep the electronics within their operational temperature, structures able to withstand extreme external hydrostatic pressure expected at the ocean level, up to 500 bar, and complex communication systems, together with autonomous guidance. On the other side, Venus landers would be subjected to extreme environmental conditions as well, being the atmospheric pressure and temperature at the surface level approximately 92 bar and 462°C respectively, making particularly challenging

the design of cost and mass efficient structural systems and thermal control systems.

Hence, trade off studies are currently being performed to evaluate different technical solutions and mission concepts. As shown in Fig.1.1, space missions are built on a strong network of science, technology, programmatics and architecture, in which the elements are linked together by two-way arrows. Indeed, for instance, advances in technology may open new possibilities for unprecedented missions architectures, or, by converse, specific science investigations may require challenging mission architectures, pulling the development of new technologies.
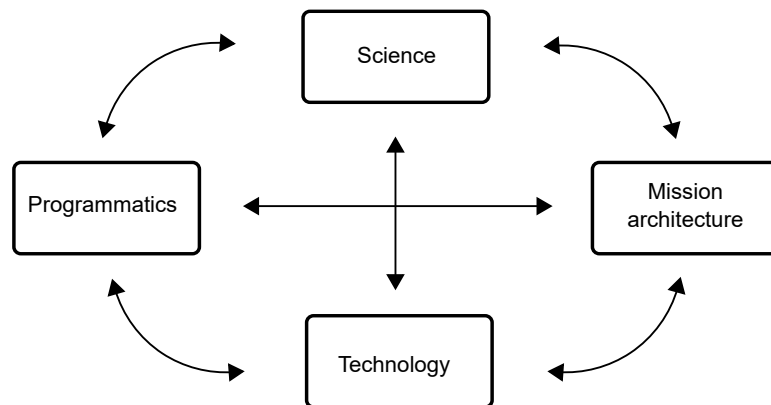
Figure 1.1: The design of a space mission is a complex problem of system engineering, adapted from [8]

Focusing on a system level (Fig.1.2), the design process starts with the definition of the requirements and evolves through iterative concepts and architectural studies, until reaching the final design of the system, continuously and strongly interacting with the technology and its maturation level. The designers are helped by the Technology Readiness Level (`TRL`), that keeps track of the evolution of a technology, from the early research stage, to its development and its final implementation. As shown in Fig.1.3, high `TRL` indexes identify all those technologies mature and ready to be used as a flight hardware, while low `TRL` technologies have still not qualified and technology development plans need to be provided .

In the context of the exploration of extreme environments, new technologies are sough to allow long-lived missions, such as electronics able to operate at very high or very low temperatures, together with lightweight structural solutions able to protect the payload against the external pressure and highly efficient thermal control systems. In the present work, attention will focus on the mechanical design of structural shells for concepts of planetary probes, considering the opportunities given by Additive Manufacturing technologies.
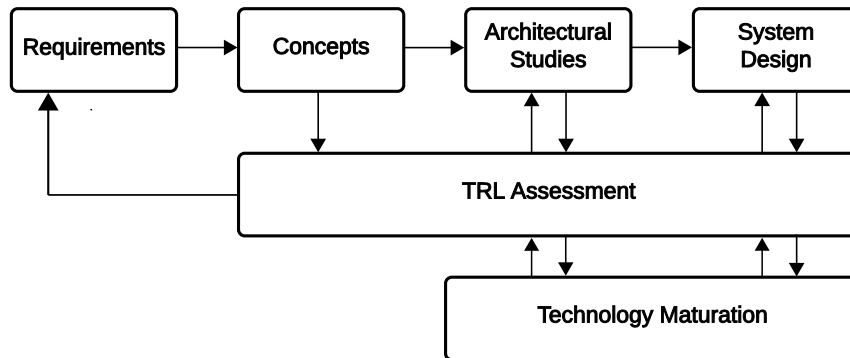
Figure 1.2: Technology and technology maturation are key elements in the system design - adapted from [9]
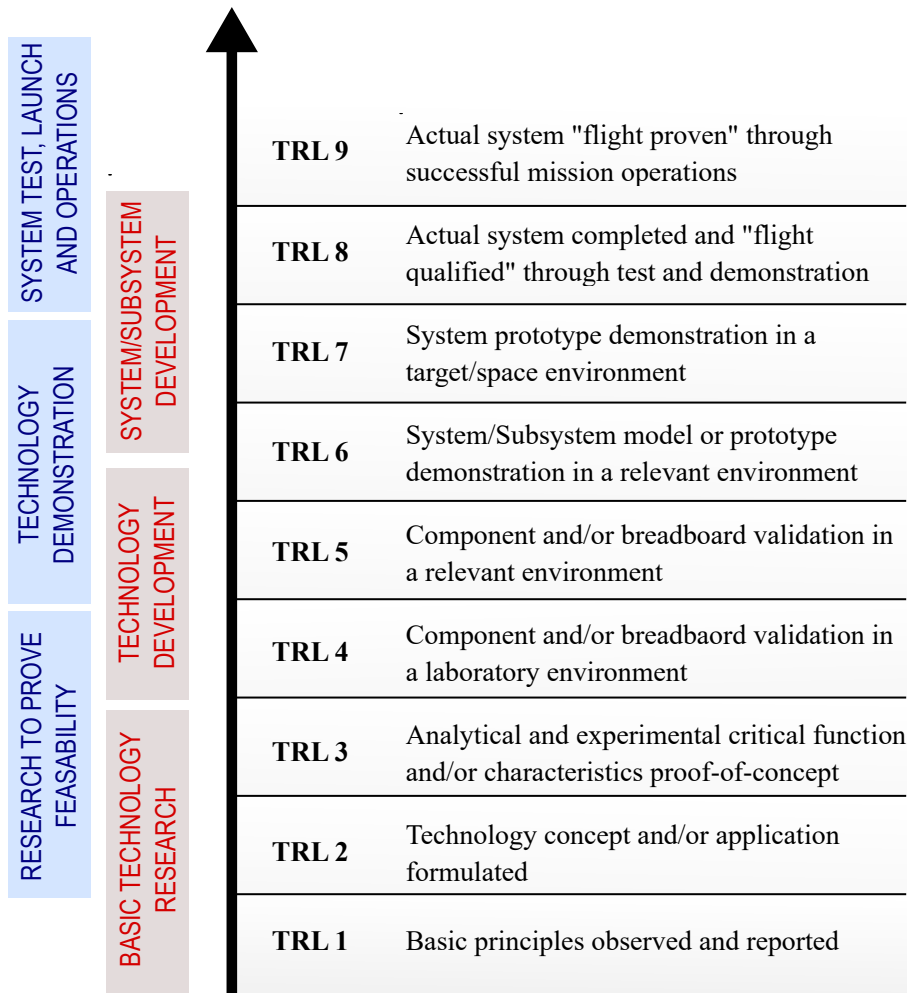
Figure 1.3: Technology Readiness Levels - adapted from [9]

1.2   The new technologies: Additive Manufacturing

The term Additive Manufacturing (`AM`) identifies a category of processes which involves the shaping of solid objects by gradual addition of material, as opposed to conventional machining operations in which material is removed from a bulk. `AM` technologies were firstly developed as rapid prototyping tools for designers, to fabricate showpieces and demonstrators, being mainly limited to polymeric materials [10]. Starting from the 2000s, `AM` has known an exponential growth, with the development of new technologies and the possibility of processing a large variety of materials, from metals to ceramics, as shown in Fig.1.4.
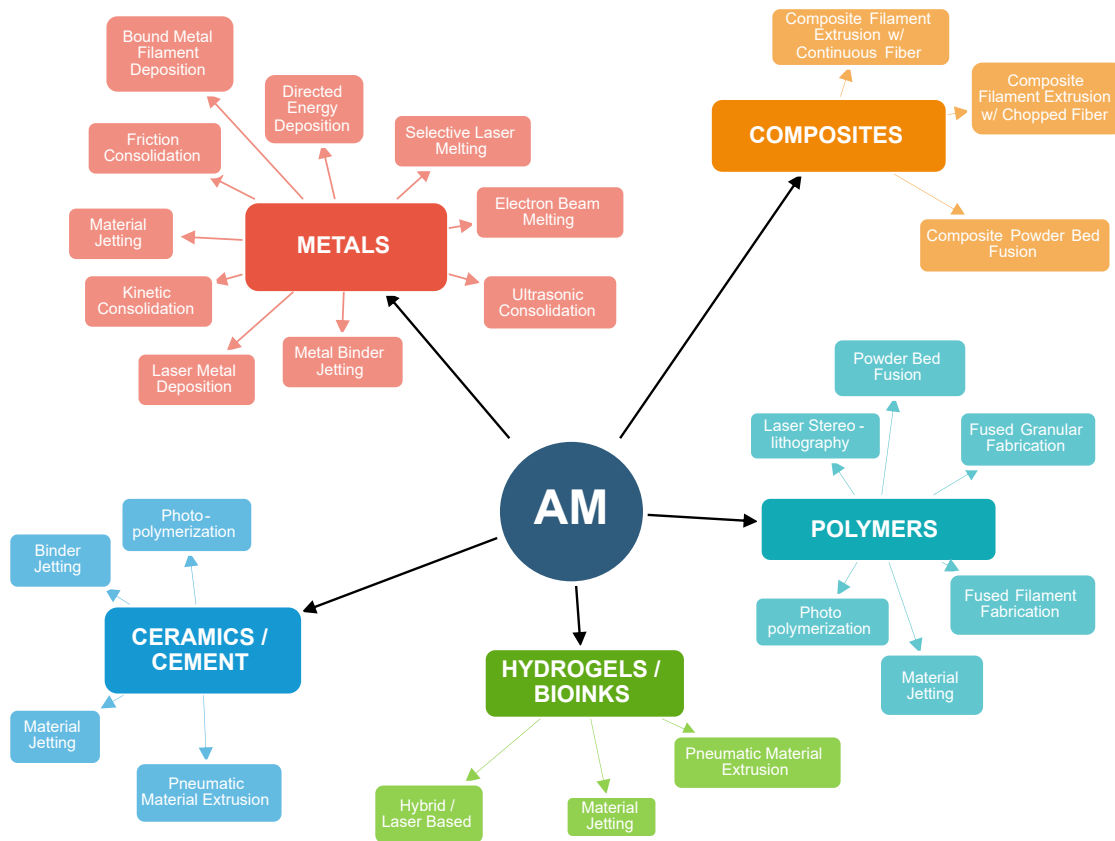
Figure 1.4: Additive Manufacturing technologies

In the case of metallic materials, one of the most common manufacturing methods is Laser Powder Bed Fusion (`L-PBF`) [11], commercially also referred to as Selective Laser Melting, or Direct Metal Laser Sintering. In `L-PBF`, as shown in Fig. 1.5, the material, in the powder form, is deposited in thin (from 20 to 100 μm)

layers by using a roller or a blade, and subsequently consolidated by melting with a laser beam, according to the relevant cross section of the part. The process is then repeated, building each layer onto the previous, creating the three-dimensional object. The loose, unmelted powder remains in position and it is finally removed during post processing.
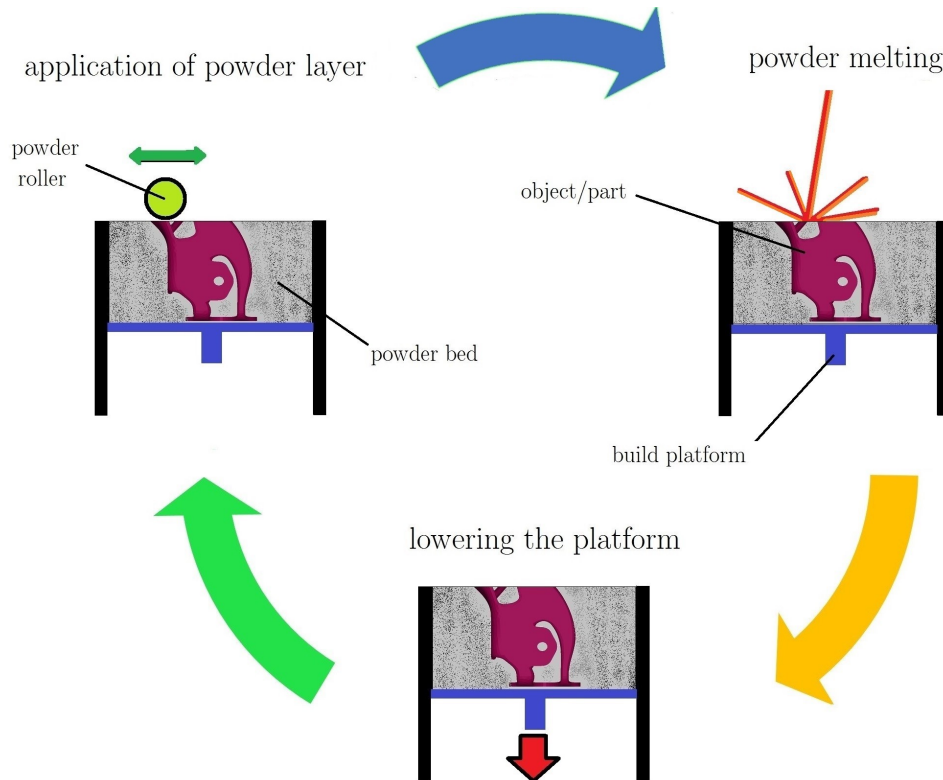
Figure 1.5: Scheme of a typical powder bed process

Beside the working principle by itself, the whole manufacturing process is composed by a total of three different phases [12], as shown in Fig.1.6. The process starts with the Digital phase, in which the three dimensional CAD model is created and processed, to obtain cross sectional slices to be converted in a job file for the AM machine. Secondly, the Manufacturing phase includes all the manufacturing processes properly called, as managing and supplying the raw powder, the set-up of the process parameters (such as laser power, scan speed, scan strategy, layer thickness, etc.), and the fabrication process, with on-line monitoring. Finally, in the Post-processing phase the component is taken off the building plate, loose powder and support structures are removed and eventual heat treatments or mechanical post-processing are performed, such as shot-peening or machining of the interfaces. The last step typically includes non destructive inspection for quality control, in

order to assess manufacturing imperfections.
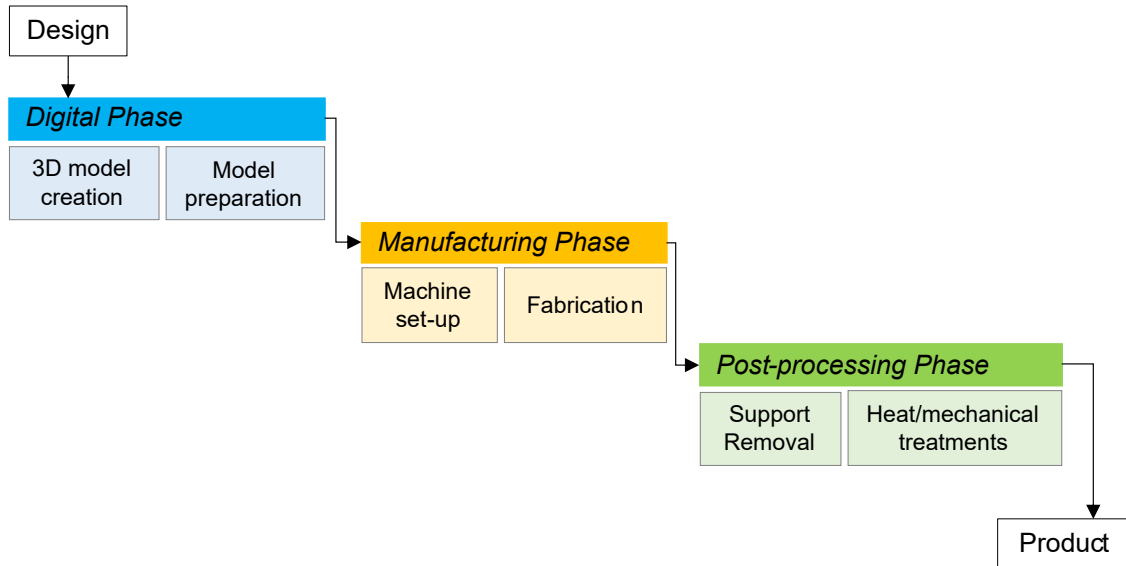
Figure 1.6: Typical phases of `AM` manufacturing cycle, adapted from [12]

A large variety of metallic materials are currently available for `AM`, ranging from steel to aluminum, titanium or nickel-based alloys, or precious materials [13, 14]. The most common `AM` alloys for aerospace applications are aluminum - silicon alloys, such as AlSi10Mg or AlSi7Mg, and titanium alloys, such as Ti6Al4V, due to the high mechanical properties together with the low mass density, which make these materials particularly suited for structural applications. From a thermal point of view, instead, aluminum and titanium alloys behaves very differently, being the former a good thermal conductor, and the latter a poor thermal conductor. A great effort is currently being made by academia and industry, to assess the mechanical and thermal properties of `AM` materials and to tune the manufacturing process and procedures to improve the material characteristics [15]. Generally speaking, `L-PBF` AlSi10Mg and Ti6Al4V alloys have been proved to show static mechanical properties similar to the conventional manufactured equivalents [16, 17, 18]; however, the fatigue behavior is still object of study, being deeply affected by the presence of superficial and internal defects [18, 19].

Although a very large range of applications, from automotive to art, can benefit of `AM` technologies, one of the most suited fields of application is aerospace, requiring high performance components, and being typically characterized by small to medium production lots [20]. Seven applications of `AM` in aerospace have been identified by [21], being:

- new design frontiers, difficult or even impossible to approach with traditional manufacturing techniques, such as multi-materials, gradient alloys and multi functional structures,

- monolithic assemblies, reducing the assembling operations, together with costs and schedule, but also reducing the possible failure points, such as weld and connections,

- high complexity parts, such as truss and lattice structures, with increased performances,

- mass reduction, obtained by taking advantage of the increased design freedom of `AM`, together with new design tools, such as topology optimization and generative design,

- tools for material research, typically not well suited for traditional manufacturing techniques, as they require small amounts of material and small production lots,

- in-space fabrication, for instance, to produce tools for the astronauts on the space station, or to fabricate very large structures on orbits,

- in-situ fabrication with local resources, for instance during lunar or Mars exploration.

In the case of probes for extreme environments, `AM` could provide great benefits, allowing the fabrication of complex internal ribbing and integrated thermostructural systems, as it will be discussed in the present work, potentially resulting in increased performance and reduced mass.

As industries have increasingly started using `AM` technologies, even for critical applications, the demand for qualification standards and procedures is growing [22, 12], with quality needed to be tracked in every phase of manufacturing (Fig.1.6), from the `CAD` model to the final physical part, identifying potential risk factors and the main process variables that can affect the performance of the final product. For example, not optimized process parameters can result in internal defects, detrimental for the performance of the final component; moreover, small features, together with unsupported overhangs can result in imperfect geometries and disconnected parts. Hence, the characterization of the typical manufacturing defects is crucial not only for technologist, during the development of the technology and in tuning the process parameters, but also for designers, in understanding the process limitations and designing components and systems, that can best exploit `AM` capabilities.

In this frame, `AM` technologies prove to be groundbreaking processes that require novel approaches not only in manufacturing, but also in the design methodologies.

1.3 The new design approaches

As described in the previous section, the new manufacturing technologies offer a broad range of new opportunities. Starting from the design of a component conventionally manufactured, `AM` can be applied at three different re-design levels. First, it can be directly applied on the original geometry, without any re-design activities, potentially resulting in schedule savings, if compared to traditional manufacturing techniques, but without providing any improvements in the performance of the product. At a deeper level, `AM` can be applied at a component level, performing a re-design of the part according to the component requirements and to the manufacturing limitations. The increased design freedom, allowed by the possibility to modify the geometry of the part, might result in improved performances and mass savings, together with the schedule saving related to the switch to `AM`. However, to fully exploit this potential, design procedures must be re-evaluated, starting at the system level, from the analysis of the system requirements.

In the case of probes for the exploration of extreme environments, the design of primary structures is particularly challenging, because of the coexistence of structural loads, thermal loads, and corrosion. Hence, an exhaustive definition of the system requirements can be a very complex task. For instance, typical primary structures for Venus surface probes shall:

- [*Req.*1] provide an internal volume to accommodate the scientific instruments, the electronics, and the hardware of the other subsystems,

- [*Req.*2] provide interfaces and ports for the scientific instruments,

- [*Req.*3] be accommodated in a entry module, inside the fairing of a launch system,

- [*Req.*4] withstand the flight, on-orbit, an entry-descent-landing loads,

- [*Req.*5] protect the payload from the external pressure loading, avoiding catastrophic failures or leakages from the outside, for the duration of the mission,

- [*Req.*6] together with the thermal control system, protect the payload form the extreme temperatures of the environment,

- [*Req.*7] provide corrosion resistance for the entire duration of the mission,

- [*Req.*8] fit in the mass budget of the entire lander,

- etc.

From this (incomplete) list, it is clear that the design of a primary structure can not be considered as a purely structural problem, but multi-physics and multi-disciplinary approaches are required, starting from the material selection.
In fact, the first step of the design process is performing trade-off studies to compare different materials, based on their properties. For instance, in the case of a

Venus lander reported above, materials shall be compared based on Req. 4 and 5, preferring alloys with high Young's modulus and strength, but also based on Req. 6, preferring materials with low thermal conductivity, and Req. 8, preferring lightweight alloys. Ashby plots, as the one reported in Fig. 1.7 can help in this task, graphically comparing different options by considering several properties simultaneously in the same figure.

Figure 1.7: Examples of Ashby plot for material trade-off activities - alloys currently available for `AM`

Obviously, manufacturing limitations must be taken into account as well, as, for instance, the number of alloys currently available for `AM` is still quite limited. It must be noted that trade-off and architectural studies may also be responsible of assessing the maturity of the technologies, such as the manufacturability of specific

alloys, limiting the design space, or eventually providing developments plans to boost the TRL progress.

The second design variable is the geometry. The development of AM has brought an increased design freedom, allowing the fabrication of very complex structures, expensive or even impossible to fabricate by conventional manufacturing. Several design techniques have been developed to exploit the potential of AM capabilities, such as topology optimization, generative and parametric design tools. In the case of primary structures for probes of harsh environments, the choice of options is limited to few configurations, being mainly cylindrical and spherical shell structures. By recurring to AM processes, it is possible to obtain complex stiffening systems, such as periodic internal ribbing, potentially resulting in improved performance, as well as cost and schedule savings. It must be noted that the structural design and optimization of lightweight shells with internal stiffening systems can be a tricky task, especially in the case of probes for the exploration of Venus surface or Europa's ocean, where the extreme environmental conditions may cause buckling and structural instability, which can be difficult to predict. Moreover, in the early design stage, simplified approaches may be required, to provide tools for quick comparisons between different options during trade-off studies. In the present work, analytical formulations and FEA-based tools will be used to investigate the performance of shells undergoing external pressure loading and to propose optimized stiffening layouts.

Finally, multi-functionality must be taken into account as well. Hence, in the case of space probes for extreme environments, integrated thermo-structural systems may provide superior performances together with potential mass savings, but also cost and schedule savings, due to the reduced assembling operations. In this regard, AM is one of the key technologies, as it enables the fabrication of optimized thermal devices [23], characterized by complex geometries, such as internal cooling channels, or conformal heat sinks, or multi-scale architected materials, such as pin fin surfaces, or heat pipes.

Heat pipes are one of the most used thermal control devices used in space applications. Firstly patented in 1942 [24], heat pipes are heat transfer devices based on two phase working fluids, consisting of a sealed tube, usually made of aluminum or copper-based alloys, containing a wick, typically made of grooves or porous material, partially filled by a working fluid. As no air is contained within the tube, the liquid fluid is in the saturated condition. At the hot end of the heat pipe (please refer to Fig.1.8), the liquid fluid evaporates, absorbing heat. The vapor fills the vapor cavity and, once reached the cold end of the heat pipe, it condenses, releasing heat. The liquid fluid is absorbed by the wick and it is pumped to the vapor end by the capillarity force.
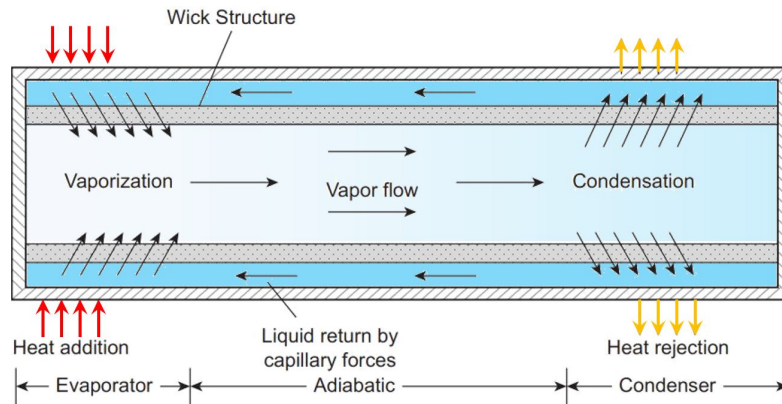
Figure 1.8: Heat pipe working principle, adapted from [25]

Thanks to the liquid-vapor and vapor-liquid state transformation, heat pipes are particularly efficient in transferring heat, with an effective thermal conductivity along the axis direction up to four orders of magnitude greater than the thermal conductivity of copper [26], as shown in Fig.1.9, in which different heat transfer technologies are compared by considering the system mass and the capacity to transfer a heat load for a unitary distance. Moreover, heat pipes can result in significant mass savings when replacing solid conductors [27], and they generally provide high reliability and low costs due to the simple functioning system, that does not involve moving parts [26]. A number of different systems and technologies have been developed, ranging from constant conductance heat pipes, to variable conductance heat pipes, loop heat pipes, pulsating heat pipes etc. [28, 27].

Heat pipes are conventionally manufactured by sinterization or extrusion techniques and then integrated in the final component, for instance by brazing. This typically limits the design to simple, tubular geometries and involves long and expensive assembling operations. In recent years, several researchers invetigated the possibility to obtain porous materials for heat pipe wicks by AM. A manufacturing demonstrator of an AM heat pipe was published in 2013, proving the possibility to fabricate porous wick using micro lattice structures [30]. This was also recently confirmed by other studies [31, 32]. A second strategy consists in recurring to stochastic foams. In fact, one of the most revolutionizing opportunities offered by AM is related to the possibility of tuning the material properties by varying the process parameters, obtaining full-solid, or porous materials within the same fabrication job. In this frame, NASA Jet Propulsion Laboratory is developing AM of porous materials, in order to fabricate porous wicks for heat pipes directly integrated within structural systems. AM wicks for evaporators of two-phase fluid loops have already been successfully designed, fabricated and laboratory tested, showing promising results
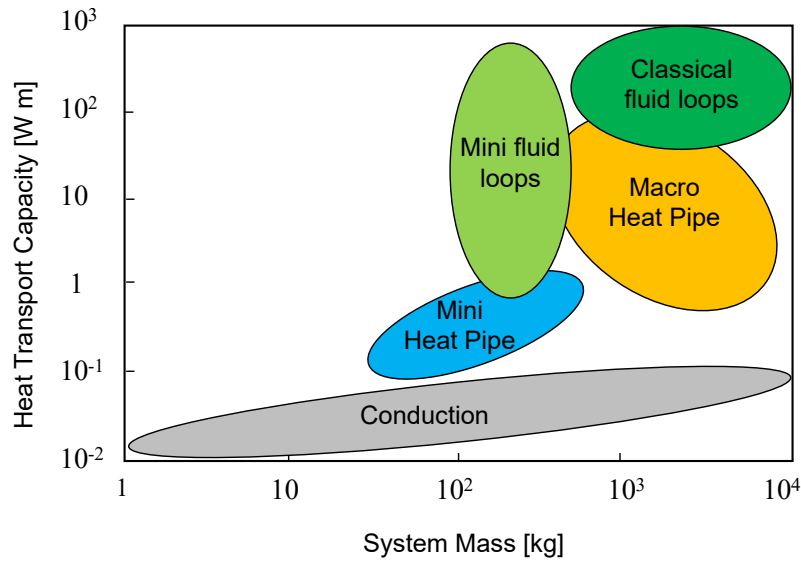
Figure 1.9: Heat transfer technologies compared by system mass and heat transfer capacity, adapted from [29]

[33, 34, 35]. Moreover, a concept demonstrator of a battery case with conformal heat pipes for thermal control has been successfully built and tested, showing a thermal conductance of one order of magnitude higher than solid aluminum [36]. `AM` technologies applied to heat pipes might allow a significantly increased design freedom, enabling the fabrication of complex geometries and conformal channels, together with multi-functional systems, resulting in improved performances and reduced assembling operations. Moreover, the short production cycle of `AM` shrinks the scheduling time, allowing quick design iterations, especially during the early design stage.

1.4 The aim of this study

The research presented in this dissertation is focused on the design of primary structures for probes for the harsh environments exploration, investigating the potential benefits related to the adoption of Additive Manufacturing as fabrication technique, and assessing novel design methodologies aimed at exploiting the `AM` capabilities. The object of the study has been provided in a collaboration framework between the Department of Mechanical and Aerospace Engineering (`DIMEAS`) of Polytechnic of Torino (Italy), and the `NASA` Jet Propulsion Laboratory / California Institute of Technology, under the `JPL` Visiting Student Research Program.

The present work has the objective to propose an Additive Manufactured lightweight layout for the primary structure of a concept of a Venus lander, in which a

periodic pattern of stiffening ribs is used to improve the mechanical performance of the system. Moreover, a prototype for laboratory testing of a thermal control device, to be eventually embedded within the primary structure, has been structurally optimized, by recurring to lattice structure infill.

The complexity of the geometry of the primary structure under study, together with the extreme loading conditions and the uncertainties of the novel manufacturing processes, requires a modeling that starts with simple analytical and numerical tools, evolves through an optimization phase, and it involves experimental testing, aimed at the validation of the models. In this context, a novel analytical optimization method for isogrid-stiffened spherical shells has been developed and validated through an experimental campaign (presented in [37, 38]).

A preliminary design activity on the evaporator to be eventually embedded within the structural shell, has been performed, working on a proof case for laboratory testing [39]. A design methodology for optimizing the structure, based on structural and thermal requirements has been proposed, including experimental activities at specimen level, aimed to assess manufacturing limitations in fabricating small struts (presented in [40]). Unfortunately, the research activities have been affected by Covid-19 events, and the planned experimental testing on the evaporator level has been delayed.

The brief introduction presented in this chapter highlighted how the new technologies require to formulate the design processes in a top-down approach, starting from the system level. A practical application will be given in the following chapter, in which an early study conducted on a concept of a meltprobe for the exploration of Europa's internal ocean will be presented. This design study, aimed at providing a first sizing of the conceptual probe, together with assessing design methods, consisted in a first trade-off analysis of different materials and configurations, including lightweight and thermo-structural shells, with heat pipes co-fabricated within the primary structure. This activity provided a preliminary testing ground for investigating typical requirements and issues related to the design of primary structures for harsh environments, to be fabricated by `AM`.

Chapter 3 will introduce the object of the study, being a concept of a Venus surface lander proposed by `NASA JPL`. The harsh environmental conditions of the surface of the planet pose unique challenges for both the structural and the thermal control systems, which need to withstand very high external pressures, up to 93 bar, and extreme temperatures, up to 462°C. An overview of past missions to Venus will be presented, together with concept studies proposed for future missions. Attention will focus on short- and mid-duration landers, with a typical lifetime in the range

going from few hours to one day, investigating the main functional requirements of the primary structure. The conceptual configuration of an Additively Manufactured, integrated thermo-structural shell under study at `NASA` Jet Propulsion Laboratory will be presented. This conceptual design consists in a Ti6Al4V spherical shell, reinforced by a stiffening system, and integrating a porous wick, that works as the evaporative device of a two-phase thermal control system, mitigating the effects of the extreme temperature of Venus, for the duration of the mission. `AM` is the enabling technology, as it allows both the fabrication of complex internal stiffening systems, and the co-fabrication of porous and full-solid materials within the same product.

Chapter 4 will present the main issues related to the design of spherical shells undergoing external pressure loading, involving not only yielding failure mode, but also structural instability. Analytical and numerical approaches for the early design stage will be described, for both shells without internal ribbing (or "plain shells"), and shells reinforced by periodically spaced ribs, forming a triangular pattern (or "isogrid shells"). This layout, although quite common for plates and cylindrical shells, has been rarely investigated for a spherical shape, mainly because of the limitations of conventional manufacturing techniques, but it can be relatively easily obtained by recurring to `AM`. A methodology for the design and the optimization of isogrid spherical shells will be proposed, based on analytical formulations.

In Chapter 5, the design methods previously described will be applied to the study case of the Venus lander, providing a preliminary comparison between plain and isogrid configurations and highlighting the need of experimental activities aimed at investigating the behavior of plain and isogrid shells fabricated by `AM` and validate the design methods.

Chapter 6 will report the experimental campaign, consisting in the design, manufacturing, and testing of sub-scale components. Hydrostatic test on both plain and isogrid shells, increasing the pressure up to the implosion of the test articles, have been performed for model correlation. A relative environment test, aimed at assessing the behavior of the component the pressure and temperature of Venus will be presented as well. The final design synthesis will be presented, summarizing the lessons learned. To close the loop, the integrated thermal control system has to be considered as well. A manufacturing demonstrator of an evaporator porous wick co-fabricated within an isogrid-reinforced spherical shell proved the manufacturability of such a system, as a monolithic component, by recurring to `AM`.

For a better understanding of the `AM` evaporator, Chapter 7 will give an overview on two-phase thermal control systems, focusing on a Two Phase Mechanical Pumped Fluid Loop system, a promising technology currently under development at `NASA`

JPL. Particular attention will be given to a prototype of the `AM` evaporator for laboratory testing, in order to propose a novel optimized structure.

As a first step of the optimization process, Chapter 8 will describe some experimental activities aimed at assessing `AM` limitations, especially when fabricating small struts, that could be used as a lattice infill to optimize the evaporator. Chapter 9 will finally present some design activities aimed at investigating the mechanical behavior of the evaporator, with the final goal of proposing a novel optimized layout. Unfortunately, Covid-19 restrictions limited and delayed the planned activities, which would include experimental activities on specimens for better material characterization, and finally the fabrication and testing of the evaporator. Finally, conclusions and suggestions for future work will be presented.

Chapter 2

A preliminary case study: a concept of a meltprobe for Europa

In the frame of the collaboration with `JPL` within the PhD activities, a first design study of a concept of a probe for Europa has been performed, aimed at exploring typical issues related to the exploration of harsh environments and investigating the potential benefits of Additive Manufacturing.

The so-called "Ocean Worlds", such as the Jupiter's moon Europa, have been identified by the scientific community as a potential location for life in the Solar System. In-situ missions are currently under study, involving probes capable of descending through the thick ice crust, accessing the internal oceans and seeking for evidences of life.

In this work, design concepts of the structural shell of a cylindrical probe for Europa's exploration have been studied. The mechanical design of such a probe is particularly interesting, as the system undergoes some harsh environmental conditions in operation, with extreme external pressures and temperatures, and a corrosive environment. A trade-off study has been performed, considering how different materials and layouts affect the structural and the thermal performance. Analytical and numerical models have been used to compare different layouts, during the optimization process. Finally, a configuration based on lightweight multi-functional shells has been designed, integrating heat pipes within the structural shell. The design synthesis exploits the Additive Manufacturing technologies, as complex geometries and solid and porous materials can be manufactured with Laser Powder Bed Fusion within the same process. This study has been proposed for an assessment of technologies, materials and design procedures, as the preliminary phase of a mission concept to Ocean Worlds.

2.1   Ocean Worlds Exploration

Although the inner composition of Europa and Enceladus is still uncertain, evidences of a liquid ocean beneath an icy crust have been provided by the data obtained thanks to the missions Voyager 1 and 2, Galileo and Cassini. More specifically, during several flybys, Galileo's magnetometer detected anomalies in Europa's magnetic field, consistent with the hypothesis of a salty water ocean [41]. Enceladus' Ocean, on the other hand, was firstly inferred from the anomalous gravitational field estimated using Doppler tracking, and then confirmed by sampling Enceladus' plume in the south polar region [42].
New orbiter missions to Europa (NASA Europa Clipper and ESA JUICE) are currently in progress and will provide crucial information about the internal composition of Europa, the ice crust thickness and safe landing sites for potential future missions; analogous missions to Enceladus (for example, ELF and LIFE) have been already proposed [3]. In-situ missions to the surface of Europa and Enceladus are being studied, producing several concepts for landers [43, 44, 45], rovers [46] and devices for sample acquisition and handling [47, 48].

Final goal is searching for evidences of life by penetrating the ice crust and directly accessing the oceans, as depicted in Fig.2.1; to this challenging end, several mission concepts, commonly referred as "melt probes" or "Cryobots" [49, 50, 51, 52], have been proposed and are currently under study.

2.2   Europa's environmental conditions

The Europa's internal structure and environmental conditions are still object of debate. A 100 km thick water Ocean is thought to lay under the ice crust, above a rocky mantle and an iron core. Estimates of the ice crust thickness are really variable, ranging from 10 km to 30 km [53, 54]. On the surface, low temperatures (approximately from -220°C to -160°C) and low pressure are expected [55]. Due to its proximity to Jupiter, its surface is exposed to large amounts of radiation.

Predictions of salt content within the shell range up to 25%. it decreases down to 2% by the ocean itself, similar to brackish water found on Earth. What makes Europa's environment so challenging, however, is the volcanism of Io, another moon of Jupiter, depositing sulfur on the surface of Europa. This sulfur reacts with the radiation environment and ice on the surface to become sulfuric acid. Depending on how long this process has been going on relative to Europa's dynamic tectonic ice cycles, the acid may be localized near the surface, or well mixed throughout the ice shell [56].
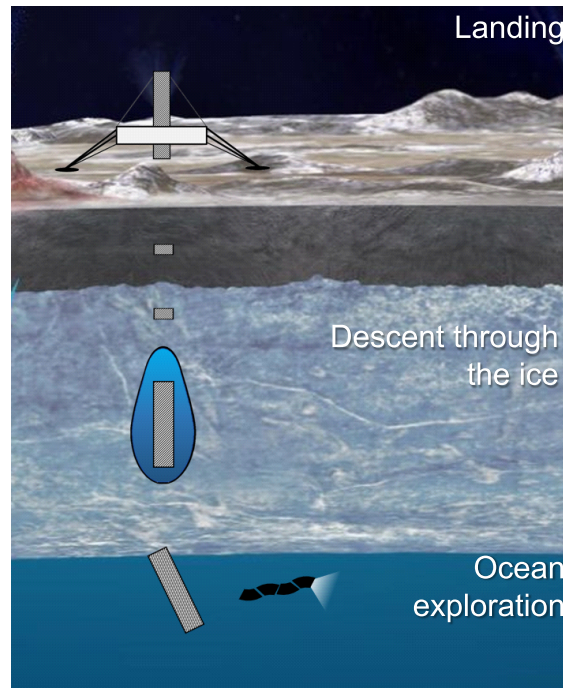
Figure 2.1: Overview of the mission concept, from landing on Europa's surface, to the descent trough the ice crust and finally to the exploration of the internal ocean

2.3   Overview of the mission concept

Concepts of a Cryobot/Meltprobe mission to Europa have been studied by JPL [52, 57], being organized in the following phases, as reported in Fig.2.2:

1. launch,

2. cruise,

3. landing,

4. surface operations,

5. ice descent,

6. transition of the ice/ocean interface,

7. deployment of an Ocean explorer,

8. decommissioning and end of mission.

Such a pioneering mission, together with the harsh environmental conditions, poses unique challenges, in every phase and for every subsystem, ranging for example from the management of the thermal energy, to the development of the technology for ice drilling and melting, to the data transmission through a thick layer of ice [52, 57].
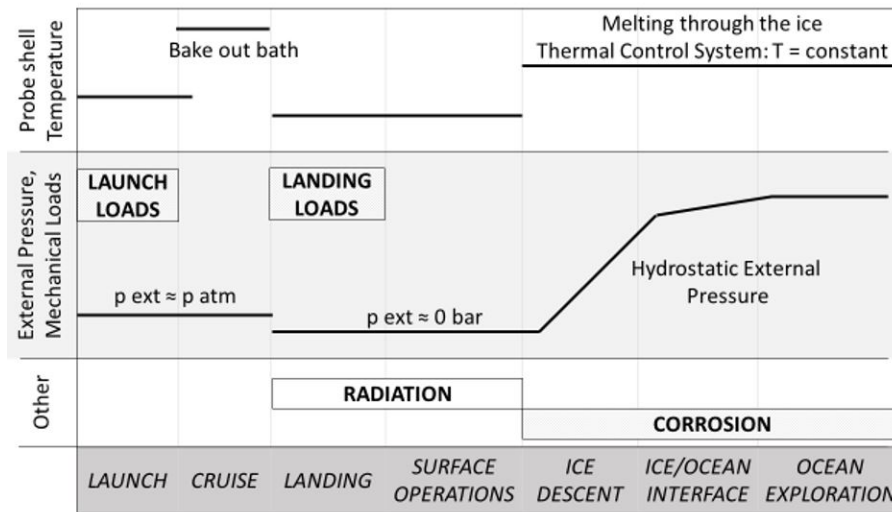
Figure 2.2: Main missions phases, together with the relative loading conditions of the primary structure

The subsystems tree is presented in Fig.2.3, together with a concept of a configuration of the probe, reported in Fig.2.4. According to this concept, the probe is basically a cylinder containing:

- a head for melting, mechanical cutting and water jetting for ice penetration,

- an undersea science explorer, to be freed once reaching the ocean of Europa,

- Radioisotope Thermoelectric Generators (RTGs), to provide electric and thermal power,

- a thermal system, to keep the electronics within their operational temperature and to manage the thermal power in melting through the ice crust of Europa

- electronics and science instruments,

- avionics,

- a deployable communication system, to transmit the data back to Earth.

According to this concept [52, 57], the ice descent is performed mainly by melting the ice; however, cutting and water jetting systems are present as well, being used in the first steps and in case of salty clusters. The thermal energy is provided by RTGs and transported by means of heat pipes, located as close as possible to the external surface of the probe shell. A modular design, such as the one showed in Fig.2.4, could help not only in the manufacturing stage, but also during the preliminary design activities.
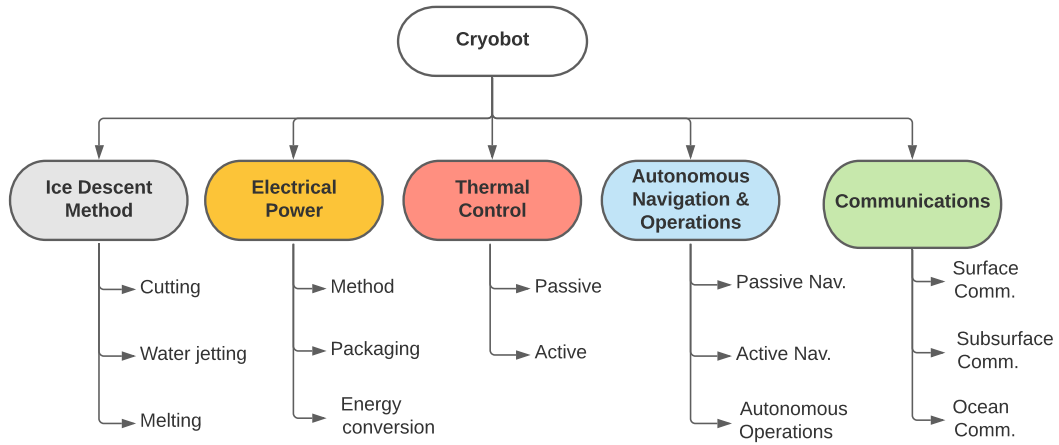
Figure 2.3: Key systems of a concept of a Meltprobe/Cryobot mission - adapted from [52]
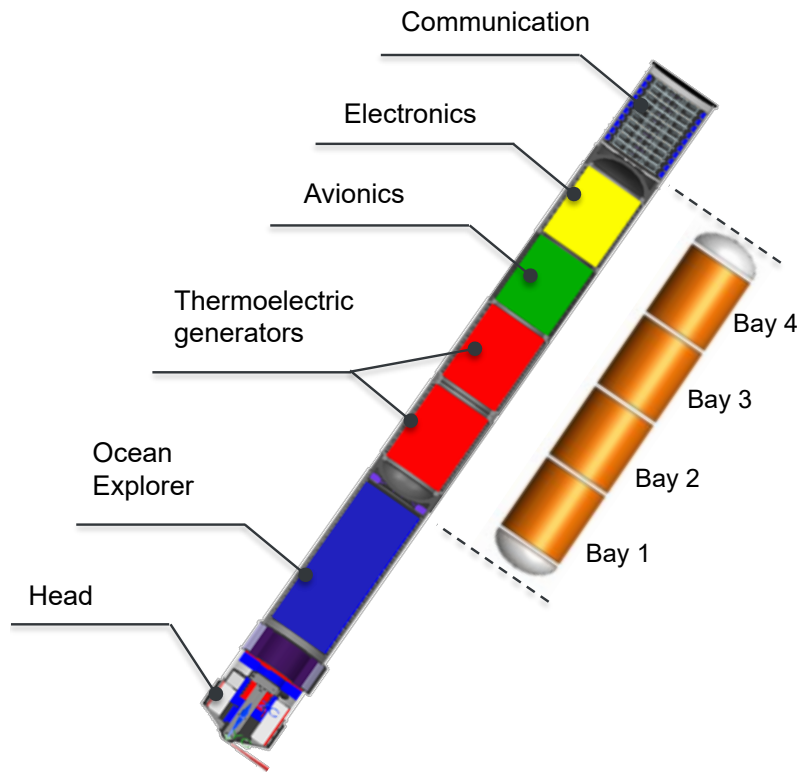
Figure 2.4: Overview of the main components of the concept

The primary structure is subjected to multiple loading conditions, corresponding to the different phases of the mission. In the case of Europa, the external pressure

21

at the ice/ocean interface (conservatively, p=50 MPa) is considered as the most severe mechanical load for the pressurized segments. It must be noticed that only some of the components (RTGs, avionics and electronics) shall be contained in a pressure vessel able to withstand the high pressure of the ocean; the bays for the Head, the Ocean explorer and the communication pucks, by the contrast, do not need a pressure vessel, as they shall be designed to be directly exposed to the ocean. The cold temperatures of the icy moons (-220°C to -160°C on the surface, 0°C at the ice/ocean interface [58] are not too much of a concern for the probe itself, as its walls is kept warm from internal heating, due to the RTGs. Temperatures may pose a design challenge, though, for other parts of the spacecraft which is frozen into the ice such as the communication pucks, surface communications relay, and any tethers. It must be noted that the pressure vessel is also subjected to high temperature (T $\approx$ 150°C) during the cruise stage, as part of a heated water bath as a form of contamination control. This should help simplify terrestrial bake-out procedures by enabling much of it to be done during cruise.

To summarize, the primary structure of this meltrprobe concept shall:

- [*Req.*1] provide a pressurized internal volume to accommodate the scientific instruments, the electronics, and the hardware of the other subsystems,
- [*Req.*2] provide an unpressurized internal volume to accommodate the ocean explorer,
- [*Req.*3] be accommodated in a entry, descent and landing module, inside the fairing of a launch system,
- [*Req.*4] withstand the flight, on-orbit, an entry-descent-landing loads,
- [*Req.*5] protect the payload from the external pressure loading, avoiding catastrophic failures or leakages from the outside, for the duration of the mission,
- [*Req.*6] withstand eventual impacts during the ice descent,
- [*Req.*7] provide corrosion resistance for the entire duration of the mission,
- [*Req.*8] transfer the heat from the RTGs to outside, in order to melt the ice, eventually integrating heat transfer devices,
- [*Req.*7] fit in the mass budget of the entire probe.

In the frame of the collaboration with JPL, a design study has been performed, exploring design methods and providing a first sizing of concepts for primary structures. The task consisted in:

1. a trade off analysis of different materials,
2. a preliminary investigation of the behavior of plain cylindrical shells subjected to high external pressure, by recurring to analytical methods,

3. the setup of an optimization procedure based on Finite Element Analysis, aimed at designing optimized ring-stiffened shells,

4. proposing novel layouts for `AM` integrated thermo-structural shells, having heat-pipes co-fabricated within the shell

The baseline configuration consists of a cylindrical shell with a internal diameter of approximately 230 mm; bay length, shell thickness and eventually internal ribs are design variables. In this early design stage, the driving structural requirements are derived from *Req.5*, due to the very high pressure expected at the ice/water interface. In particular, two failures modes are connected to external pressure loading, being yielding of material and structural instability; the most critical failure mode could be either the first or the latter, depending not only on the material properties (E, σ_y), but also on the length of vessel and the external pressure. As suggested by `NASA` technical report [59], safety factors of 1.25 and 1.40 shall be used for the static and the buckling analysis respectively.

2.4   Material selection

In order to select a material for the primary structure a number of key material parameters must be considered. From the structural point of view, the most important properties are the Young's modulus, the yield strength and the mass density. A significant part of the melt probe's outer structure is an external pressure vessel needing to withstand approximately 50 MPa at the ice/water interface. This load needs to be supported as efficiently as possible: a high value of the Young's modulus is required, in order to avoid instability and high specific strength is needed to reduce the mass.

The second constraining factor is the thermal conductivity of material. During the descent through the ice crust, a large amount of heat shall be efficiently transferred from the thermal generators to the outer surface of the vessel, to melt the ice around the probe, forming a liquid water jacket. Heat transport and temperature control depends on the technology of the thermal control system, on the geometry of the probe and on the material and the thickness of the skin of the shell. In particular, thermal conductivity is a crucial parameter. If the thermal conductivity of the shell is low, the working fluid of the thermal control system needs to be at a high temperature, increasing the operational temperature of the power unit. A hotter working fluid also may need to operate at a temperature higher than the internal electronics, necessitating investment in secondary methods for cooling. A large thermal conductivity enables more freedom in the placement and number of heat pipes, as the largest thermal resistance moves from the structural shell to the shell/water interface.

Corrosion resistance needs to be considered as well. Europa, in particular, is characterized by high concentrations of salt and sulfuric acid, which may be an issue for many metallic alloys. However, it must also be noted that protective coatings could be used to broaden the range of possible materials.
The minimum service temperature and the downgrading of mechanical properties at low temperatures shall be evaluated as well, even if the probe shall be kept warm by the thermal system for the entire duration of the mission.

Manufacturability shall be taken into account as well. Early designs have shown a crucial need to use Additive Manufacturing for fabrication. Hence, the materials shall be currently or potentially processable by `AM`, i.e. available in powder or wire format and showing high weldability.

After narrowing down the materials choices based on the criteria above, a few trends become apparent and the choice of material collapses to just a few basic materials systems, being Aluminum, Copper, Iron, Nickel, and Titanium.
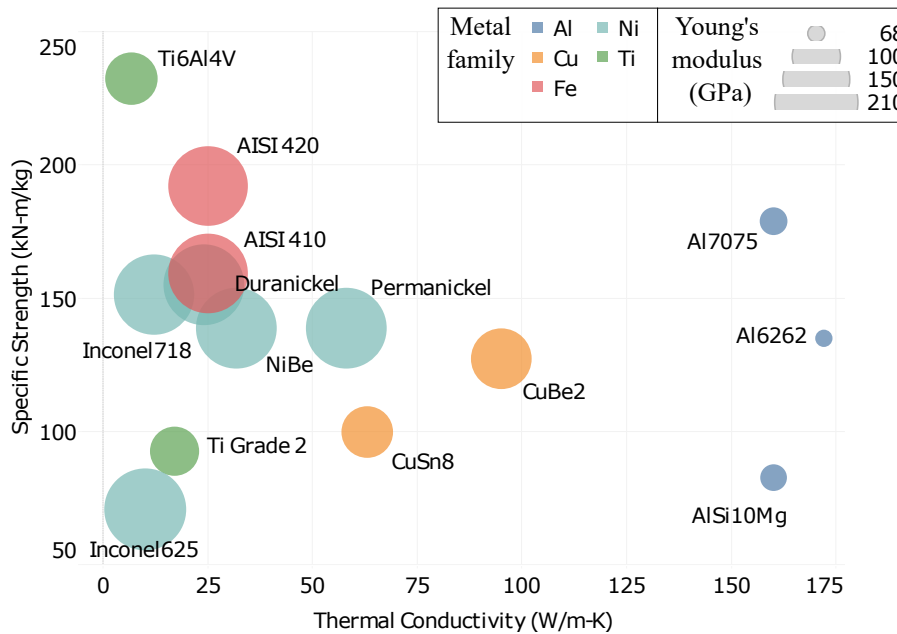
Figure 2.5: Material selection: Ashby plot for comparing different materials by their mechanical and thermal properties

Aluminum alloys typically have very high thermal conductivity and medium to high specific strength, depending on the alloy. The relative low Young's modulus can be an issue when buckling problems need to be addressed. Only AlSi10Mg and few other aluminum alloys are currently available for `AM`, although there is significant investment currently underway by the materials community to develop

printable 6000-series and 7000-series alloys. 6262 is formulated for salt water service, while most aluminum alloys are not recommended for it and they require corrosion resistance coatings.

Commercially pure titanium, grade 2, offers excellent corrosion resistance, but low specific strength and thermal conductivity. It is weldable, although it is not currently being fabricated by `AM`. There may not be a fundamental reason why it has not been fabricated as of yet, though. It is likely just there is significantly higher demand for Ti6Al4V, so the industry has instead focused on its development. Ti6Al4V offers one of the highest specific strength, together with a relative high Young's modulus, which could results in configurations with very thin shells, so that the effects of the low thermal conductivity might be mitigated. Fracture toughness at low temperatures shall be investigated.

Stainless Steel AISI 420, with a high strength heat treatment is the stiffest alloy downselected, which means it will have the greatest resistance to buckling (minimizing the need for stiffening rings). It also has very high specific strength. Its main drawback is a minimum operational temperature of -58 °C. During expected operation of the mission, the walls of the melt probe should not get this cold, but if there is a brief issue with thermal control it could lead to catastrophic failure. Similarly, because this specific alloy is heat treated at 200 °C, it has a lower maximum operating temperature of 169 °C. This could be too close to temperatures seen near the `RTG`s or experienced during cruise.

Copper Beryllium Alloy is a very strong choice. While it has a relatively modest specific strength and elastic modulus, it has a superb thermal conductivity. It is already used for undersea vessels, so it would have heritage in saltwater environments. No issues on the minimum or maximum service temperatures. However, it is not a very promising alloy for `AM` as its weldability ranges from poor to good.

Nickel-beryllium alloys have a high specific strength and stiffness, and good thermal conductivity, but they are still not currently available for `AM`. Among nickel-based alloys, Inconel alloys provide good corrosion resistance and have already been developed for `AM`. As mentioned before, additional high performance alloys can be added to the list, when specific coatings for corrosion resistance are applied.

2.5   Plain shells

Goal of the activity is performing a first assessment of layouts of cylindrical vessels. A preliminary study on plain shells has been conducted using analytical models. The well-known equations of hoop (σ_h), axial (σ_a), and radial (σ_r) stresses of thin-walled cylinders subjected to hydrostatic external pressure and with simply supported boundary conditions are briefly reported below, together with a scheme of the problem in Fig.2.6.

$$\sigma_h = \frac{pR}{t}; \;\; \sigma_a = \frac{pR}{2t}; \;\; \sigma_r \approx 0 \tag{2.1}$$

being p the external pressure, R the radius of the cylinder, and t the thickness. The equations are valid under the hypotheses of thin shell ($t/R < 0.1$), small displacements and do not take into consideration the effects of interfaces and endcaps.
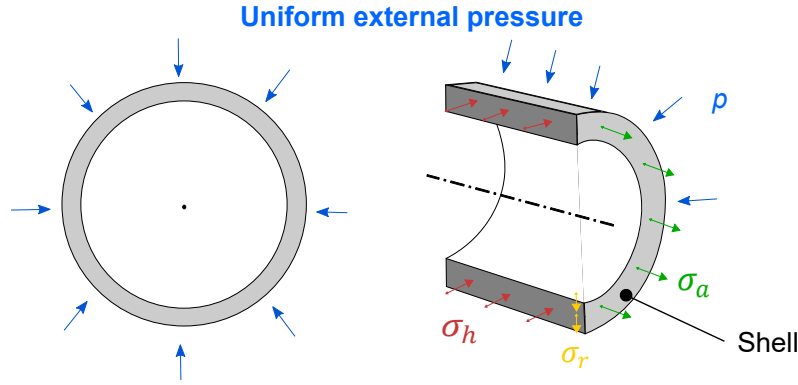
Figure 2.6: Scheme of the problem

Beside yielding, structural instability, or buckling, is a possible failure mode as well. According to the `NASA` technical report [60], the buckling critical pressure (p_{cr}) can be evaluated as follow:

$$\frac{p_{cr}^{\text{SP-8007}} R l^2}{\pi^2 D} = \frac{1}{\beta^2 + 1/2} \left[(1 + \beta^2)^2 + \frac{12 \gamma^2 Z^2}{\pi^4 (1 + \beta^2)^2} \right]$$

$$\text{where: } D = \frac{E t^3}{12(1 - \nu^2)}$$

$$\beta = \frac{nl}{\pi R m} \tag{2.2}$$

$$Z = \frac{l^2}{rt} \sqrt{1 - \nu^2}$$

where D is the wall flexural stiffness, Z is the curvature parameter, γ is the correlation factor (suggested equal to 0.752 [60]) and β is the buckle aspect ratio, function of m and n, number of buckle half waves in the axial direction and in

the circumferential directions. The values of m and n shall be chosen so that the resulting critical pressure is minimum. Conservatively, the `NASA` document suggests to make β varying continuously.

Alternatively, the Von Mises/Kendrick equation [61] is iteratively solved, varying the integer parameter n in order to minimize the pressure, being the Knockdown Factor $\mathtt{KF_1} = \sqrt{\gamma} = 0.75$ and $\lambda = \frac{\pi R}{l}$

$$p_{cr}^{\mathtt{VM}} = \frac{\mathtt{KF_1}E\left(\frac{t}{R}\right)}{n^2 + \frac{\lambda^2}{2} - 1} \left\{ \frac{\left(\frac{t}{R}\right)^2 \left[n^2 + \lambda^2 - 1\right]^2}{12\left(1 - \nu^2\right)} + \frac{\lambda^4}{\left(n^2 + \lambda^2\right)^2} \right\} \tag{2.3}$$

Handbooks [62] report also the following equation, suggesting to use $\mathtt{KF_2}$=0.8:

$$p_{cr}^{Roarks} = \mathtt{KF_2} \frac{0.92E}{\frac{L}{R}\left(\frac{R}{t}\right)^2} \tag{2.4}$$

The buckling equations 2.2 2.3, and 2.4 have been compared each other by considering as case study a cylindrical shell with a mean diameter of 265 mm and an axial length of 500 mm. Three different materials have been analyzed, for each of which the shell thickness has been chosen so that $p_{cr}^{\mathtt{SP-8007}} \approx 1.5 \cdot 50$ MPa, resulting in t=13.8 - 11.6 - 11.0 mm for Ti6Al4V, Inconel and NiBe 440 respectively. The results have been reported in Fig.2.7.
Von Mises equation (Eq.2.3) overestimated the critical pressure, while a good agreement between `NASA` standards (Eq.2.2) and handbooks (Eq.2.4) has been found, especially when β has been let varying continuously. For this reason, Eq. 2.2 will be used in the following sections.
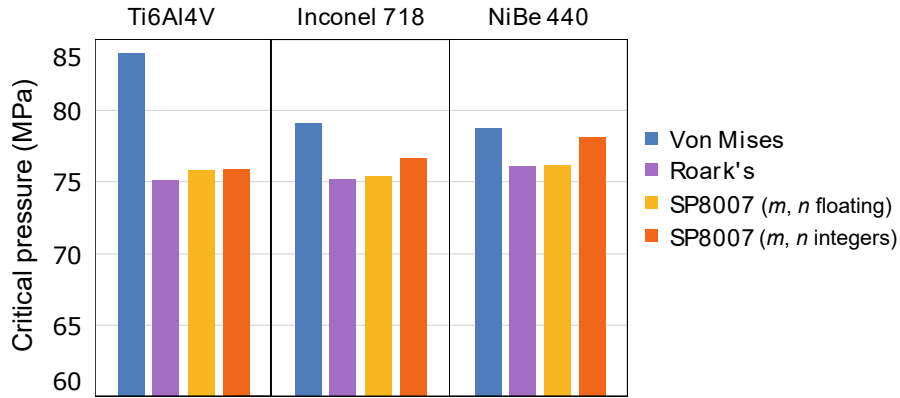
Figure 2.7: Comparison among different buckling equations.

Selected the buckling model, the influence of the bay length on the structural behavior has been investigated. According to Eq. 2.2, the buckling critical pressure

is a complex function of l, as it is included in both β and Z parameters. Generally speaking, decreasing the bay length results in an increased buckling critical pressure, as more clearly shown by Eq.2.4. Hence, shorter bays allow to reduce the shell thickness, resulting in lighter structures.

The effect of the bay length on the bay mass has been investigated for a range of design pressures, using as a NiBe alloy as the reference material. As reported in Fig.2.8, three bay length have been investigated (250, 500 and 1000 mm). It is easy to understand that a long unstiffened bay is not an option, resulting in a thick and heavy shell. This lead to the adoption of architectures with relatively short modular bays (500 mm), connected by radially stiff bulkheads.
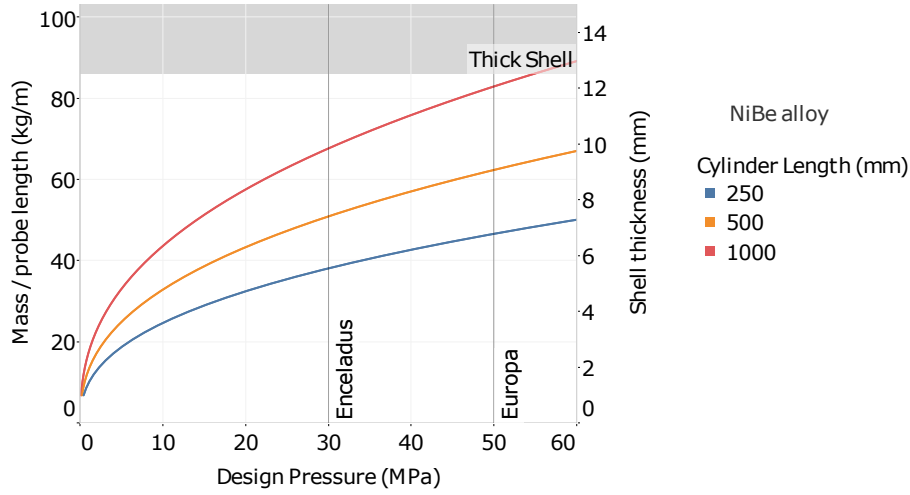
Figure 2.8: Effect of the bay length on mass and shell thickness (NiBe alloy)

Then, selected a bay length of 500 mm, different materials have been compared, as shown in Fig.2.9. Results are plotted considering shell thickness (horizontal axis), mass per unit of probe length (vertical axis), type of alloy (color and label) and a thermal parameter K (marker size), calculated by dividing the thermal conductivity by the shell thickness, considering the Fourier law for thermal conduction:

$$q = -k\frac{dT}{dr} = -\frac{k}{t}\Delta T = -K\Delta T \Rightarrow K = \frac{k}{t} \qquad (2.5)$$

where q is the heat flux, k is the thermal conductivity, t is the shell thickness and ΔT is the temperature difference between inner and outer surface. The parameter K is an indicator of the thermal performance of the shell, taking into account both the material properties and the geometry: highest is the K (i.e. high thermal conductivity and thin shell), better the heat can be transported from the power generators to the external surface, in order to melt the ice. Beryllium alloys
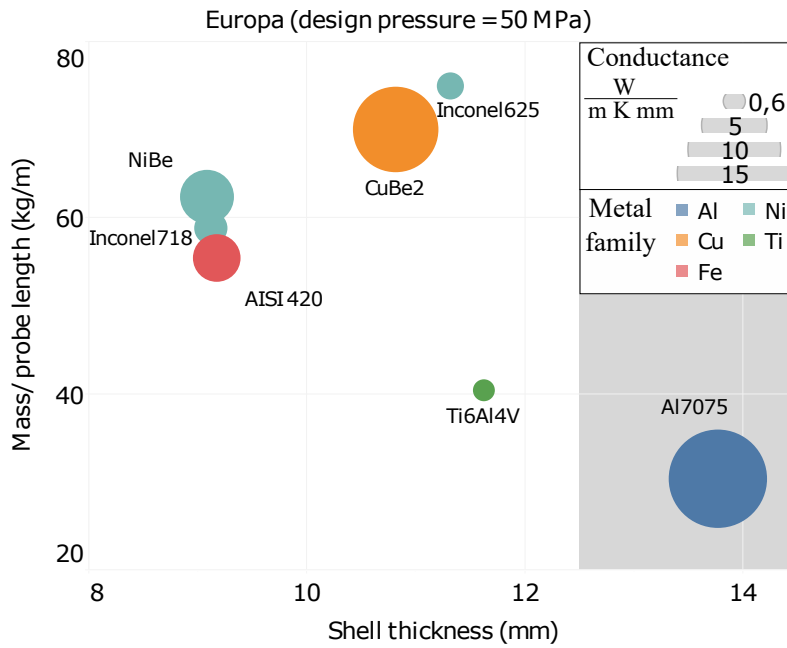
Figure 2.9: Optimum designs, considering Europa loading conditions

are very promising materials, especially from the thermal point of view, providing high K values, even if the high density of Nickel and Copper result in heavy structures. On the other side, Ti6Al4V shows excellent structural performance, but it is characterized by poor thermal properties.
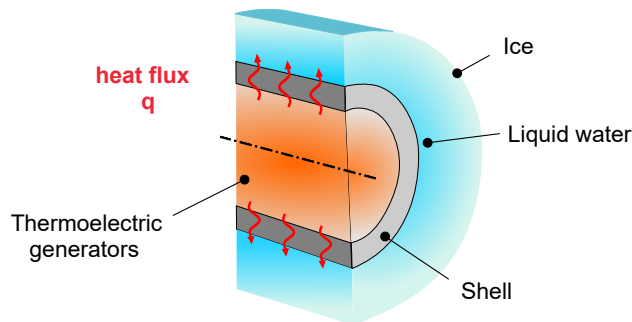
Figure 2.10: Scheme of the heat flow, from the `RTG` to the external surface of the probe

This first study on plain shells provided the opportunity to investigate the behavior of cylindrical shells subjected to external pressure loading, analyzing how bay length and material properties can affect the design. The analytical method resulted easy to implement and very convenient in the early design stages, when rough estimations of the overall geometry and mass are needed and the configuration of the entire probe is often subjected to drastic changes.

2.6   Ring stiffened shells

The preliminary analyses on plain cylinders showed that the most critical failure mode is instability. To increase the flexural stiffness, and so improve the buckling stability, ring stiffeners have been added on the internal surface.

The new configuration consists in l=500 mm cylindrical modular bays, stiffened by a number of rectangular cross section rings and bulkheads (R=90 mm, t=25 mm) at the ends, as shown in Fig.2.11. Rigid bulkheads provide additional stiffness and the location for welded or bolted connections. Moreover, they limit the interactions between bays in both static and buckling conditions, allowing the adoption of sub-models for the simulations. The determination of the optimum geometry (shell thickness, spacing and geometry of the stiffeners) that minimizes the mass turned out to be a never trivial problem, given the high external pressure and the limitations on inner and outer diameter.
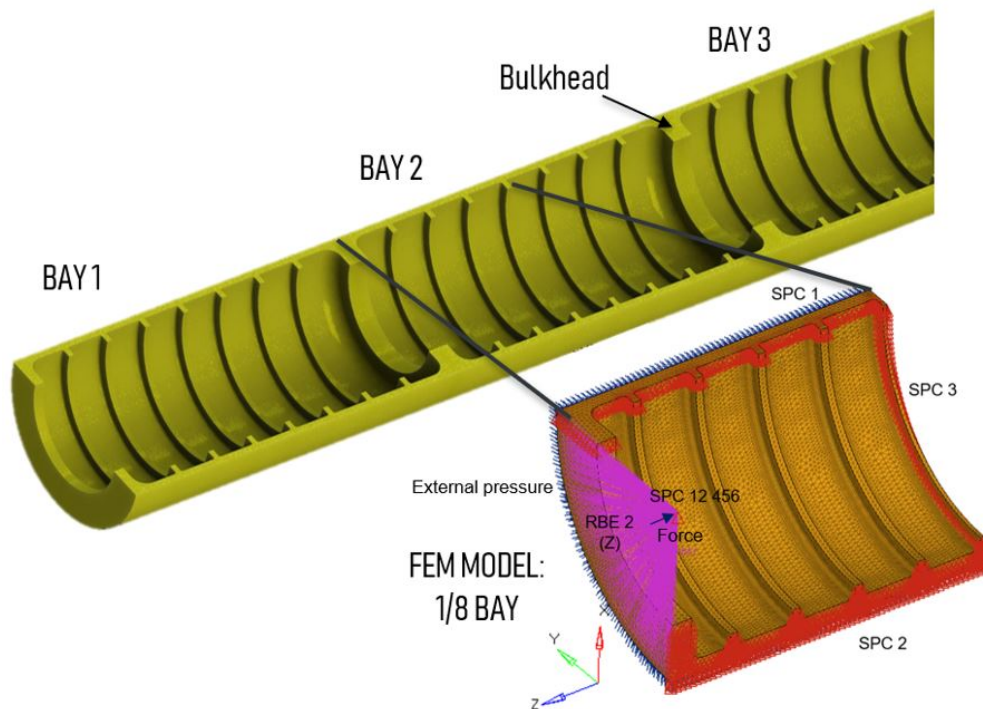
Figure 2.11: Ring-stiffned shell: geometry and `FE` sub-model

A Finite Element Analysis – based approach has been used to design the bay. A single bay has been modeled in Altair Hypermesh®, taking advantage of 3 symmetry planes. As the midplane of the bulkhead is supposed to stay planar and normal to the axial direction of the probe, the nodes on that surface have been constrained

using rigid elements (RBE2), so that they share the same axial displacement. Uniform external pressure has been applied on the external lateral surface, while an axial force simulates the pressure acting axially. The geometry has been meshed using tetrahedral elements (CTETRA, average size 1 mm, 40 000 nodes). A linear elastic material model has been used and Linear Static Analysis and Linear Buckling Analysis have been performed using MSC Nastran®.

To check the validity of the boundary conditions set at the interfaces, the sub-model (1 bay, 40 000 nodes) has been compared to a bigger model, formed by 3 bays (120 000 nodes). It has been found that stress, radial displacements and buckling load factor full agree, proving that the presence of the rigid bulkhead allows to decouple the behavior of single bays and makes possible the adoption of sub-models.

A parametric design and optimization process has been set up in Siemens HEEDS®, linking the `CAD` model (written in Solidworks®) to the pre-processor (Altair Hypermesh®), to the solver(MSC Nastran®), to the post-processor (Siemens HEEDS®), as shown in Fig.2.12. Mass, maximum displacement, maximum Von Mises stress and buckling load factor (defined as the ratio between the critical pressure and the design pressure) have been defined as Key Performance Indicators, to be monitored by the optimization algorithm. At each iteration, the `CAD` geometry is updated, meshed and analyzed. Goal of the activity is to optimize the ring-stiffened layout, sizing the shell thickness, as well as number, height and thickness of the ribs.
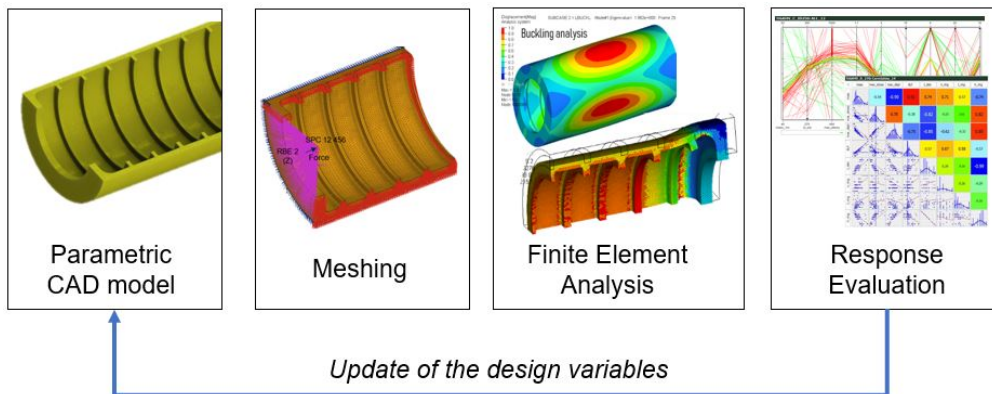
Figure 2.12: Optimization process set-up in Siemens HEEDS®

According to an initial configuration of the probe, the inner diameter of the vessel has been set equal to `ID`=230 mm and the outer diameter equal to `OD`=270 mm. Three materials have been considered: Ti6Al4V, CuBe2 and NiBe alloys.

The optimization has been performed and the optimal configurations have been

listed in Table 2.1.

The Margin of Safety against yielding (MoS_y) as been calculated as:

$$\text{MoS}_y = \frac{\sigma_y}{\sigma_{\text{VM}}\text{SF}_y} - 1 \tag{2.6}$$

where σ_y is the Yield stress, σ_{VM} is the Von Mises stress obtained by analysis, and SF_y is the yield safety factor.

Ti6Al4V and CuBe2 optimum layouts are really similar, because of the similarity in the mechanical properties. By the contrast, the NiBe layout presents larger margins of safety, suggesting that the constraint on the OD is probably leading to sub-optimal layouts, i.e. the optimum OD for NiBe is probably smaller than 270 mm. Based on the results of the simulations, correlation matrices have been plotted, as shown in Fig.2.13. The number and the thickness of the rings affect the buckling behavior, while their influence on the maximum stress is limited; in addition, a high correlation factor links the maximum stress to the skin thickness.

Table 2.1: Ring stiffened configurations

Material	Mass kg/m	MoS_y	λ	t_{skin} mm	n_{ring}	t_{ring} mm	h_{ring} mm	K W/m-K-mm
CuBe	60	0.01	1.87	6.0	4	4.7	14.0	15.8
NiBe	64	0.54	2.03	6.5	2	4	13.5	4.9
Ti6Al4V	35	0.02	1.90	6.5	4	7	13.5	1.1

The optimization approach here proposed, linking together CAD, meshing and simulation tools, is particularly useful in the early design stage, when the overall configuration is frequently subjected to changes. In addition, the process can be set-up in order to monitor a number of responses, even if they are not explicitly defined as optimization targets or constraints. The main limitations are related to practical difficulties in the meshing process, to possible numerical peaks and to high computational time. In this case, a large number of solid elements was needed, in order to take into consideration the thick shell, the fillets and possible small features.
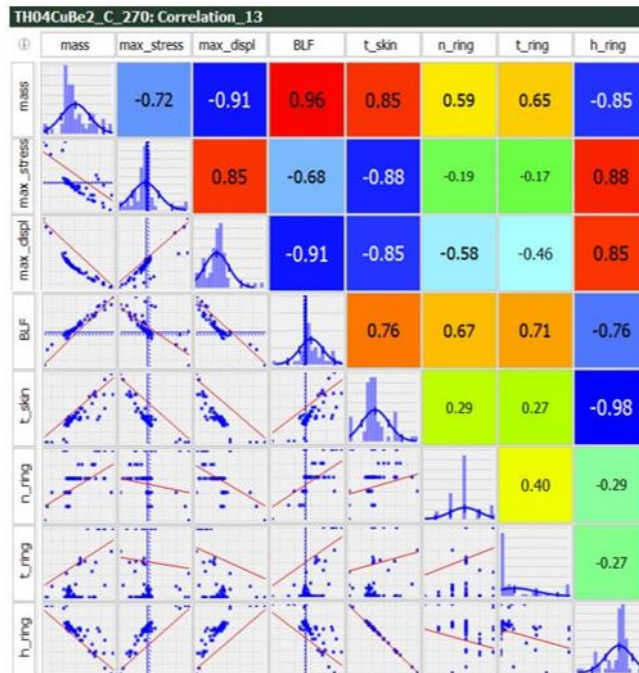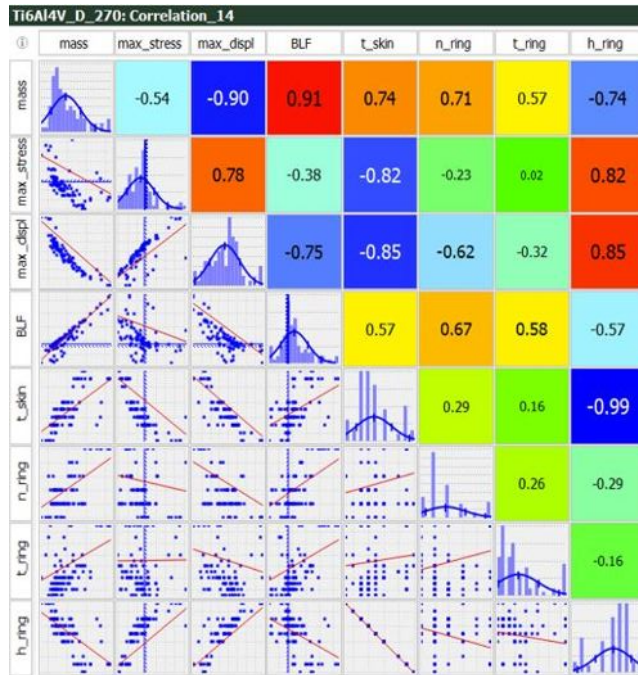
Figure 2.13: Correlation matrices for the Ti6Al4V case(left) and the CuBe case (right)

2.7   Thermo-structural shells

The last step of this case study has been represented by investigating multi-functionality. Integrating the heat pipes in the structural shell could result not only in better structural and thermal performance, but also in time and cost savings, because of reduced assembly operations. The effectiveness of `AM` in manufacturing heat pipes has already been proven in literature; potential issues related to the dimensions of the probe could be solved adopting modular bays and junctions, using for instance bolted interfaces or friction stir welding.

A number of 20 to 40, d_{HP} =6mm Heat Pipes has been included in the geometry. A new `FE` model has been created, having smaller elements to catch the stress concentration near the Heat Pipes. To reduce the computational cost of the analysis, especially during the optimization loop, only a portion of the vessel has been modeled (Fig.2.14, 270 000 nodes, 170 000 elements) and only the static analysis has been performed. The results of the previous optimization (where heat pipes were not included) have been used as starting point: the number of rings has been fixed, while skin thickness, ring shape, location and shape of the heat pipes have been considered design variables.
Obtained the optimal layout, one final run has been performed, considering the entire bay and both static and buckling analysis.
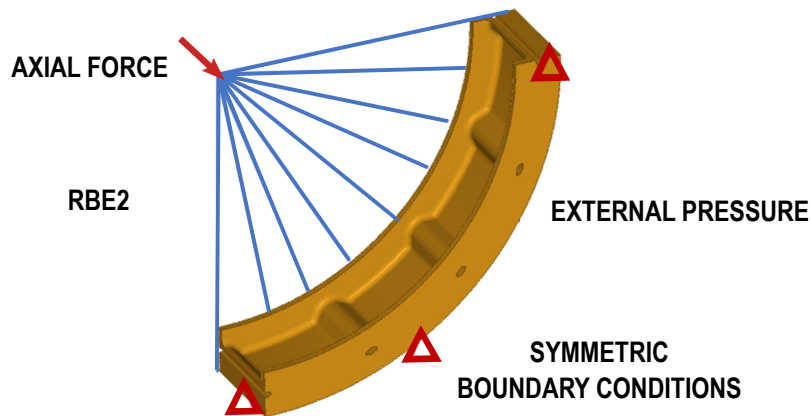
Figure 2.14: `FEM` sub-model relative to the configuration having the heat pipes running on the internal surface

Three different geometries have been considered, having the heat pipes located on the internal surface, on the external surface or in the mid-thickness of the shell, as shown in Fig.2.15. Ti6Al4V has been used as reference material, due to its high specific strength and stiffness, and to the maturity of the technology.
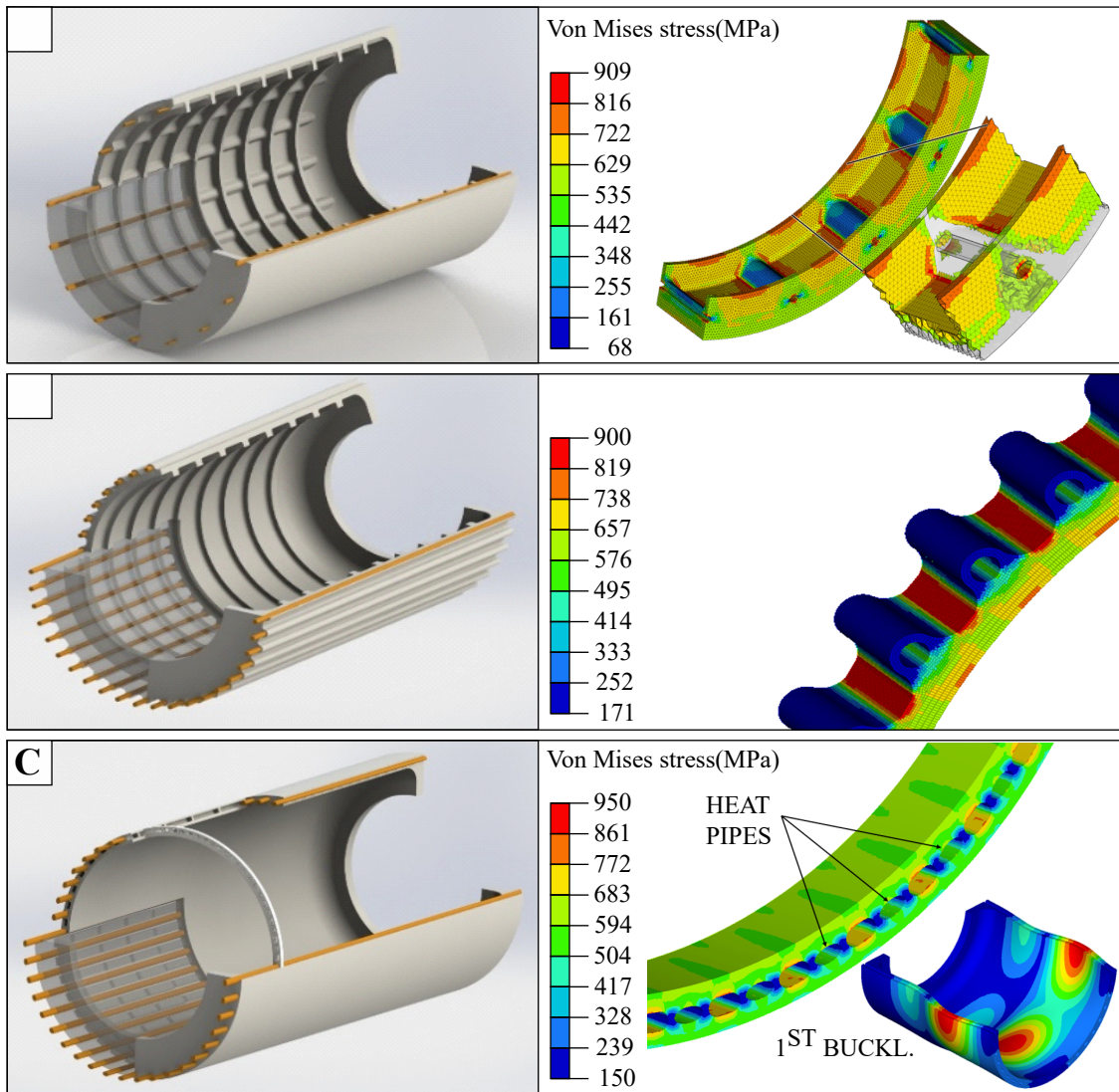
Figure 2.15: Layouts of integrated thermal control systems. From the first to the third row: internal channels, external channels and sandwich layout. In the left column: details of the stress distribution for the three configurations proposed

At first, heat pipes have been placed near the internal surface. Studying the effect of heat pipe size and shape, it has been noted that smaller, oval cross-sectional pipes reduce the stress concentration. However, heat pipes have to be located relatively far from the external surface, to limit the maximum stresses. This resulted in thicker shells, degrading the thermal performance.

To make the most of the structural properties of pipes, a new design has been developed, having the pipes on the external surface. This layout, even if efficient from the structural point of view, makes more critical the resistance to abrasion or

corrosion and presents several drawbacks from the thermal perspective, causing a less uniform temperature distribution and increasing the complexity of the models for the thermal simulations and for the prediction of the time to descent to the ocean.

Finally, the Heat Pipes have been integrated into the skin: the geometry of the rings has been kept, while the skin thickness has been increased and a topology optimization has been performed, in order to minimize the mass. As expected, the material in the mid-thickness is characterized by low stress and can be removed; the result is a sandwich structure, more efficient in both the static and the buckling condition and characterized by plain internal and external surfaces. The thickness of the inner and outer skin has been iteratively modified, in order to limit the stress and minimize the mass. As an example, `FEA` results for Ti6Al4V are reported in Fig.2.15. The optimized configurations exhibit a good buckling resistance, due to the high flexural stiffness provided by the sandwich layout, and high thermal performance, being the heat pipes located close to the external surface. However, stress concentrations near the heat pipes limited the mass saving.

Sandwich configuration made of NiBe and Inconel 718 have finally obtained similarly to what done for Ti6Al4V, as reported in Table 2.2. In respect to Ti6Al4V, NiBe and Inconel are characterized by higher mass density and resulted in heavier configurations, even if the the thickness of the skin was lower. According to this preliminary assessment, NiBe alloy could provide a very strong choice, especially from a thermal point of view, because of both high thermal conductivity and very thin shell thickness, according to Table 2.2. Further investigations should be performed, by recurring to more accurate non linear analysis. Moreover, manufacturability assessments should be performed, as NiBe alloys are currently not available for `AM`.

Table 2.2: Integrated thermal control system – Configurations

	Material	Mass kg/m	OD mm	t_{skin}^{out} mm	t_{skin}^{in} mm	n_{ring}	t_{ring} mm	h_{ring} mm	n_{HP}
Internal Channels	Ti6Al4V	52	294	8.1	N/A	5	6.7	13.8	20
External Channels	Ti6Al4V	51	298	7.6	N/A	5	8	12	40
Sandwich	Ti6Al4V	54	285	4.5	6	5	6.7	5	40
Sandwich	NiBe	68	271	2	3.5	5	4	8.5	40
Sandwich	Inconel	90	278	4	5	5	5	10	40

2.8 Preliminary conclusion

In-situ missions for the exploration of Europa's internal ocean are currently under study. Additive Manufacturing could be a key technology, enabling the fabrication of optimized structural shell, with integrated thermal control system, such as heat pipes.

The activity described in this chapter regarded some preliminary assessments of materials and layouts for primary structures for a meltprobe concept, to be fabricated by `AM`. A material trade-off study has been performed, considering Europa's harsh environment, as well as requirements and needs of structural and thermal systems. Analytical and numerical methods have been used for the first sizing of plain, stiffened and multi-functional cylindrical shells subjected to high external pressure.

A parametric design method have been proposed, in which `CAD`, meshing and simulation tools are linked together within the optimization loop, and results of the simulations are post-processed in correlation matrices. The parametric design approach has been found to be very effective during the early design stage, when the requirements and the overall configuration is frequently subjected to modifications. In addition, it allows to monitor multiple responses, which may have a weak influence of the structural behavior, but may strongly affect the performances of other sub-systems.

This design activity provided a preliminary testing ground for investigating typical requirements and issues related to the design of primary structures for harsh environments, considering both structural and thermal phenomena, and assessing also potential benefits of `AM`.

Chapter 3

Test case: a concept design of a Venus lander

The concept study of the Europa meltprobe, described in the previous chapter, provided the opportunity to approach the typical issues related to the design of structures for probes for harsh environments, investigating the potential benefits related to the adoption of `AM` techniques. The object of this dissertation has been provided by a research and technology development activity, regarding a concept for a Venus lander, in which the primary structure consists in a `AM` lightweight spherical shell, potentially integrating a thermal control system.

Very similar to Earth in structure, size, and distance from the Sun, Venus is considered as the Earth's twin. It is also thought to host oceans in the past, but a severe greenhouse effect has made its atmosphere inhabitable today. In fact, Venus atmosphere is characterized by a thick layer of carbon dioxide gas at high pressure and temperature, surrounded by clouds made of sulfuric acid. Surface pressure and temperature are 93 bar and 462°C [63, 4]. The reasons behind the different evolution paths of Earth and Venus are still unknown. New space missions to Venus could lead to a better understanding of the origin and the evolution of Venus, the Earth and Earth-like planets. Additionally, with climate change becoming a more pressing issue in our time, understanding an analog atmosphere could help scientists identify better ways to address this issue [64].

This chapter gives a quick overview of past Venus in-situ exploration, summarizing past missions and concepts for the future. Landing missions will be briefly discussed, considering the main challenges to be addressed and typical probes architectures. Finally, attention will focus on the structural sub-system, which be the object of the following chapters.

3.1   Past missions

The exploration of Venus started in the early '60s with the Soviet program Venera and the `NASA` Mariner. In the following decades, Venus has been the scene of an impressive number of missions, including orbiters, flybys and landers. The milestones of the history of Venus exploration [65, 66, 67] are briefly reported below, together with some images (Fig.3.1).

1962 Mariner II flew by Venus, being the first successful planetary mission in history. The data gathered by the radiometers of the spacecraft revealed the presence of clouds and high temperatures.

1967 Venera 4 was the first successful entry probe. It transmitted data while descending through the atmosphere, providing measurements of pressure (up to 76 bar), temperature (up to 500 C) and chemical composition. It failed before reaching the surface, because of the harsh environmental conditions. Venera 4 provided a great scientific return, and it enabled improvements in the design of the following probes. In the same year, Mariner V reached Venus orbit, providing additional information about the planet environment.

1970 In order to land on the surface of Venus, Venera 7 was designed considering more severe conditions, such as a design pressure of 150 atm and a temperature of 540C. After a partial failure, the probe landed and survived for 23 minute, measuring an external temperature of 475 C and, indirectly, a pressure of 92 bar.

1972 Venera 8 was designed considering the data provided by the previous mission. After descending and touching down, it transmitted data for 63 minutes. The instruments confirmed Venera 7 measurements about surface pressure and temperature and provided more information about the soil composition and the illumination at the surface level.

1975 With Venera 9 and 10, a new spacecraft architecture was adopted, composed of a lander module and an orbiter module, in order to carry more instruments and better transmit the data. Both Venera 9 and 10 successfully landed and took the first photos from the surface of another planet.

1978 Pioneer Venus missions were composed by an Orbiter mission and a Multiprobe mission, both launched in the same year. The first one orbited around Venus, mapping the surface using radar technologies, measuring the magnetic field and observing the planet using cameras. The Multiprobe spacecraft was composed by a bus, carrying one Large (R = 78 cm) and three small (R = 47 cm) probes, designed to entry and descent through Venus atmosphere. Although the probes were not designed to survive he landing, one of the small

probes continued sending back data for more than one hour. The mission resulted in a great scientific return, providing a detailed map of pressure, temperature and structure of Venus atmosphere.

1981 After the partial failure of Venera 11 and 12 in 1978, which had some issues with the instruments, the twin probes Venera 13 and 14 successfully landed on Venus in 1981, surviving on the surface for 127 min and 57 min respectively. The probes provided the first color images of the surface of Venus and analyzed a soil sample, obtained by mechanical drilling.

1985 Vega 1 and Vega 2 were challenging missions aimed to the exploration of the surface and the atmosphere of Venus, as well as the Halley's comet. In fact, the spacecraft was composed of a lander, a balloon with a gondola and a bus, which flew by Venus and continued its travel to Halley's Comet. The landers descended through the atmosphere, deploying the balloons, before landing on the surface, where they survived for nearly one hour.

1990 In 1989, the Space Shuttle Atlantis deployed the spacecraft Magellan. Starting from 1990, Magellan radar-mapped more than 96% of the surface of Venus, providing high-quality images and the evidence of tectonic movements and volcanism.

2006 The European orbiter Venus Express was the first spacecraft to perform long-duration observations of Venus atmosphere, operating for almost 10 years. It provided evidence for past oceans.

2015 Akatsuki probe, currently orbiting around Venus, is observing the atmosphere of the planet, studying its dynamics and the structure of the clouds.
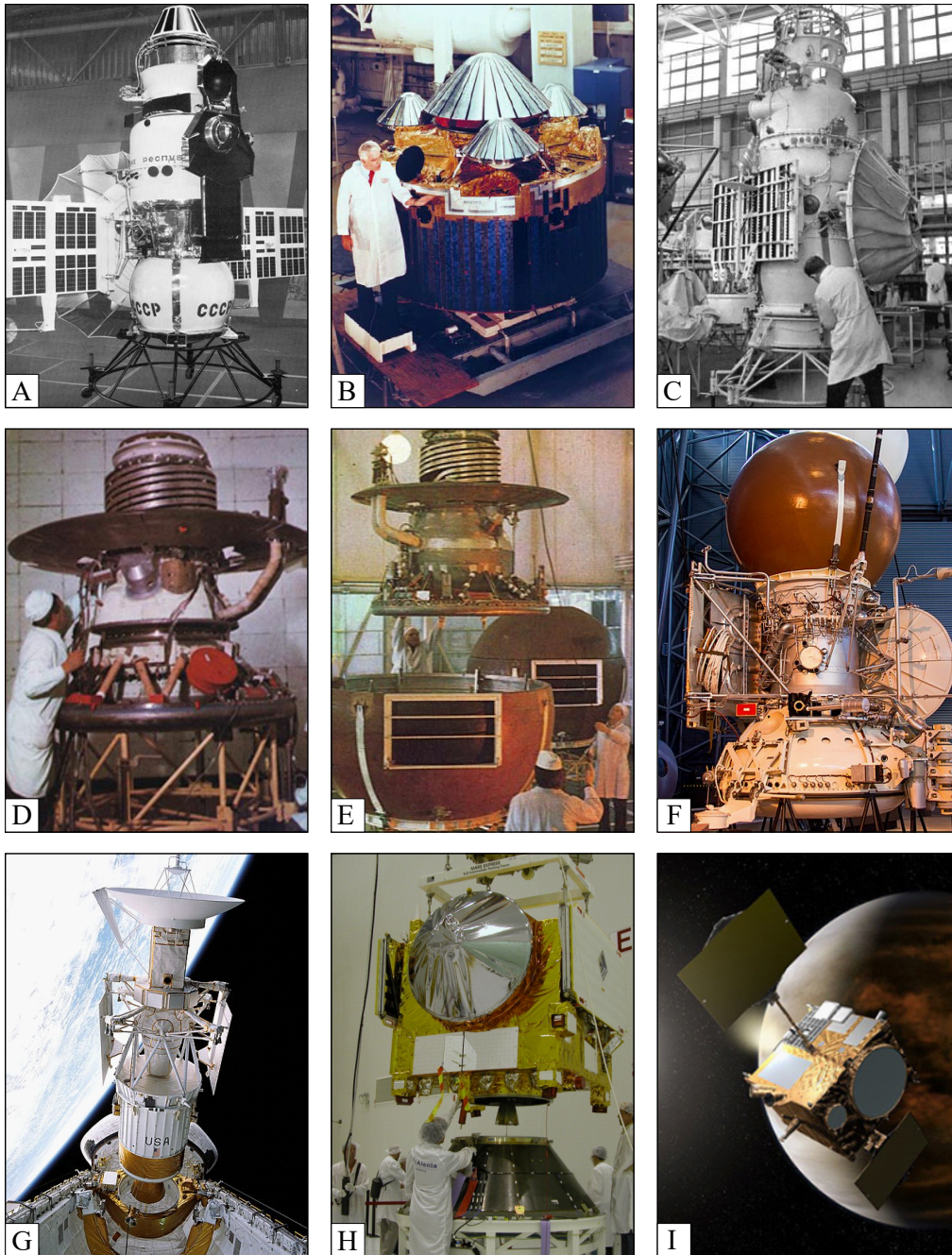
Figure 3.1: Images of past missions to Venus: A) Venera 4 probe, B) Pioneer Venus Multiprobe spacecraft: bus carrying the probes during the integration activities, C) Venera 7 probe, D) Venera 11 lander, E) Venera 13 lander during integration in the entry module, F) Vega spacecraft, carrying the lander in the sphere at the top, G) Magellan orbiter being deployed by Space Shuttle Atlantis, H) Venus Express orbiter at the Integration Facility in Baikonur, I) Venus Climate Orbiter Akatsuki

3.2   Mission concepts

Despite nearly 60 years of exploration, many scientific questions about the Earth's Twin are still unsolved. The planetary science community has identified Venus as a high-priority destination for scientific exploration. According to the Venus Exploration Analysis Group (VEXAG), three main scientific goals need to be addressed [68]: understanding the early evolution of Venus and its potential habitability, understanding the atmospheric composition and dynamics, and understanding the geologic history preserved on the surface of Venus and the present-day couplings between the surface and atmosphere. Each Goal can be decomposed in two more specific Objectives, for each of which several Investigations need to be performed. Based on these scientific needs, mission concepts can be described [7], including orbiters, entry probes, balloons, landers, and multi-element architectures. Finally, concepts must be discussed from an engineering point of view and considering their readiness, based on technology maturity, complexity and resource needs [69]. A landed mission has been targeted as a mid-term goal, with proposed payloads including instruments to study surface chemistry, mineralogy, or seismology. An overview of mission architectures is outlined in Fig.3.2.

Several concepts for Venus landing missions have been proposed over the last decades, including a number of different spacecraft architectures, systems and subsystems [70, 71, 72]. The Venus Flagship Study Report [72] has recommended a multi-element architecture, which may include an obiter, two balloons and two short duration landers. In addition to the intrinsic high flexibility of a multi-element mission, the interconnection between platforms and instruments could significantly enhance the science return. The main functional requirements of landing missions may include investigating the chemical composition of the soil, measuring pressure, temperature and the chemistry of the atmosphere during descending, imaging the morphology of the surface, measuring the magnetic field. Generally speaking, landing missions to Venus are typically composed by the launch phase, an approximately 6 month cruise to Venus, the deployment of the entry element, the Entry-Descent-Landing phase, and, finally, the operations on the surface of the planet. Each mission phase is characterized by challenging issues to be solved. From an engineering point of view, the operations on the surface are particularly critical, due to the harsh environmental conditions, which reduce the lifetime and strongly limit the science return, making the landing probe one of the biggest design challenges.
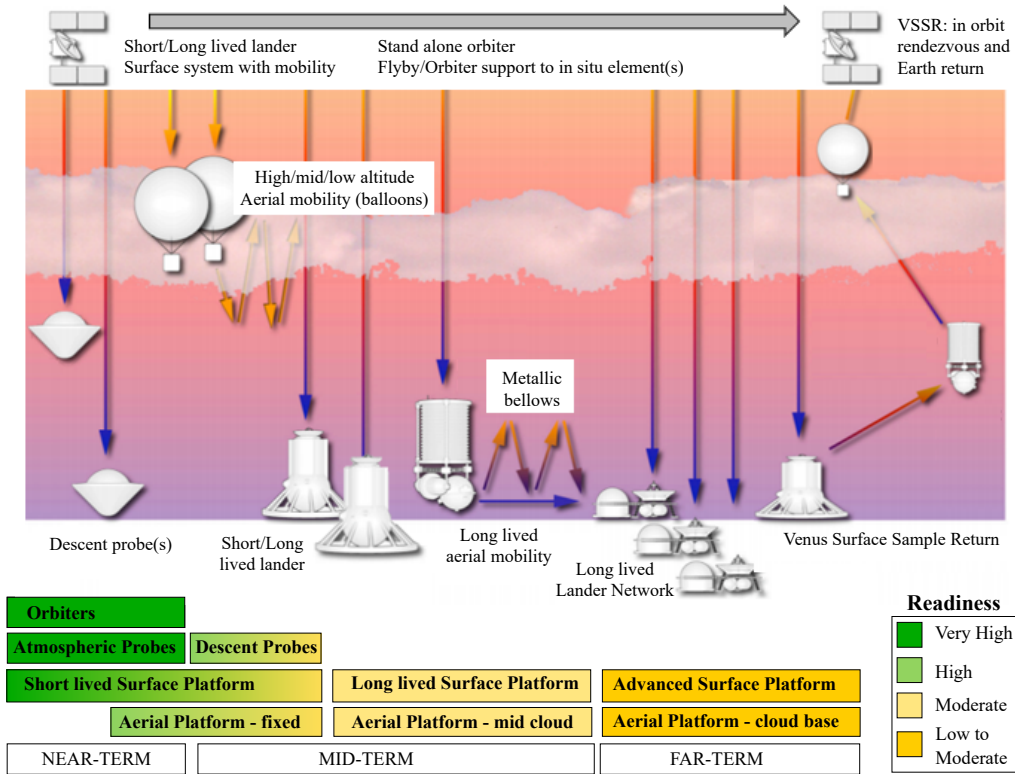
Figure 3.2: Mission architectures for Venus exploration, grouped by their readiness, adapted from [8, 7]

3.3 System concepts

Concepts for near-term and middle-term future missions usually consider short-duration landers, with a typical lifetime of few hours. These solutions are characterized by conventional electronic components, that are kept within the operational temperature range by using passive control systems, such as insulating materials, or phase change materials. Concepts for mid- and long-duration probes, with a lifetime of days or weeks, are under investigation as well, but they require more complex and expensive solutions, including active thermal control and refrigeration systems and/or high temperature electronics, still under development. As an example, a tree of the main subsystems of a typical Venus lander is shown in Fig.3.3, together with an overview of possible options.

The present work is focused on the structural subsystem for concepts of short/middle duration landers. The main requirements are listed below:

- survive to launching and landing loads, providing secure load paths and interfacing with landing legs,
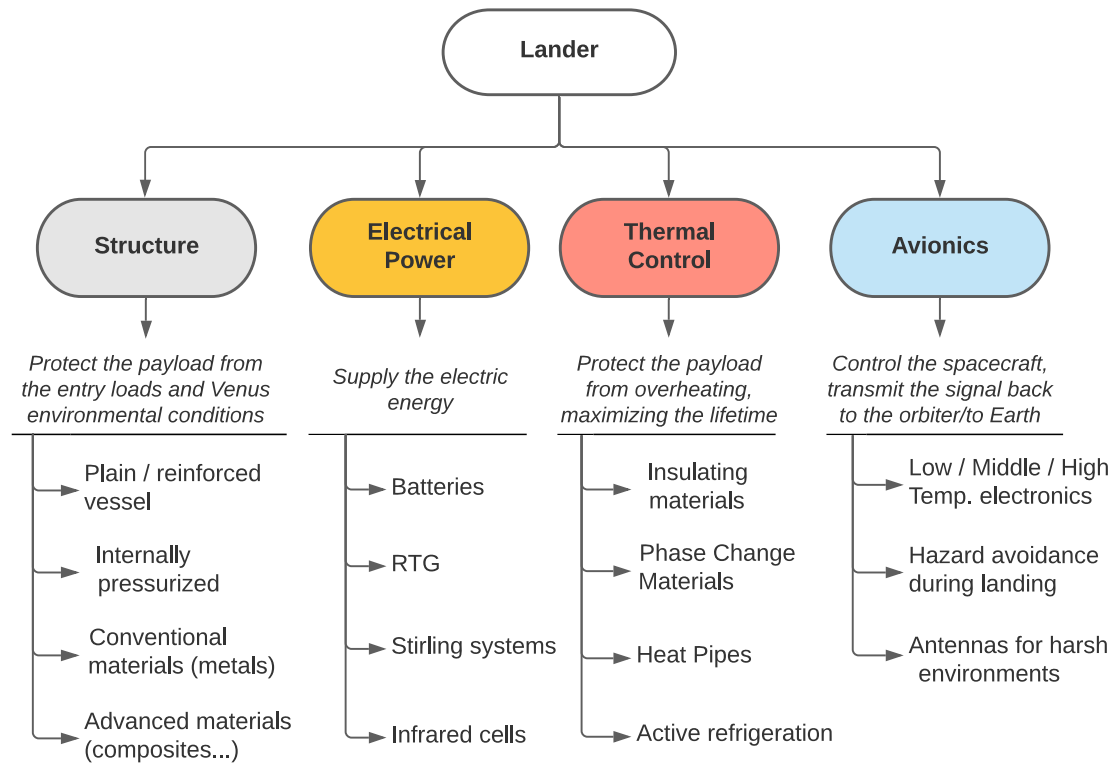
Figure 3.3: Key systems and subsytems of concepts of Venus landing probes

- withstand the extreme environmental conditions (temperature, pressure and corrosion) for the lifetime duration defined by the mission requirements,

- accommodate the lander subsystems and the scientific payload, providing instruments windows and vents to access the external environment and providing access for the integration,

- fit in the aeroshell element.

The main function of the structural subsystem is to protect the payload from the entry and landing loads and from the high pressure (93 bar) expected on the surface. For this reason, high strength materials are preferable, to prevent yielding, and with high elastic modulus, to limit instability and vibrations. In the material selection, the corrosive environment of Venus should be considered as well, limiting the choice to corrosion-resistant alloys or using protective coatings. Moreover, lightweight materials should be used, in order to limit the structural mass of the lander. The design of the primary structure, however, is not driven by the structural requirements only.

Indeed, as a part of a system, the structure must interface with the other subsystems, and in particular with the thermal control system, which can probably be considered as the most critical one. Indeed, as mentioned before, mission goals and architectures depend on the lifetime of the lander, which is strictly related to the management of the thermal energy, especially when medium/low temperature electronics are used. In this frame, most of the past missions and new concepts [65, 70, 71, 72] have used spherical vessels to protect the subsystems and the payload, in order to minimize the area exposed to Venus environment, given the required internal volume. For instance, as shown by the cutaways reported in Fig.3.4, Venera probes were composed of a monocoque spherical shell, and Pioneer Large Probe was made of 3 flanged parts, assembled together in a sphere and sealed with o-rings. The concept for a spherical lander proposed for a Flagship mission [72] is shown as well, together with a possible accommodation of instruments and subsystems.
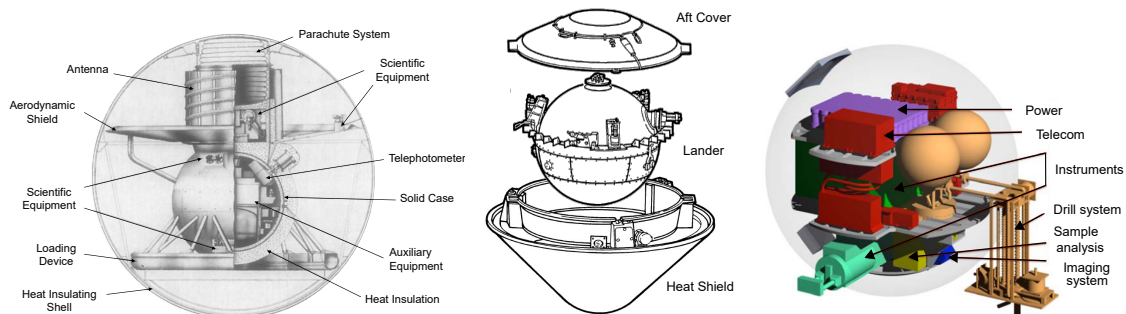
Figure 3.4: Venera 9 and 10 landing probes [73], Pioneer Large Probe, Concept of a Venus Flagship mission [72]

In most of the configurations, the spherical pressure vessel is surrounded by a multi-layer structure of insulating materials to protect the payload form the external extreme temperature. To further increase the lander lifetime, solid/liquid or liquid/vapor Phase Change Materials can be used as well to cool the electronics, by using the latent heat. Although the pressure vessel can be considered mainly as a structural component, thermal properties must be take into account during the design phase, preferring low conductive materials to limit the heat flux from the exterior. Moreover, cooling systems are currently under development and concept studies for Venus landers have shown promising results. For instance, a two phase system with expandable fluid has been proposed by Lee et al. [74] (Fig.3.6). A fluid is used to cool the electronics with its latent heat of evaporation; then, the vapor flows in channels located near the skin of the pressure vessel, and it is finally vented outside. A gas tank and a system of valves is used to control the pressure of the fluid and the evaporation temperature. Two phase cooling systems with evaporators integrated into the structural shell are under study as well [34].

46
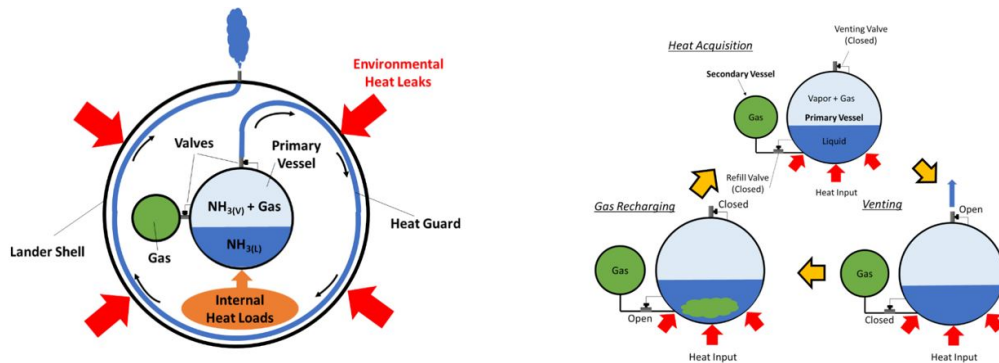
Figure 3.5: Two-phase thermal control system proposed by Lee et al. [74]

Integrating the thermal channels or the evaporators in the vessel itself may lead to benefits in terms of thermal performance and mass savings, although it presents challenging integration and manufacturing issues, especially if conventional fabrication techniques are used. In the past Venus missions, for example, manufacturing and technology constraints limited the design options to plain spherical shells without stiffeners or integrated channels, fabricated by spin forming and post-machining. Recent developments is Additive manufacturing have opened new opportunities, enabling the fabrication of very complex geometries and the integration of multiple systems in a single component. In the case of vessels for Venus landers, Additive Manufacturing may allow the fabrication of stiffened shells, potentially resulting in enhanced mechanical performance and mass savings, and/or the fabrication of integrated thermo-structural shells.

Aim of this research is investigating the mechanical behavior of lightweight Additively Manufactured shells. As a reference for the case study, a concept of a Pioneer-like lander (approximately ⌀1 m) will be considered. The architecture of the cooling system is based on the two phase technologies previously described, although its integration within the structural shell will not be fully addressed within this work.

The concept of the primary structure (Fig.3.6) consists of two metallic hemispherical shells, fabricated by L-PBF, assembled and sealed with high temperature seals. The shells are internally reinforced with ribs forming a triangular pattern, commonly referred as "isogrid". The isogrid layout, although common in aerospace industry for flat panels and cylinders, has not deeply investigated in the case of hemispherical shells for external pressure vessels. This is probably related to the intrinsic complexity of the geometry, which makes isogrid hemispheres hard and expensive to be fabricated, using conventional techniques. With the development of
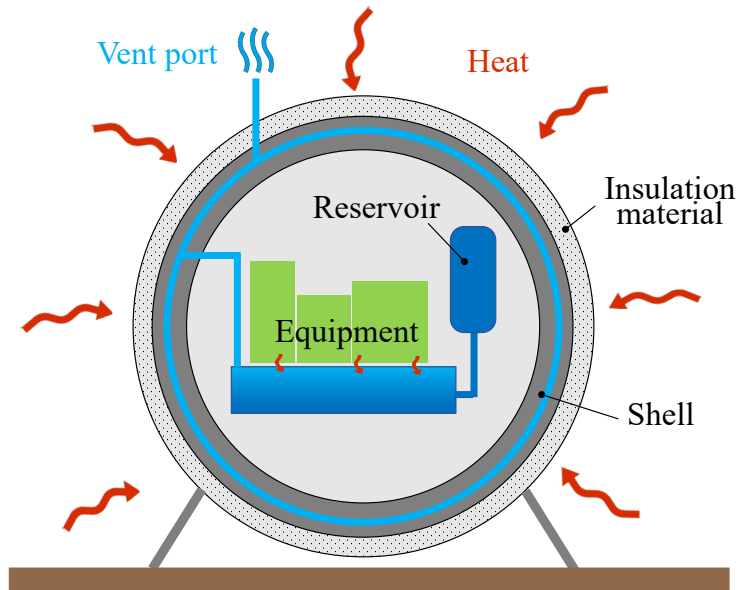
Figure 3.6: Concept of the Venus lander

`AM` techniques, complex stiffening systems, such as the isogrid, have become available also for doubly-curved geometrical shapes, such as in the case under study.

An assessment of materials and fabrication techniques was performed in 2006 by Pauken at al. [75] and identified Titanium, Nickel, Beryllium and steel alloys as potential candidates for shells for Venus probes. Among the others. At that time, `AM` was not considered as fabrication technique. In the present research, the Titanium alloy Ti6Al4V, commonly used in `AM`, will be considered, for its high specific strength and stiffness, its good creep and corrosion resistance, and for the low thermal conductivity

First, design methodologies for plain and isogrid-stiffened spherical shells will be discussed, considering the case of external pressure loading and using both analytical and numerical methods.

Chapter 4

Venus lander: System modeling

In the previous chapters, a concept of a spherical Venus lander has been proposed. The extreme environment of Venus, characterized by high atmospheric pressure, makes the design of such structures particularly challenging, as the eternal pressure loading might cause not only very high stresses, but also the structural instability of the shell. As it will be discussed in the following, difficulties are even increased when spherical shells are used, as their buckling behavior is strongly affected by geometric and manufacturing imperfections, so that complex and non-linear tool may be necessary to assess the structural performance. In the early design stage, however, predictive models, both accurate and easy to implement, are essential for performing trade-off analyses and for the preliminary sizing.

In this chapter, the case of spherical vessels undergoing external pressure loading will be presented, describing the main analytical and numerical approaches for the early design stage. Attention will be finally focused on the isogrid-stiffened layout, presenting the state of the art and proposing an optimization method based on analytical formulations.

The design formulae and approaches described hereafter will be used in the next chapter to present a first sizing of the primary structure of the conceptual Venus lander.

4.1 Plain shells: basic theory

Past landing missions to Venus adopted plain spherical shells. This section reports the main design methods, both analytical and numerical, used in the early design stage to size plain spherical vessels undergoing eternal pressure loading.

4.1.1 State of stress

Given a spherical shell with a mean radius R and a shell thickness t, undergoing uniform external pressure loading (Fig. 4.1), a spherical reference frame $< \vec{r}, \vec{\theta}, \vec{\phi} >$ can be defined, so that the relative stresses are principal. Under the hypothesis of thin shell, i.e. when $R/t > 10$, the radial stress is negligible and polar and azimuthal stresses can be written as follow:

$$\begin{cases} \sigma_r \approx 0 \\ \sigma_\theta = -\dfrac{pR}{2t} \\ \sigma_\phi = \sigma_\theta \end{cases} \tag{4.1}$$

Considering a material with isotropic mechanical properties, where E is the Young's modulus and ν is the Poisson's ratio, the strains can be calculated as:

$$\begin{cases} \epsilon_r = -\dfrac{2\nu}{E}\sigma_\theta \\ \epsilon_\theta = \epsilon\phi = \dfrac{1-\nu}{E}\sigma_\theta \end{cases} \tag{4.2}$$

Finally, the radial displacement of the shell can be obtained starting from the definition of the tangential strain, as:

$$\epsilon_\theta = \frac{2\pi(R+u_r) - 2\pi R}{2\pi R} = \frac{u_r}{R} \Rightarrow u_r = \epsilon_\theta \cdot R \tag{4.3}$$
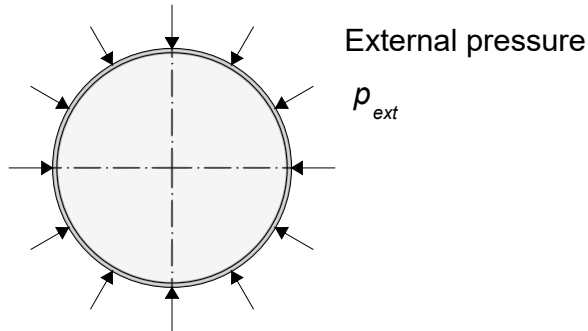
Figure 4.1: Scheme of the problem

4.1.2 Structural stability

A clear description of shell buckling is given by David Bushnell in [76]:

[in thin shells] the membrane stiffness is in general several orders of magnitude greater than the bending stiffness. A thin shell can absorb a great deal of membrane strain energy without deforming too much. If the shell is loaded in such a way that most of its strain energy is in the form of membrane compression, and if there is a way that this stored-up membrane energy can be converted into bending energy, the shell may fail rather dramatically in a process called "buckling" as it exchanges its membrane energy for bending energy.

Some experimental activities on spherical shells undergoing external pressure loading from literature are reported in Fig.4.2 to 4.4.
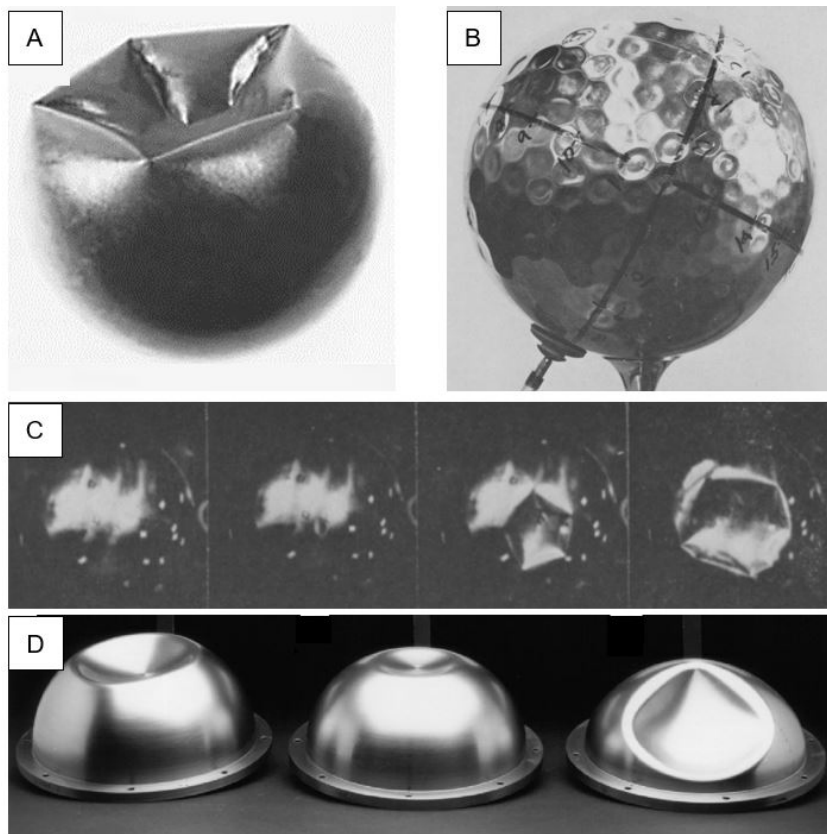
Figure 4.2: Experimental activities on spherical shells undergoing external pressure loading - examples of buckling failures: A) buckling of an electroplated copper spherical shell citeThompson1961, B) buckling mode of an electroplated nickel, with an internal wax mandrel [77], C) high speed frames of a thin nickel sphere during testing [78], D) buckling of a steel hemisphere obtained by machining [79]

Figure 4.3: Experimental activities on spherical shells undergoing external pressure loading - examples of buckling failures: E) buckled copper-steel-copper hemispheres, manufactured by spinning [80], F-G) Ti6Al4V pressure hull before and after testing [81], H-I) Carbon Fiber Reinforced Polymer hemisphere after testing, J) failure of a Poly Methyl Metachrilate dome [82], K) manufacturing of almost-perfect Vinylpolysixolane hemispheres [83]
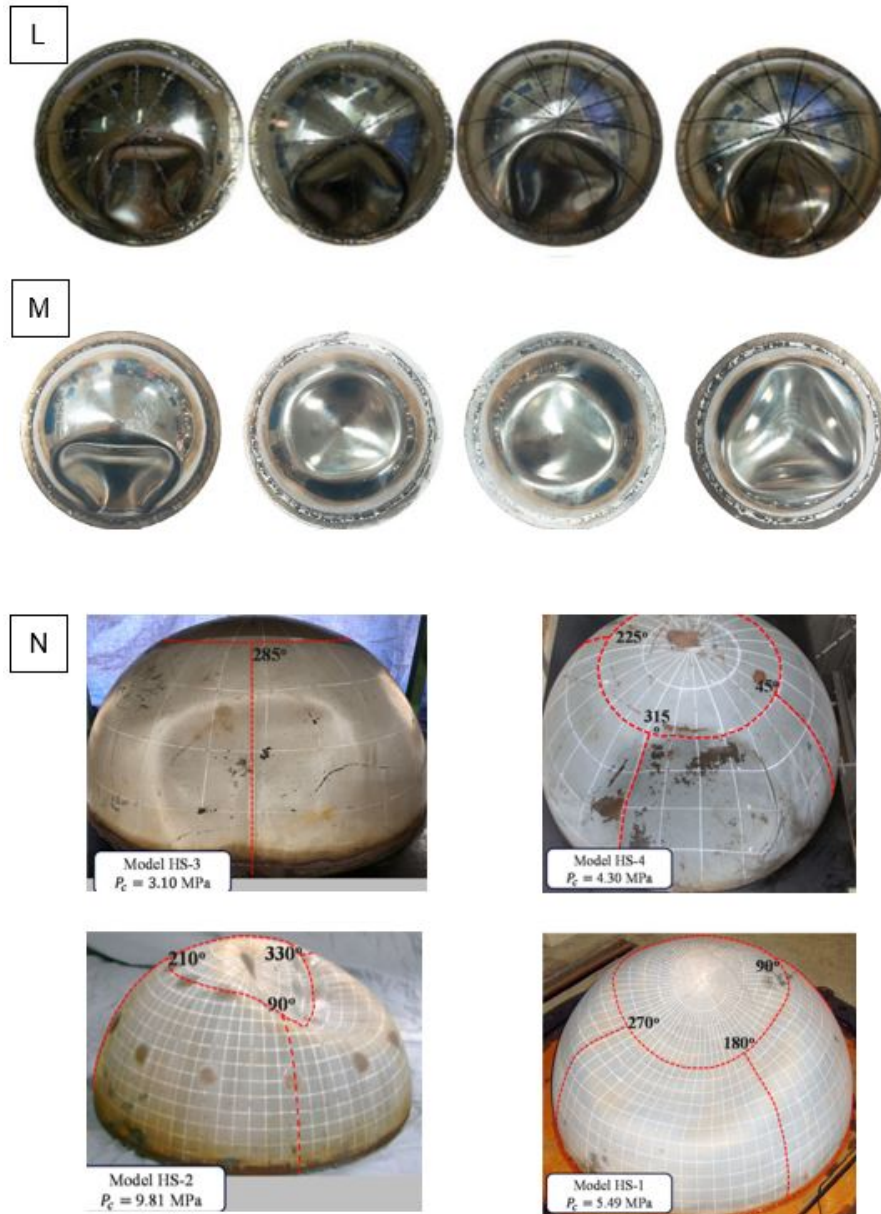
Figure 4.4: Experimental activities on spherical shells undergoing external pressure loading - examples of buckling failures: L) stainless steel hemispheres obtained by cold stamping, after testing [84], M) comparison between the buckling modes of undented and dented by conical, spherical or cylindrical indenters hemispheres obtained by cold stamping and grinding [85], N) buckling of steel welded hemispheres [86].

Zoelly [87] first studied the structural instability of a perfect thin spherical shell undergoing uniform external pressure loading. In this ideal case, the critical pressure at which instability occurs is calculated as:

$$p_{cl} = \frac{2E}{\sqrt{3 \cdot (1 - \nu^2)}} \frac{t^2}{R^2} \tag{4.4}$$

where p_{cl} is the ideal critical pressure, E is the Young's modulus, ν is the Poisson's ratio, t is the shell thickness and R is the mean radius of the spherical shell. Over the years, a number of experimental campaigns have been performed on spherical shells, considering a large range of thicknesses, radii and different materials and manufacturing processes. It has been noted that thin spherical external pressure vessels were failing at pressures significantly lower than Zoelly's estimations, and the failure pressure was strongly influenced by the fabrication technique and the ratio between the sphere radius and the shell thickness. The results of some of these past experimental campaigns have been reported in Fig.4.5 (adapted from [83]), by recurring to a *Knockdown Factor* KF, defined as follow:

$$p_{cr} = \text{KF} \cdot p_{cl} \tag{4.5}$$

where p_{cr} is the experimental failure pressure, so that when KF = 1, Zoelly's estimations are in full accordance with the experimental results, while when KF < 1, the predictions are non conservative. According to Fig.4.5, it is possible to observe that i) KF is always lower than 1, i.e. in all the cases reported in the literature Eq.4.4 lead to non conservative results; ii) the KF values are extremely dispersed; iii) KF values tend to get lower for large radius-to-thickness ration. A literature review of the past experimental works is reported in Wagner et al. [88, 89], providing a detailed historical list of the experiments.

Since the late 30s, more complex formulations have been proposed, starting from Von Karman [90] and Tsien [91], and then Koiter [92, 83], introducing the concept of sensitivity to imperfections, related to the boundary conditions [93], or the geometry [77, 78]. In particular, Thompson, Berke and Carlson [94, 78, 77] used electroplating techniques to test accurately manufactured copper and nickel thin spherical shells, to study the effects of imperfections (see Fig.4.2 A-B-C). Indeed, it was noted that spherical vessels are strongly affected by geometric imperfections, typically induced by the manufacturing process, which play a critical role in the buckling behavior, strongly reducing the load capacity.

The uncertainties in predicting the actual critical failure pressure pose significant issues in the design phase; therefore, a conservative approach is usually adopted, using Eq.4.5 with a low KF value. Recommended KF values range from 14%, according to the NASA SP8003 [95], to 25% [96], to 30%, according to industrial
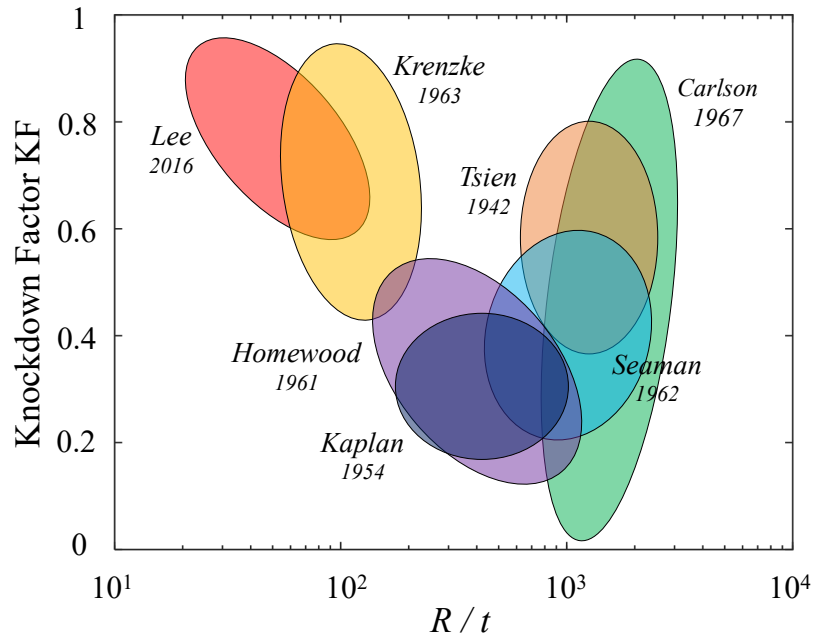
Figure 4.5: Knockdown factors versus radius to thickness ratio: experimental results from the literature (adapted from [83]

practice [62]. Obviously, this assumption has significant implications on the design and the mass of the vessel. For example, if a $\varnothing = 200$ mm external pressure vessel made of Ti6Al4V shall to be designed in order to survive to a nominal pressure of 200 bar, with a safety factor of 1.5 (i.e. expected failure pressure: 300 bar), the minimum shell thickness t can range from 2.3 to 4 mm, depending on the assumed value of KF, as shown in Fig.4.6.

Defining the required KF value can be difficult a priori, as it depends not only on the R/t ratio, but also on the accuracy of the fabrication process. A common approach consists in a preliminary design phase, supported by experimental activities on full-size or sub-scale components, aimed to assess the buckling behavior given the particular geometry and fabrication process.

In recent years, Lee, Jimenez and Hutchinson's research group [83, 97, 98] deeply studied the role of imperfections on the buckling behavior of thin spherical elastic shells, by inducing dimp-like geometric imperfections on precisely manufactured silicon-polymer hemispherical shells (Fig.4.3 K). Their experimental activity confirmed the direct relationship between geometric imperfections and the buckling critical pressure of the shells. Moreover, they developed non-linear Finite Element based and Ordinary Differential Equation-based methods able to accurately predict the critical buckling pressure, based on the initial imperfection. These efforts
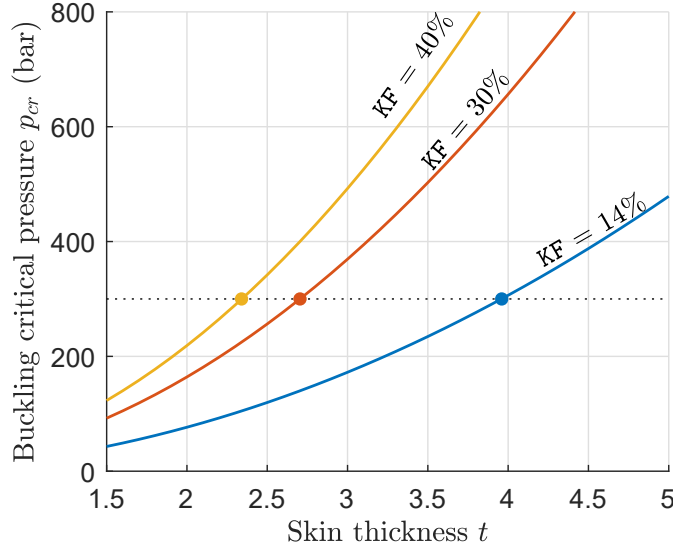
Figure 4.6: Bucking critical pressure against shell thickness, considering a range of KF, from KF=14% to 40%

are aimed at providing new, deterministic approaches to design and analyze the buckling behavior of shells, instead of the traditional methods, based on empirical knockdown factors derived from extensive experimental campaigns.

Precisely manufactured polymeric specimens have recently been used also by Yan et al. [99] to study the structural instability of thin spherical shells with trough-thickness defects, mapping the buckling behaviors as a function of the main geometric parameters of the defect.

A comprehensive investigation on the buckling behavior of metallic hemispheres undergoing external hydrostatic pressure loading is currently being performed by Wagner, Huhne, Zhang et al. [85, 88, 89, 100, 101], including experimental testing, analytical modeling and numerical simulations. A comparison of several analytical models has been given in [85], considering the case of undented and dented hemispheres. Hence, as shown in Fig.4.4, the buckling mode of the hemispheres is strongly affected by the initial imperfection and the geometry of the indenters. Final goal of the research is to provide accurate predictive models and new design criteria.

The effects of multi-layered structures [80], or composite materials [102], as well as the influence of weldings [86] is currently under study, bu recurring to analytical, numerical and experimental activities (Fig.4.3 E, H-I and Fig.4.4N).

4.1.3 Finite Element Analysis

The buckling critical load of a structure can be predicted by using numerical tools as well. The fundamental approach consists in predicting the critical pressure by solving the related eigen-value problem, also known as Linear Bifurcation Analysis. In the case of spherical shells undergoing uniform external pressure, the results are fully in accordance with the analytical predictions made by using Eq.4.4 without considering the knockdown factor. As mentioned before, this may lead to non conservative predictions.

More reliable results can be obtained by switching to more complex tools including non linear analyses, although they require high computational costs, and an increasing level of complexity for the analysis set-up. For instance, Eurocode EN-1993-1-6 [103, 104] suggests to include in the analysis plasticity (material non linearity), large displacements (geometric non linearity), and/or the effects of imperfections, directly measured using non destructive methods, or assumed based on the typical imperfections produced by the specific fabrication technique. Tall et al. [105] described the buckling behavior of perfect and imperfect spherical shells subjected to both external pressure and circumferential shear loadings simultaneously, recurring to both linear and non linear analysis, by including material, geometrical and coupled material and geometrical linearities.

Pan et al. performed a fundamental study of buckling and ultimate strength of spherical pressure hulls, comprehending a critical review [106], a proposal of design formulae based on numerical simulations [107] and experimental testing on titanium shells [81, 100], shown in Fig.4.3 F-G). Experimental buckling tests have been performed on Poly-Metyl-Metachrilate hemispheres for ummanned undewater vehicles by Meschini et al. [82] (Fig.4.3 J) and on Composite Fiber Reinforced Polymer hemispheres by Blachut et al. [102] (Fig.4.3 H-I). Design of metallic and polymeric pressure hulls for manned and unmanned underwater vehicles using analytical methods and `FEA` has also been described by Pranesh et al in [108] and by Khan et al. in [109].

4.2 Isogrid shells

Plain shells revealed to be sensitive to imperfections and prone to fail because of buckling. Hence, it has been decided to investigate shells reinforced by internal stiffening ribs, as previously done for the study case of the Europa meltprobe concept. The axi-symmetry of the spherical shape and of the loading conditions, being uniform hydrostatic external pressure, suggested to use an isogrid layout. Isogrid panels and shells are lightweight structures, composed of a plain or curved skin reinforced by stiffening ribs forming equilateral triangular cells. This particular

57

pattern provides high stiffness and results in a macroscopic isotropic mechanical behavior, from which the name "*isogrid*". Thanks to the high specific stiffness, the isogrid has been extensively used in industry, especially for aerospace applications.

If cylindrical isogrid geometries can be easily obtained from the two dimensional panels, the spherical geometry can be tricky to obtain, due to the double curvature. A convenient approach consists starting from a regular icosahedron, i.e. a polyhedron composed by 20 equilateral triangular faces, whose vertices are located according to Table 4.1. Each triangle represents an isogrid cell, with ribs running along the edges; to obtain a finer pattern, also referred as "*isogrid frequency*" cells are subdivided in smaller triangles, as shown in Fig.4.7.
Finally, the skin and the ribs are projected to the spherical surface bounding the icosahedron. It must be noted that, even if the faces of the original icosahedron were equilateral triangles, the cells obtained by the projection on the sphere are non-regular and different each other.

Table 4.1: Icoshahedron vertices, according to a rectangular reference frame

Icosahedron vertices					
A =	$(0, 1, \varphi)$	E =	$(\varphi, 0, 1)$	I =	$(1, \varphi, 0)$
B =	$(0, -1, \varphi)$	F =	$(\varphi, 0, -1)$	J =	$(-1, \varphi, 0)$
C =	$(0, -1, -\varphi)$	G =	$(-\varphi, 0, -1)$	K =	$(-1, -\varphi, 0)$
D =	$(0, 1, -\varphi)$	H =	$(-\varphi, 0, 1)$	L =	$(1, -\varphi, 0)$
	where $\varphi = (1 + \sqrt{5})/2$ is the golden ratio				
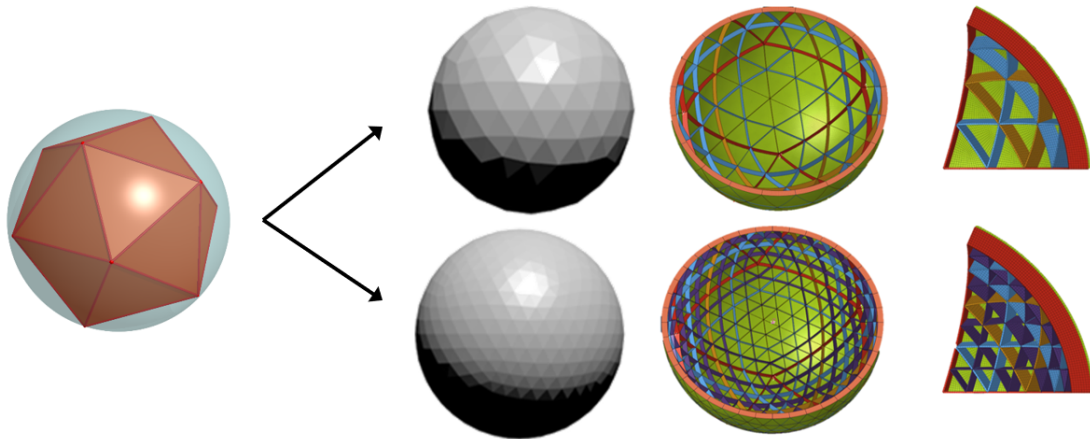
Figure 4.7: Geometry of isogrid spheres for different isogrid frequencies

4.2.1 Basic theory of Isogrid

The isogrid layout is characterized by 4 fundamental dimensions: skin thickness *t*, rib thickness *b*, rib height *d* and triangle height *h*, as shown in Fig.4.8, together with the global $\{x, y\}$ and local $\{P_1, P_2, P_3\}$ reference frames. According to the Isogrid Design Handbook [110], the state of stress of an isogrid panel can be easily described by recurring to some non dimensional parameters:
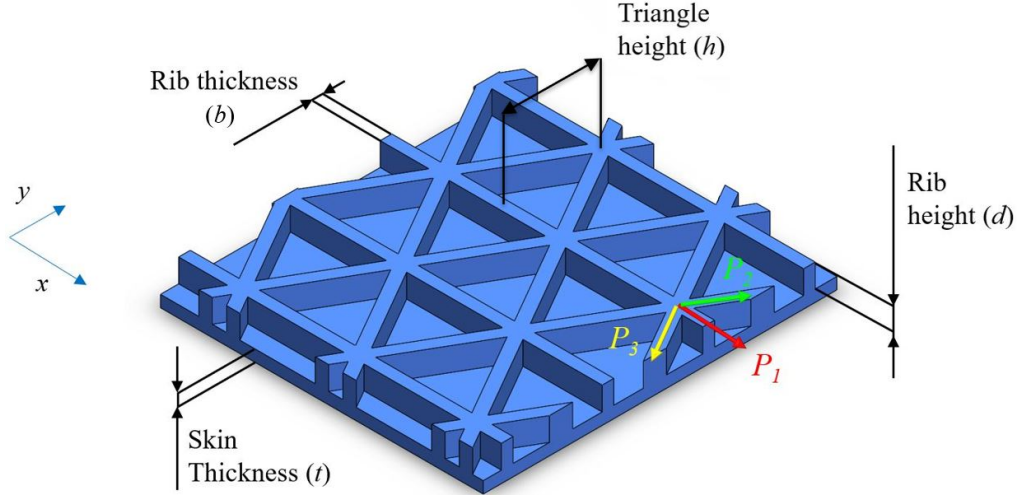
Figure 4.8: Main design variables of the isogrid layout

$$\alpha = \frac{bd}{th} \tag{4.6a}$$

$$\delta = \frac{d}{t} \tag{4.6b}$$

$$\beta = \sqrt{3\alpha(1+\delta)^2 + (1+\alpha)(1+\alpha\delta^2)} \tag{4.6c}$$

so that it is possible to obtain the area (A) and moment of inertia (I) per unit of triangle height, together with the extensional (K) and bending (D) stiffness, as:

$$A = t \cdot (1 + \alpha) \tag{4.7a}$$

$$I = \frac{t^3}{12} \cdot \frac{\beta^2}{1+\alpha} \tag{4.7b}$$

$$\text{K} = \frac{Et}{1-\nu^2} \cdot (1+\alpha) \tag{4.7c}$$

$$\text{D} = \frac{Et^3}{12(1-\nu^2)} \cdot \frac{\beta^2}{1+\alpha} \tag{4.7d}$$

59

Finally, an equivalent monocoque panel can be considered, characterized by thickness t_e and Young's modulus E_e, so that it provides the same extensional and bending stiffness as the isogrid one

$$\begin{cases} \mathtt{K} = \dfrac{E_e t_e}{1 - \nu^2} \\ \mathtt{D} = \dfrac{E_e t_e^3}{12(1 - \nu^2)} \end{cases} \Rightarrow \begin{cases} t_e = t\dfrac{\beta}{1 + \alpha} \\ E_e = E\dfrac{(1 + \alpha)^2}{\beta} \end{cases} \tag{4.8}$$

According to [110], the equations previously reported can be used to calculate the membrane stress of an isogrid shell, so that, given the load per unitary length N, the stress state in the skin and in the ribs can be written as:

$$\begin{cases} \sigma_x = \dfrac{1}{t(1 + \alpha)} N_x \\ \sigma_y = \dfrac{1}{t(1 + \alpha)} N_y \\ \tau_{xy} = \dfrac{1}{t(1 + \alpha)} N_{xy} \end{cases} \tag{4.9}$$

$$\begin{cases} \sigma_1 = \dfrac{1}{3t(1 + \alpha)}(3N_x - N_y) \\ \sigma_2 = \dfrac{2}{3t(1 + \alpha)}(N_y + \sqrt{3}N_{xy}) \\ \sigma_3 = \dfrac{2}{3t(1 + \alpha)}(N_y + \sqrt{3}N_{xy}) \end{cases} \tag{4.10}$$

4.2.2 Analytical modeling

The state of stress and the buckling failure pressure of an isogrid-reinforced spherical shell undergoing uniform external pressure loading can be described by adapting the equation previously described to the specific case, in which:

$$\begin{cases} N_x = N_y = \dfrac{pR}{2} \\ N_{xy} = 0 \end{cases} \tag{4.11}$$

so that Eq.4.9 and Eq.4.10 become:

$$\sigma_{\theta,\phi}^{skin} = \frac{pR}{2t(1 + \alpha)} \tag{4.12a}$$

$$\sigma_1^{rib} = \frac{pR}{3t(1 + \alpha)} \tag{4.12b}$$

60

Due to the complexity of the geometry, three different instability phenomena can occur: the General Instability (`GI`), i.e. the instability of the structure as a whole, the Skin Buckling (`SB`), i.e. the instability of the triangular pockets only, and the Rib Crippling (`RC`), i.e. the instability of the ribs only, as shown in Fig.4.9.
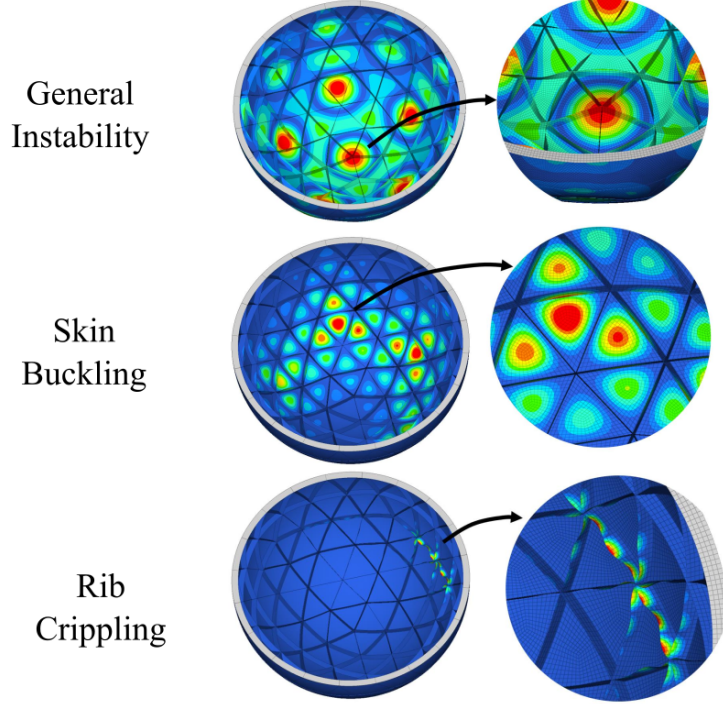
Figure 4.9: `FEA` Post-precessing: examples of different buckling modes. From left to right: `GI`, `SB` and `RC`

The General Instability can be described by modifying the Zoelly's formula (Eq.4.4) with the isogrid equivalent thickness and equivalent Young's modulus:

$$p_{cl} = \frac{2E_e}{\sqrt{3(1-\nu^2)}} \frac{t_e^2}{R^2} = \frac{2E}{\sqrt{3(1-\nu^2)}} \frac{t^2}{R^2} \beta \qquad (4.13)$$

As done for the case of the plain shell, the equation has to be corrected using an empirical knockdown factor, in order to take into account for the detrimental effects of the imperfections. A `KF` of approximately 43% is applied, based on the results reported in the experimental campaign performed on aluminum and plastic domes, described in [111]. The equation can be finally re-written according to the nomenclature used in [110]:

$$p_{\text{GI}} = \frac{\text{KF}}{\sqrt{3(1-\nu^2)}} \cdot 2E \frac{t^2}{R^2} \beta = c_0 \cdot 2E \frac{t^2}{R^2} \beta \qquad (4.14)$$

Reducing the skin thickness, the second type of instability can be observed, involving the shell buckling of the triangular pockets. This can be modeled as a triangular plate loaded in compression with simply supported edges, as shown in Fig.4.10, considering the size of the larger of the isogrid shell and neglecting the curvature ($k_1 = 5$). Therefore, the Skin Buckling pressure can be obtained by equating the triangular plate critical pressure to the skin shell stress:

$$\sigma_{cr}^{triang.plate} = \frac{k_1 \pi^2 E}{12(1 - \nu^2)} \left(\frac{t}{\sqrt{3}/2h} \right)^2 = \frac{p_{\text{SB}} R}{2t(1 + \alpha)} \tag{4.15}$$

Finally, when the ribs get slender, the third type of instability can occur, i.e. Rib Crippling. Similarly to the previous case, the phenomenon can be modeled by considering the case of a rectangular plate loaded as shown in Fig.4.10 ($k_2 = 0.456$):

$$\sigma_{cr}^{rect.plate} = \frac{k_2 \pi^2 E}{12(1 - \nu^2)} \left(\frac{b}{d} \right)^2 = \frac{p_{\text{RC}} R}{3t(1 + \alpha)} \tag{4.16}$$
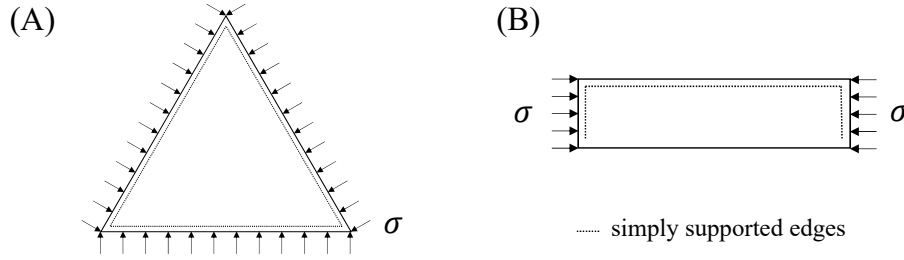
Figure 4.10: Scheme of skin buckling (a) and rib crippling (b) - adapted from [111]

To summarize, the structural instability of isogrid-reinforced external pressure vessels involves three different phenomena, whose failure pressure can be analytically predicted by resorting to Eq.4.14, 4.15, and 4.16, i.e.:

$$p_{\text{GI}} = c_0 \cdot 2E \cdot \frac{t^2}{R^2} \beta \; ; \qquad\qquad c_0 = 0.26 \tag{4.17a}$$

$$p_{\text{SB}} = c_1 \cdot 2E \cdot \frac{t(1 + \alpha)}{R} \frac{t^2}{h^2} \; ; \qquad\qquad c_1 = 3.47 \tag{4.17b}$$

$$p_{\text{RC}} = c_2 \cdot 2E \cdot \frac{t(1 + \alpha)}{R} \frac{b^2}{d^2} \; ; \qquad\qquad c_2 = 0.634 \tag{4.17c}$$

4.2.3   Optimization of the isogrid layout

The isogrid layout shall be finally optimized, in order to find the configuration of minimum mass, given the sphere radius, the material properties, and the eternal pressure as input data. Based on the analytical formulation previously described, a procedure for optimizing the isogrid layout has been developed and it is proposed in this section. At first, structural stability is considered. The non dimensional buckling load factor λ can be defined as the ratio between the buckling critical pressure and the eternal pressure:

$$\lambda = \frac{p_{cr}}{p_{ext}} \tag{4.18}$$

A value of λ per each buckling mode can be obtained. According to [110], the optimal configuration is found when the three critical pressures have the same margin of safety, i.e. the structure collapses because of the three modes simultaneously:

$$\lambda_{\texttt{GI}} = \lambda_{\texttt{SB}} = \lambda_{\texttt{RC}} \Rightarrow optimum \tag{4.19}$$

The isogrid parameters to be defined are the triangle height h, the skin thickness t, the rib thickness b and the rib height d. It must be considered that the isogrid frequency parameter is always a positive integer and, consequently, the triangle height can not vary continuously, being a function of the isogrid density and the sphere radius only. In the proposed design method, the optimization loop does not include h, but its effects are evaluated by running multiple loops. Therefore, the design variables can be reduced to three only, simplifying the optimization process.

First, the `SB` and `RB` critical pressure (Eq.4.17) are equated, so that the rib height d becomes a function of skin thickness and rib thickness:

$$d = \frac{bt}{h}\sqrt{\frac{c_2}{c_1}} \Rightarrow \lambda_{\texttt{SB}} = \lambda_{\texttt{RC}} \tag{4.20}$$

The design variables have been reduced to two only. Then, the `GI` equation is included as well. Given the isogrid frequency and the sphere radius, the failure pressures are mapped as a function of skin and rib thickness, as shown in Fig.4.11 (left), where `SB` and `RC` curved are collapsed in a single one (yellow), because Eq.4.20 is imposed. The intersection between yellow and blue curves represents all the solutions of Eq.4.19; the design point can be found by imposing the minimum buckling critical pressure, according to the design requirements of the specific application.

A clearer representation is given by the top view of the same plot, shown in Fig.4.11 (right), in which the iso-curves of rib height, buckling load factor, and mass are reported.
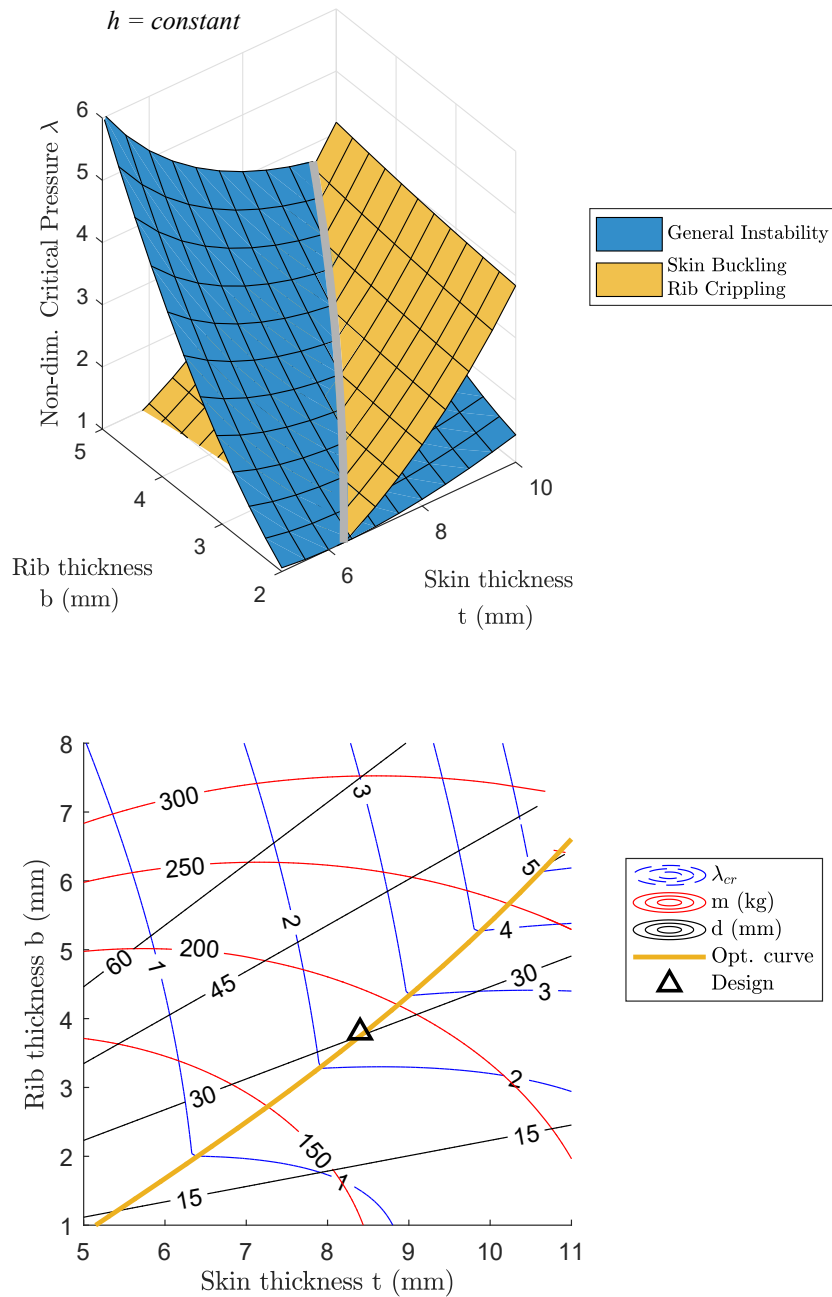
Figure 4.11: Optimum geometry plots: 3D view (top) and top view (bottom)

To verify that the so called optimum curve actually results in a configuration of minimum mass, i.e. to verify Eq.4.19, three sets of analyses have been performed, considering as a test case a $R = 560$ mm sphere made of Ti6Al4V ($E = 110$ GPa) undergoing an external pressure loading of 150 bar, and considering as a requirement a minimum buckling load factor of 2.3.

The methodology previously described has been used to find the optimum isogrid configuration, which results to weigh 183 kg. Then, starting from this point, several isogrid configurations having the same mass have been obtained by fixing one isogrid parameter and varying the other two. The buckling load factors $\lambda_{\texttt{GI}}$, $\lambda_{\texttt{SB}}$, and $\lambda_{\texttt{RC}}$ have been evaluated using Eq.4.17 for every isogrid configuration and results have been plotted in Fig.4.12.
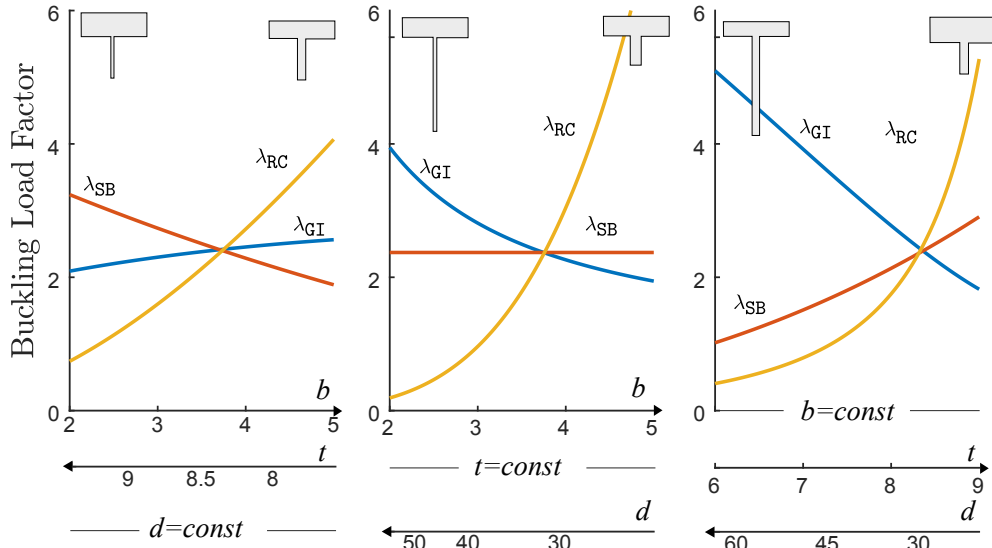
Figure 4.12: Buckling load factor for General Instability (blue), Skin Buckling (red), and Rib Crippling (yellow), as a function of the main isogrid variables

For instance, in the first plot, the rib height is fixed, the rib thickness increases going from left to right, and the skin thickness increases in the opposite direction, so that the mass is kept constant. The configurations on the left side of the plot are characterized by thinner shells, prone to fail because of skin buckling, while configurations on the right have tall ribs and are prone to fail because of rib crippling. The three plots reported in Fig.4.12 show that the solution of Eq.4.17 is a point of optimum, at least locally.

4.2.4 Finite Element Model

The mechanical behavior of isogrid stiffened shells has been modeled by using the Finite Element Method as well. A `FE` model has been created in Altair HyperMesh®, using Altair Optistruct® as solver. A two-dimensional element mesh composed of 4-nodes quadrangular elements (CQUAD4) has been generated starting from one face of the primitive icosahedron; once the ribs were created and the nodes were projected to the bounding spherical surface, the mesh has been replicated to obtain the full geometry.

To limit the computational cost of the analysis, only one hemisphere has been considered (approx. 78000 elements) and symmetric boundary conditions has been applied, as shown in Fig. 4.13. Then, the outer face of the skin elements has been loaded by uniform external pressure and a homogeneous isotropic material model (MAT1) has been used providing Young's modulus and Poisson ratio. Linear static and linear buckling analyses have been performed, to evaluate the stress state and the buckling critical pressure. The most stressed areas, as well the main buckling mode have been evaluated by post-processing the results in Altair HyperView®.
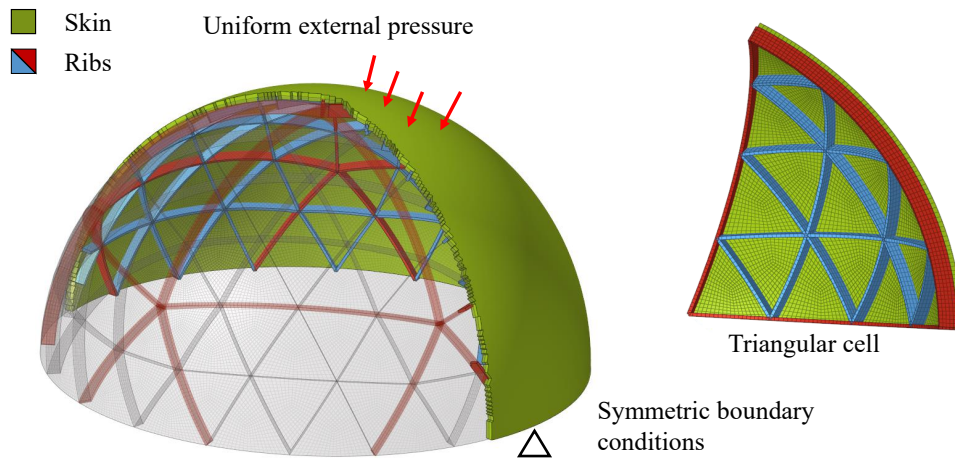
Figure 4.13: Finite Element Model

An array of different geometries has been generated, varying the isogrid parameters, and the results provided by the analytical model and the by the `FEA` have been compared. Three sets of simulations have been performed, for each of which the isogrid frequency and the rib height were fixed, while the skin and rib thickness were varied around a baseline value, as reported in Table 4.2. A total number of 147 isogrid configurations have been generated and analyzed, considering variations of $\pm 50\%$, $\pm 25\%$ and $\pm 12.5\%$ in respect to the baseline values of the skin thickness and the rib thickness.

The displacements and the stresses obtained by the `FEA` have been found in agreement with the analytical predictions. The results of linear buckling analysis are reported in Fig.4.14, in which the results obtained by the analytical model and by the `FEA` are compared. In all the cases, the analytical predictions have been found lower than the `FEA` simulations, being the slope of the regression lines between 0.55 and 0.60. This can be explained by considering that the general instability equation (Eq.4.17) includes an empirical knockdown factor, similarly to what done for plain shells. For this reason, the `FE` linear buckling analysis could lead to non

Table 4.2: Set of trail cases for `FEM` and analytical method comparison

		Set 1	Set 2	Set 3	
Triangle height	h	157	157	79	mm
Rib height	d	30	60	30	mm
Skin thickness (baseline)	t_{base}	8.40	14.70	5.00	mm
Rib thickness (baseline)	b_{base}	3.80	3.10	4.50	mm

Case generation: full factorial, Total number of cases = 3x7x7 = 147
Changes of $\pm 50\%$, $\pm 25\%$ and $\pm 12.5\%$ of the baseline variables
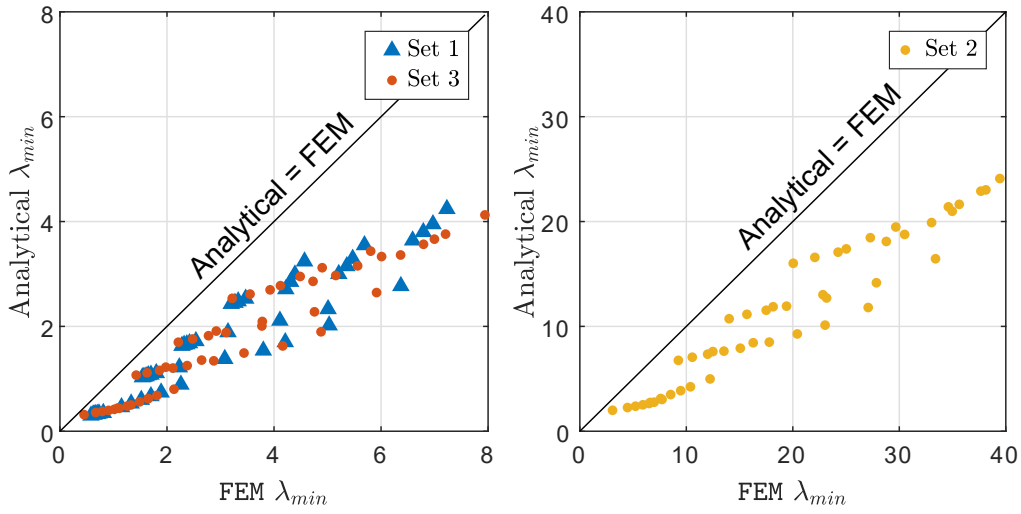
Figure 4.14: `FEM` and analytical method comparison

conservative results and should be corrected by using a knockdown factor as well. The value of the `KF` to be applied to the `FEA` predictions in the design stage should be assessed and validated by experimental testing.

Due to the low computational costs, the development and the validation of linear analytical and numerical methods could provide to designers helpful tools for the preliminary design stage. Non linear simulations, eventually including the effects of geometrical imperfections, could provide more accurate results, but their application is usually limited to the final steps of the design process, due to the high computational costs.

In the next pages, the analytical and numerical approaches described in this chapter will be applied to the case study of a structural shell of a concept for a Venus lander, considering the atmospheric pressure of the planet as the most critical loading condition.

Chapter 5

Venus lander: System design

The design formulae described in the previous chapter have been applied to the case of the concept of a Venus lander described in Chapter 3, whose baseline is a ∅ 1.12 m spherical shell made of Ti6Al4V. This chapter presents the results of the preliminary design of a plain and an isogrid-stiffened primary structure.

Aim of this chapter is describing how the design method previously proposed can be applied to a study case, together with providing estimations of mass and geometry of structure for Pioneer-like landing probes. Limitations of the analytical and numerical methods will be presented, highlighting the need of experimental testing to validate the models.

5.1   Mechanical requirements

The typical mechanical environments of the primary structure of a Venus lander are mainly related to the launch phase, the cruise to Venus, the entry, descent and landing loads, and the environmental conditions of Venus. This preliminary study is focused on the design against the extreme pressure on the surface of Venus (Fig.5.1), which is one of the most critical environments.

According to the concept described in Chapter 3, the primary structure is not pressurized on Earth, i.e. the internal pressure is approximately 1 bar. Therefore, the worst loading condition occurs on the surface of Venus, where the high external pressure may cause shell instability. It must be noted that another strategy [113] consists in internally pressurizing the lander, in order to minimize the differential pressure on the surface of Venus, or make it positive, to avoid buckling failures. In
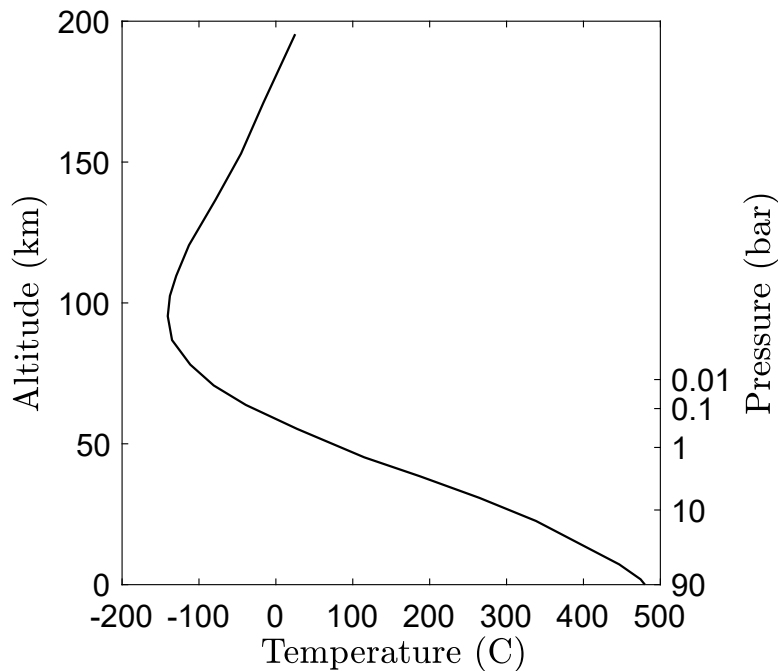
Figure 5.1: Venus environment: temperature and pressure profiles, adapted from [112]

this second case, the most severe conditions occur during the cruise stage, where the net differential pressure is maximum and positive. The present concept does not consider internally pressurized vessels, to facilitate the design and integration of the payload.

Venus surface environment is characterized by high temperature as well, which can affect the mechanical performance of the shell, by involving thermal expansion or degradation of the material properties, such as a reduction of the elastic modulus or the Yield strength (up to 25% at 350 C [114, 115, 116]). It must be noted that the effects of the extreme temperatures of Venus should be mitigated by the active and passive thermal control systems.

In this preliminary stage, the effects of temperature on the structural behavior of the shell have not been taken into account, as the temperature of the shell depends on the thermal control strategy, which relates on the mission architecture, not fully defined. For this reason, the design pressure and the safety factors used for the yielding and buckling analyses have been conservatively set at 100 bar and 1.5, instead of assuming the actual Venus surface pressure and the standard safety

factors [59], somehow providing margins for the degradation of the material properties.

The design method can be easily adapted when details of the thermal environment are fully defined, and lower Safety Factors could applied, performing dedicated tests and assuming an acceptable level of risk.

According to the lander concept, the primary structure would consist of a full solid Ti6Al4V skin with structural functions, together with a porous wick, whose function is mainly related to the thermal system. As the concept of the thermal control system has not fully developed and the morphology of the porous media have not been defined yet, the effects of a wick on the structural performance have not been addressed in this work. Additive Manufacturing is considered as manufacturing technique.

In particular, Laser Powder Bed Fusion (`LPBF`) allows not only the fabrication of complex internal ribbing, but also the co-printing of the full-solid shell and the porous wick together is a single process. It must be noted that the maximum size of `AM` components is limited by the size of the machine, which currently is typically about 250x250x250 mm^3. `AM` machines with larger volumes compatible with the size of the lander concept are under development and may be available in the next years.

Finally, Table 5.2 summarizes the design specification.

Table 5.1: Design specifications

Geometry	Radius	R	560	mm
	Shell thickness, Isogrid layout: To be designed			
Loading Conditions	External pressure	p_{ext}	100	bar
	Yield Safety Factor	SF$_y$	1.5	
Material Properties	Density	ρ	4.4	kg/mm^3
	Young's modulus	E	110	GPa
	Poisson's ratio	ν	0.3	
	Yield's strenght	σ_y	910	MPa
Requirements	No yield at the design pressure			
	No buckling at the design pressure. KF =?			

5.2 Plain sphere

Firstly, the plain geometry has been considered.
Considering Zoelly's equation (`KF` = 1), or equivalently the Linear buckling `FEA`, the buckling load factor can be calculated as follow:

$$\lambda = \frac{p_{cl}}{\text{SF}p_{ext}} = \frac{p_{\text{LFEA}}}{\text{SF}p_{ext}} \tag{5.1}$$

The buckling load factor can be plotted against the shell thickness t, as reported in Figure 5.2. The secondary axis reports also the Margin of Safety (`MoS`) obtained from the linear static analysis as follow:

$$\text{MoS} = \frac{\sigma_y}{\text{SF} \cdot p_{ext}} - 1 \tag{5.2}$$

where σ_y is the Yield strength of the material.
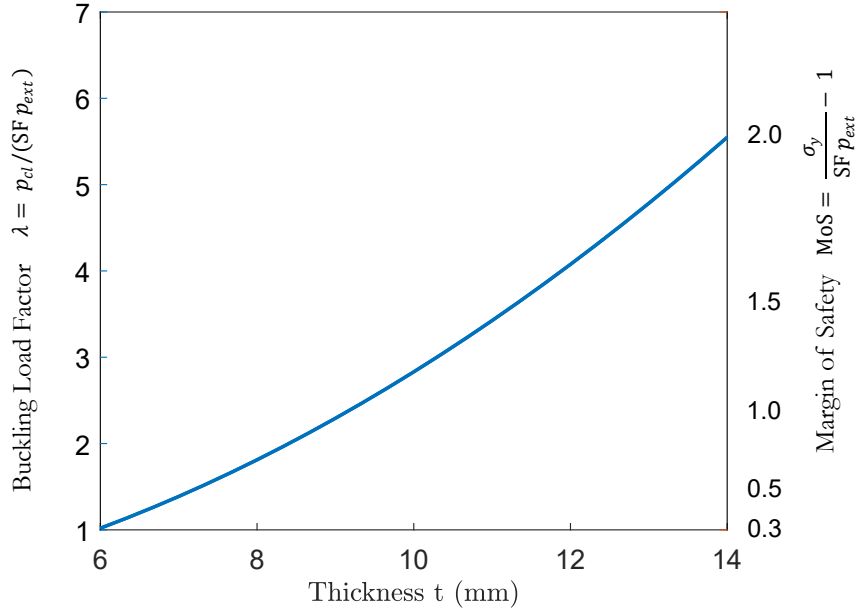
Figure 5.2: Buckling Load Factor and Yield Margin of Safety for a range of shell thicknesses

By increasing the shell thickness t, both the static and the buckling resistance are improved, resulting in higher margin of safety and buckling load factor. The design point has been chosen so that it provides a positive `MoS` and a buckling load factor equal to 3.2 approximately. It must be noted that the `KF`-based formulation can be considered as well:

$$p_{cr} = \text{KF} \cdot p_{cl} \tag{5.3}$$

where p_{cl} is the buckling critical pressure obtained by Zoelly's equation, or by linear `FEA`, and the critical pressure must be set at the external pressure, multiplied by the safety factor, so that:

$$\text{KF} = \frac{p_{cr}}{p_{cl}} = \frac{\text{KF} \cdot p_{ext}}{p_{cl}} = \frac{1}{\lambda} \tag{5.4}$$

In this way, imposing a buckling load factor of 3.2 is equivalent to using Zoelly's equation, modified by a `KF` of approximately 30%, as suggested by the industrial practice [62].

Table 5.2: Plain shell configuration

Geometry	Radius	R	560	mm
	Shell thickness	t	10.5	mm
textbfMass	Spherical shell mass	m	184	kg
Linear	Buckling Load Factor	λ	3.2	
Analyis	Yield Margin of Safety	MoS	1.3	

5.3   Isogrid sphere

In this section, the procedure and the results of the preliminary design of the isogrid shell will be presented. Firstly, the analytical method presented in the previous chapter has been used to find the optimum geometry for two different isogrid frequencies (h=157mm and h=79mm), named *Baseline* and *Finer* respectively. As done for the case of the plain shell, the geometry has been defined so that a positive `MoS` can be achieved, and the buckling load factor calculated by `FEA` (λ_{FEA}) was equal or greater than 3.2, or, considering the analytical method, $\lambda_{\text{FEA}} \geq 2.4$.

As an example, Fig.5.3 reports the optimization plot for this *Baseline* case, obtained using the procedure presented in the previous chapter. The triangular marker identifies the selected configuration. The configurations *Baseline* and *Finer* are compared in Fig.5.4, in which the cross sections of an isogrid cell are shown. By passing from the *Baseline* layout to the *Finer* layout, a significant reduction of the shell thickness can be observed, while the ribs are subjected to small variations.

The mechanical behavior of the two layouts has also been checked by numerical simulations. Two `FEM` models have been created and linear static and linear buckling analysis have been performed. Contour plots of displacements, stress and buckling modes are shown in Fig.5.5, and results are finally summarized in Table 5.2.
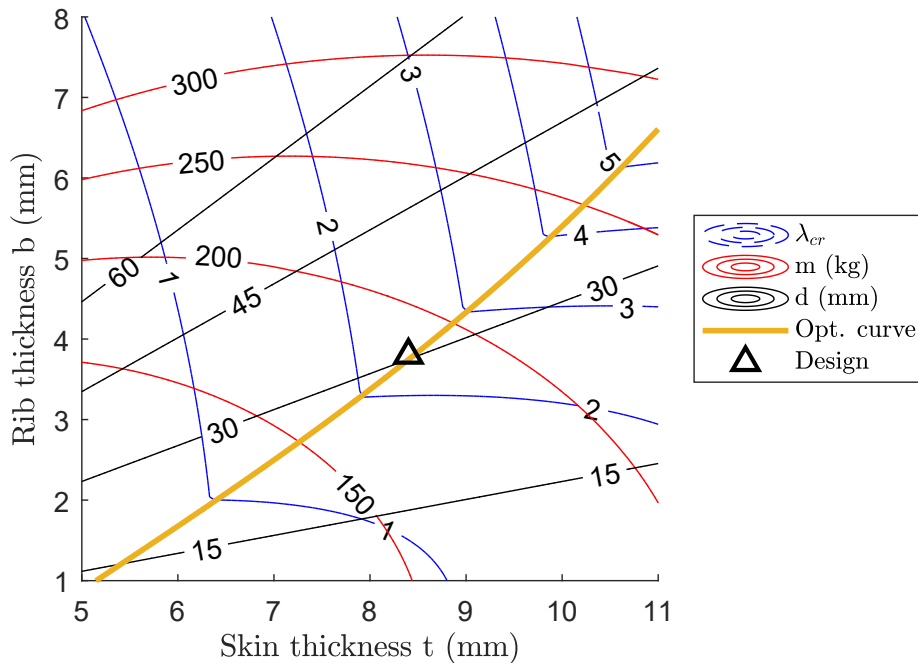
Figure 5.3: Optimization plot based on the analytical method described in the previous chapter
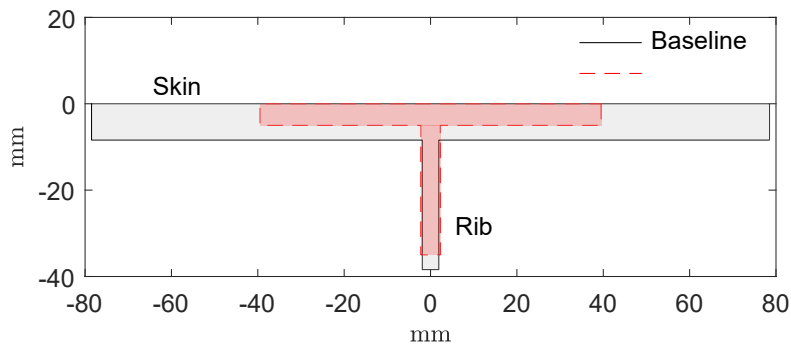
Figure 5.4: Isogrid cross-section for *Baseline* and *Finer* model

Comparing the analytical results to the `FEA` simulations, a large difference in buckling performance can be noted: in fact, for both *Baseline* and *Finer* models, the analytical minimum buckling load factor is significantly lower than the `FEM` one. As discussed in the previous chapter, this difference was expected, because of the empirical parameter c_0 included in the analytical formulation, but not in the `FEA` simulations.

Comparing the two isogrid configurations, it can be observed that, as the isogrid

frequency increases, the skin thickness decreases, the maximum Von Mises stress increases, while the mass is almost the same. For this reason, the geometry with larger triangles (*Baseline*) will be considered in the following activities.

Finally, the size optimization tool present in Altair Optistruct has been used to optimize the geometry, considering as design variables the skin thickness and the rib thickness and defining the minimization of the mass as the optimization objective, setting a minimum buckling load factor of 3.2. Starting from the configuration *Baseline* and making *t* varying from 3 to 15 mm and *b* from 1 to mm, the optimization algorithm iteratively ran the `FEA`, updating the design variables according to the gradient method.

As shown in Table 5.2, the optimization resulted in a slightly thicker skin (+2.3%), and thinner ribs (+27.9%). No significant mass reduction has been observed (-3.3%) and Linear Static performance (equivalent Von Mises stress and displacements at the design pressure) were almost unchanged. Even if $\lambda_{\texttt{FEA}}$ was still 3.2, the buckling critical factor obtained using the analytical formulation (λ_{cl}) dropped down from 2.43 ti 1.30, due to a lower value of rib crippling critical pressure. For this reason, the *Baseline* layout has been considered as the baseline configuration for the following activities.

Table 5.3: *Baseline*, *Finer* and Size Opt. configurations

			Baseline	*Finer*	Size opt.	
Geometry	n div		2	3	2	
	Triangle height	h	157	79	157	mm
	Skin thickness	t	8.4	5	8.6	mm
	Rib height	d	30	30	30	mm
	Rib thickness	b	3.8	4.5	2.74	mm
	Mass	m	184	179	178	kg
Analytical Model	Max. displacement	u	1.53	2.08	1.53	mm
	Max Von Mises stress	σ	460	625	461	mm
	Buckling load factor	λ_{cl}	2.43	2.54	1.30	mm
`FEA`	Max. displacement	u	1.61	2.31	1.61	mm
	Max. Von Mises stress	σ	496	695	487	MPa
	Buckling load factor	$\lambda_{\texttt{FEA}}$	3.20	3.22	3.20	
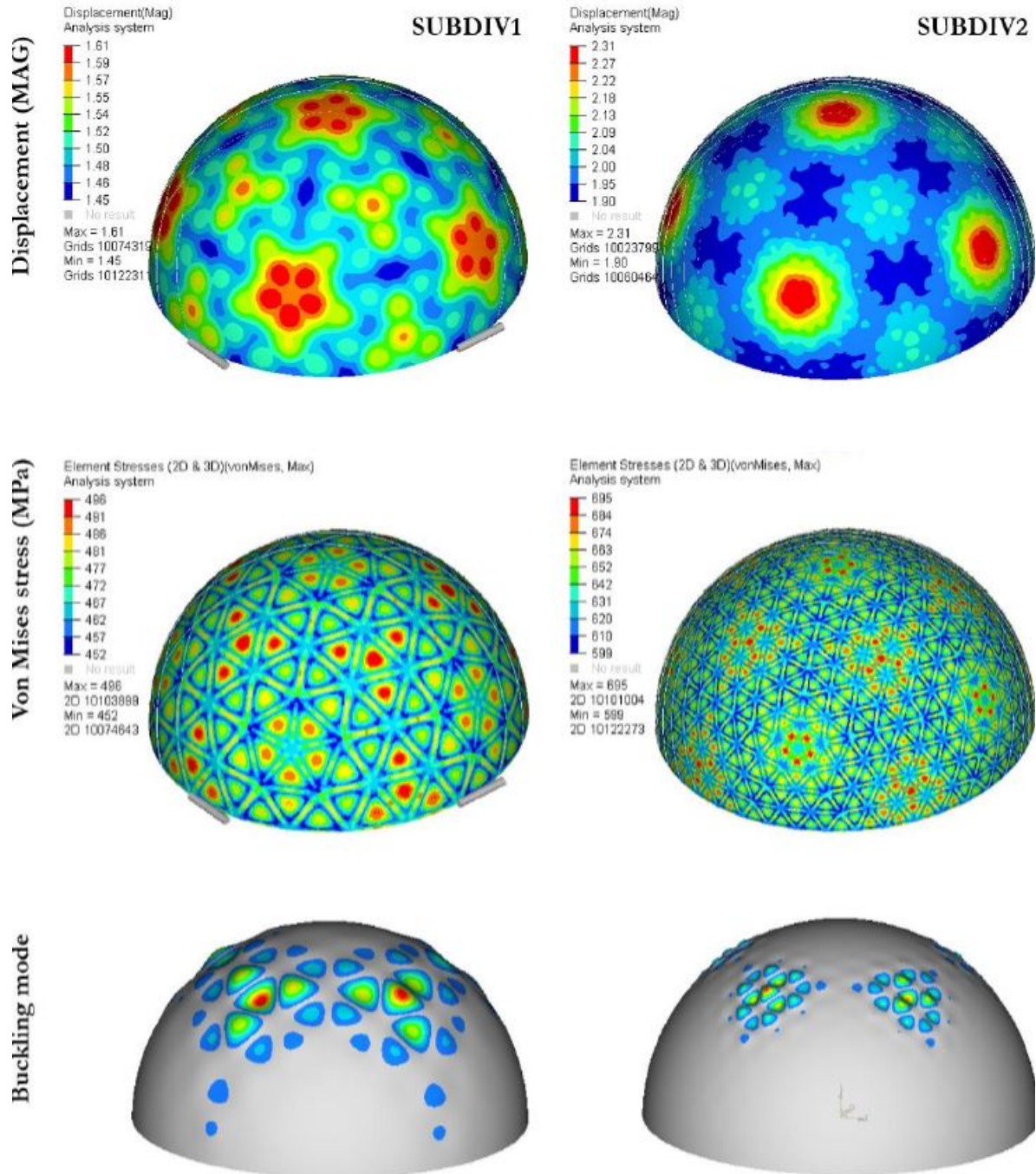
Figure 5.5: Results of the linear `FEA`: contour maps of displacements (mm), Von Mises stresses (MPa) and buckling shape for the Baseline (left) and Finer (right) models

5.4   Conclusion

The analytical methods described in the previous chapter have been applied to the study case of a concept of a Pioneer-like Venus lander, considering both plain and isogrid-stiffened configurations.

Given the structural requirements, being a minimum buckling load factor of 3.2 and a positive margin of safety in respect to yielding, the plain and the isogrid layouts have been sized. Surprisingly, no mass savings have apparently been achieved by passing from the plain to the isogrid layout. However, it must be noted that the required minimum buckling load factor (or, equivalently, the knockdown factor) may significantly vary from plain to stiffened shell, potentially resulting in mass savings. In fact, the internal isogrid ribbing may improve the buckling resistance and make the component less sensitive to geometric imperfections, which typically trigger the premature instability of spherical shells. This could allow to use lower `KF` values for the isogrid case, resulting in mass savings.

For this reason, and to assess the suitability of `AM` processes for external pressure vessels, an experimental campaign on sub-scale components has been conducted, as it will be discussed in the next chapter.

Chapter 6

Model validation and Design Synthesis

In the previous chapter, the analytical design techniques were applied to the study case of a concept for a Venus lander. One of the most critical limitations consisted in the uncertainties in the accuracy of the predictive models, which include empirical knockdown factors derived form past experimental works [110, 111]. Moreover, the mechanical behavior of spherical external pressure vessels is strongly affected by the presence of geometric imperfections, which depends also on the manufacturing process. In this frame, testing activities were needed to both explore the capabilities of Additive Manufacturing in fabricating thin spherical shells, and to investigate the buckling behavior of isogrid-stiffened shells.

This chapter reports the experimental activities performed on Ti6Al4V sub-scale components, composed of the following tasks:

- design of the plain and the isogrid sub-scale components, by recurring to the analytical methods previously described and updating the geometry to meet the manufacturing requirements;

- manufacturing of the test articles, including the fabrication by `L-PBF` in Ti6Al4V, the post-processing, and the machining the interfaces;

- experimental testing, subdivided in a) hydrostatic test, performed by imposing an increasing uniform pressure acting on the external surface of the test articles, up to failure; b) relative environment test, performed at high pressure and temperature to simulate the atmospheric conditions of Venus.

The results of this experimental activities will be used to update the geometry of the full scale model during the final design synthesis.

6.1 Sub-scale modeling

The dimensions of the concept described in the previous pages have been based on a Pioneer-like probe, having a shell diameter of approximately ∅ 1 m. However, most of the L-PBF machines currently available are characterized by a working volume of about 250 x 250 x 250 mm^3, which does not allow the fabrication of so large components. Hence, it has been decided to consider a sub-scale geometry, with a shell diameter of ∅ 200 mm.

6.1.1 Isogrid design

The analytical design procedure previously used for sizing the full scale model has been applied to the sub-scale version, and the optimization plot of Fig. 6.1 has been obtained, in which the optimum configurations curve (in yellow) has been plotted as a function of the main geometric parameters, together with the iso-curves of the predicted failure pressures.
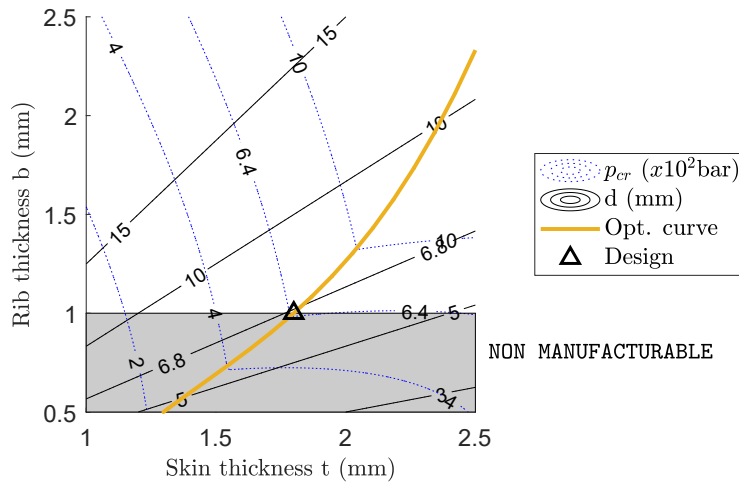
Figure 6.1: Scaled model - isogrid optimum geometry

Moreover, it was necessary to restrict the design space, in order to consider the typical manufacturing limitations: for instance, ribs thinner than 1 mm may be affected by distortions or critical internal defects generated during the fabrication process. Hence, a gray area has been added on Fig. 6.1, representing the non-manufacturable geometries. The design point, obtained by imposing the manufacturing limits instead of the failure pressure, has been indicated by the triangular marker; according to the analytical model, it resulted in an expected failure pressure of 640 bar.

`FEA` has been performed as well, by using the model described in Chapter 4, updated according to new geometric parameters. The buckling failure pressure has been estimated to be 810 bar, according to the `FE` linear buckling analysis. As a reference, linear static analysis has been performed as well, considering an external pressure of 100 bar; the maximum Von Mises stress and displacement have been estimated as 269 MPa and 0.16 mm respectively. A summary of the baseline of the isogrid sub-scale component is reported in Table 6.1.

Table 6.1: Scaled model design - summary

Geometry	Radius	R	100	mm
	Triangle size	h	28	mm
	Skin thickness	t	1.8	mm
	Rib height	d	6.8	mm
	Rib thickness	b	1	mm
Mass	Hemisphere	m	0.690	kg
Linear Analysis	Analytical buckling pressure	p_{analyt}	640	bar
	LFEA buckling pressure	$p_{\mathbf{LFEA}}$	810	bar
	LFEA max stress at p = 100 bar	$\sigma_{\mathbf{LFEA}}^{100bar}$	269	MPa
	LFEA max displac. at p = 100 bar	$u_{\mathbf{LFEA}}^{100bar}$	0.16	mm

Finally, manufacturing issues have been addressed, in order to improve the manufacturability. Two different fabrication directions are possible, as reported in Fig.6.2. However, support structures in the internal surface can be difficult to remove and could results in high surface roughness and irregularities. For this reason, layout b has been selected. Small modifications in the geometry, such as fillets and chamfers, have been made (Fig.6.3), in order to reduce the overhangs and to avoid stress concentrations at the intersections between ribs.
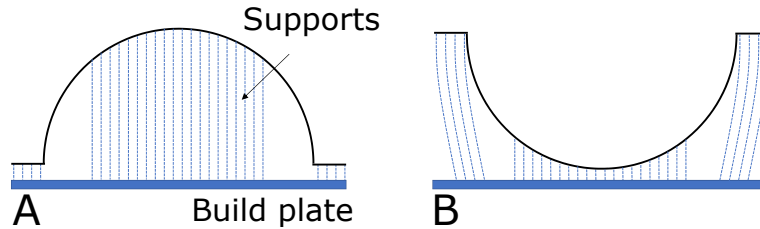
Figure 6.2: Possible fabrication layouts
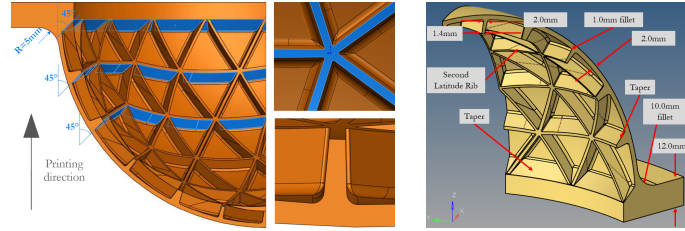
Figure 6.3: Detail of fillets and chamfers added to improve the manufacturability

As the new geometry is slightly different from the ideal isogrid layout, a new `FEA` has been performed (Table 6.2), showing an improvement in the buckling resistance, as well as lower stress peaks. A more detailed analysis, including non-linear simulations, will be presented in the Section 6.3.2.

Table 6.2: Ideal vs modified isogrid

			Ideal	Modified	
Mass	Hemisphere	m	0.690	0.833	kg
	Hemisphere with flange	m'		1.562	kg
Linear Analysis	Analytical buckling pressure	p_{analyt}	640	NA	bar
	LFEA buckling pressure	p_{LFEA}	810	934	bar
	LFEA max stress at p = 100 bar	$\sigma_{\text{LFEA}}^{100bar}$	269	251	MPa

6.1.2 Plain shell

A plain sub-scale shell has been designed as well by recurring to the analytical methods described in the previous chapters. A summary of the properties of the plain shell are given in Table 6.3. Similarly to the isogrid case, supports have been designed to improve the manufacturability, and support structures have been added near the overhangs.

Table 6.3: Scaled model design - summary

Geometry	Radius	R	100	mm
	Skin thickness	t	2.7	mm
Mass	Hemisphere	m	0.731	kg
	Hemisphere with flange	m'	1.460	kg
Linear Analysis	Analytical buckling pressure (Zoelly)	p_{cl}	971	bar
	LFEA buckling pressure	p_{LFEA}	971	bar
	LFEA max stress at p = 100 bar	$\sigma_{\text{LFEA}}^{100bar}$	185	MPa

6.2 Manufacturing

A total of 7 isogrid hemispheres and 1 plain hemisphere have been fabricated in Ti6Al4V alloy using `L-PBF` technique. After the fabrication, the components have been subjected to `HIP` treatment and then removed from the building platform and machined. A Computerized Numerical Control machine has been used to remove the support structures and to machine the interfaces, to obtain planar surfaces and the holes for the fasteners, as shown in Fig.6.4. Visual inspection has been performed on the final components. A few cm long, about 0.1 mm high protruding flow (Fig.6.5) has been detected on the external surface of the shells. It could have been related to some warping, or distortions during the manufacturing process.
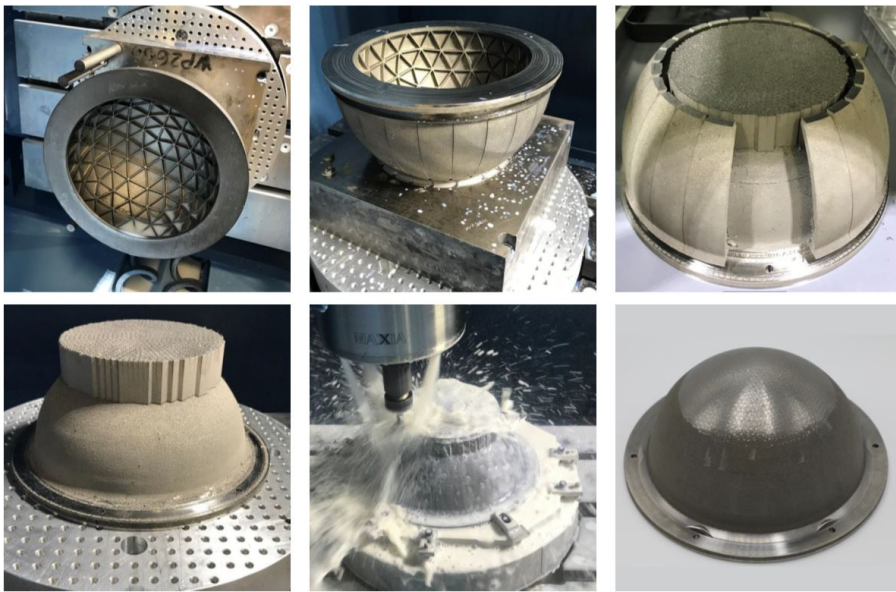
Figure 6.4: Support removing and machining
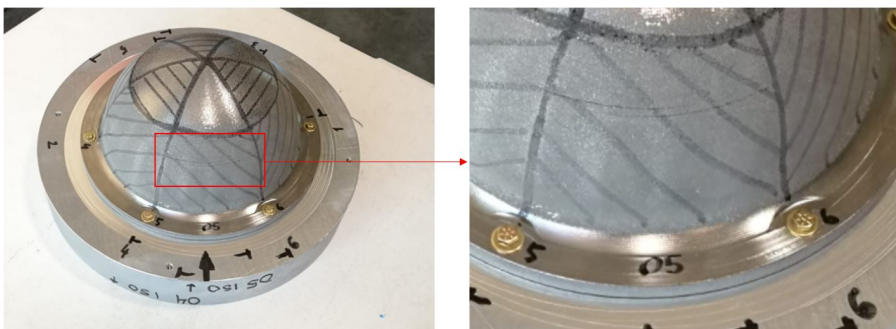
Figure 6.5: Manufacturing flaw on the external surface of the hemisphere

6.3 Hydrostatic test

Firstly, ambient temperature hydrostatic test has been performed. Aim of the test is investigating the failure pressure and the failure mode of both the plain and isogrid shells, to validate the models used in the design stage.

6.3.1 Test procedure

Four articles (3 isogrid and 1 plain hemispheres) have been tested, one per each run. Each test article was filled with plastic beads to reduce the shock wave at failure, and sealed to a thick aluminum plate, using a rubber o-ring and 6 fasteners. The test have been conducted in a hydrostatic pressure chamber, increasing the pressure acting on the external surface of the shell by pumping water inside the chamber, according to Fig.6.6, until the failure of the test article. An analogical pressure gage has been used to monitor and manually record the pressure inside the chamber. In addition, a high pressure rated video camera has been set up, in order to monitor the specimen during testing. Failure can be detected by a sudden pressure drop measured by the pressure gage of the chamber, and camera images.
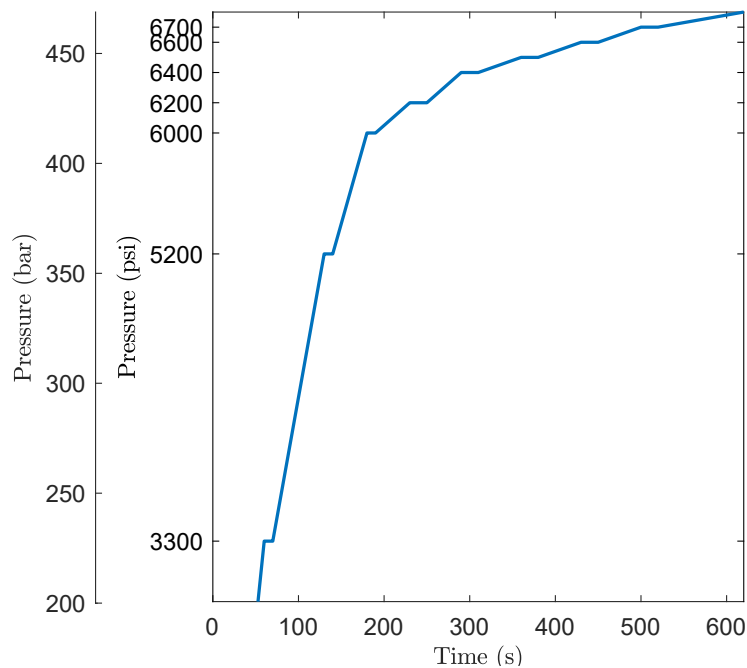
Figure 6.6: External pressure vs time (for convenience, the plot is cut for value below 200 bar). To better detect the failure point, the pressure rate decrease step by step; in addition, at each step, a dwell time is applied.

Figure 6.7: Hydrostatic test: test article preparation

6.3.2   Predictions

Linear and Non linear analysis have been performed, for both the plain and isogrid geometry, to predict the failure pressure. The linear analysis has been performed using shell element model, described in Section 4.2. Non linear analyses have been performed in Radioss®, considering both material and geometric non linearities and applying the pressure load as a linear function of time. Two models were created, considering a two-dimensional element mesh (the same as the linear analysis) or a three-dimensional tetrahedral element mesh, to better replicate the geometry of chamfers and junctions between the ribs. In the second case, only 1/5 of the hemisphere was modeled, to reduce the computational cost.

The contour plots of the 2D and 3D element models are reported in Fig.6.8, for the isogrid and the plain geometry. The results of the simulations are summarized in Table 6.4.

Comparing the two dimensional element non linear model and the tetra element

85

non linear model, similar results have been obtained in the case of the plain shell, while some discrepancies have been noted for the isogrid geometry. This could be related to the adoption of the hypothesis of the symmetric boundary conditions. For the following activities, the results obtained by the linear analysis and the non linear analysis using 2D elements will be considered.

Comparing the results of linear and non linear `FEA`, the first predicted higher failure pressures when considering a buckling knockdown factor of 1. When a `KF` of 30 % is applied, accordingly to what suggested by industrial practice [62], the results of the linear simulations are more conservative than the non linear predictions. The results of the experimental activities will help in assessing the most appropriate value of the knockdown factor, to be applied in the design stage, together with the accuracy of the non linear predictions.

Table 6.4: Predictions - Hydrostatic test

			Plain	**Isogrid**	
Mass	Hemisphere w/o flange	m	0.731	0.833	kg
Linear	LFEA buckling pressure	p_{LFEA}	971	934	bar
Analysis	KF suggested by [62]	$30\% p_{\mathrm{LFEA}}$	291	280	bar
	Max stress at p=100 bar	$\sigma_{\mathrm{LFEA}}^{100bar}$	185	251	MPa
Non Linear	NLFEA buckling pressure	$p_{\mathrm{NL,2D}}$	507	448	bar
Analysis (2D)	Max stress at $p = p_{\mathrm{NL,2D}}$	$\sigma_{\mathrm{NL,3D}}^{p}$	1154	1038	MPa
Non Linear	NLFEA buckling pressure	$p_{\mathrm{NL,3D}}$	510	523	bar
Analysis (3D)	Max stress at $p = p_{\mathrm{NL,3D}}$	$\sigma_{\mathrm{NL,3D}}^{p}$	1190	1245	MPa
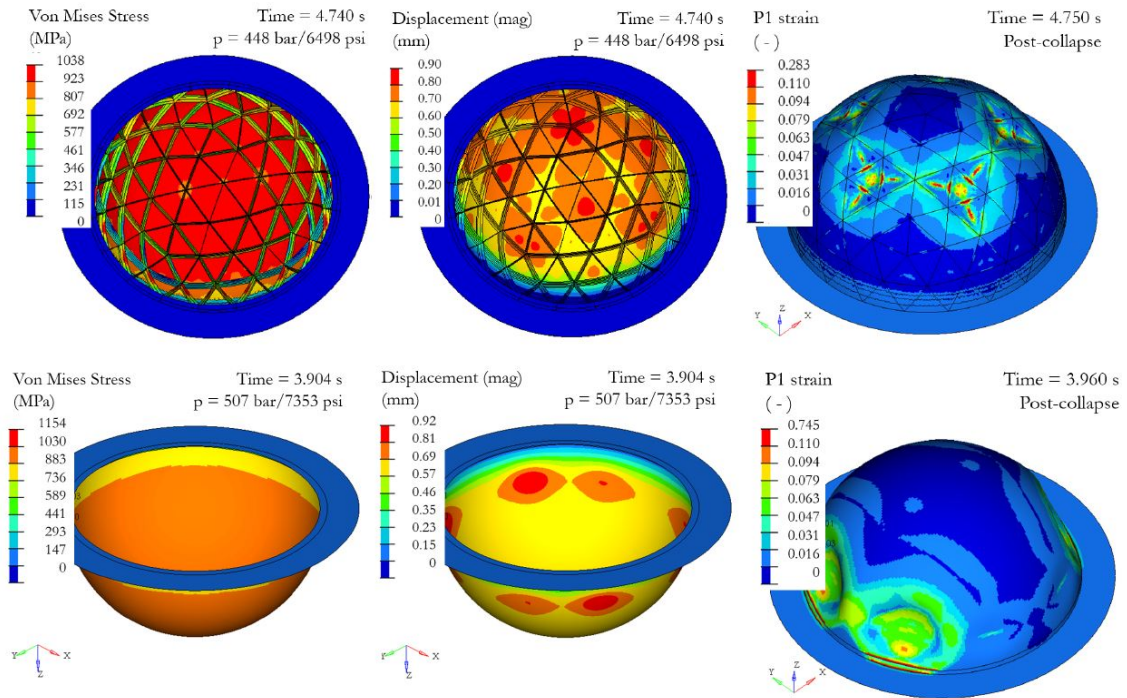
(a) 2D element model
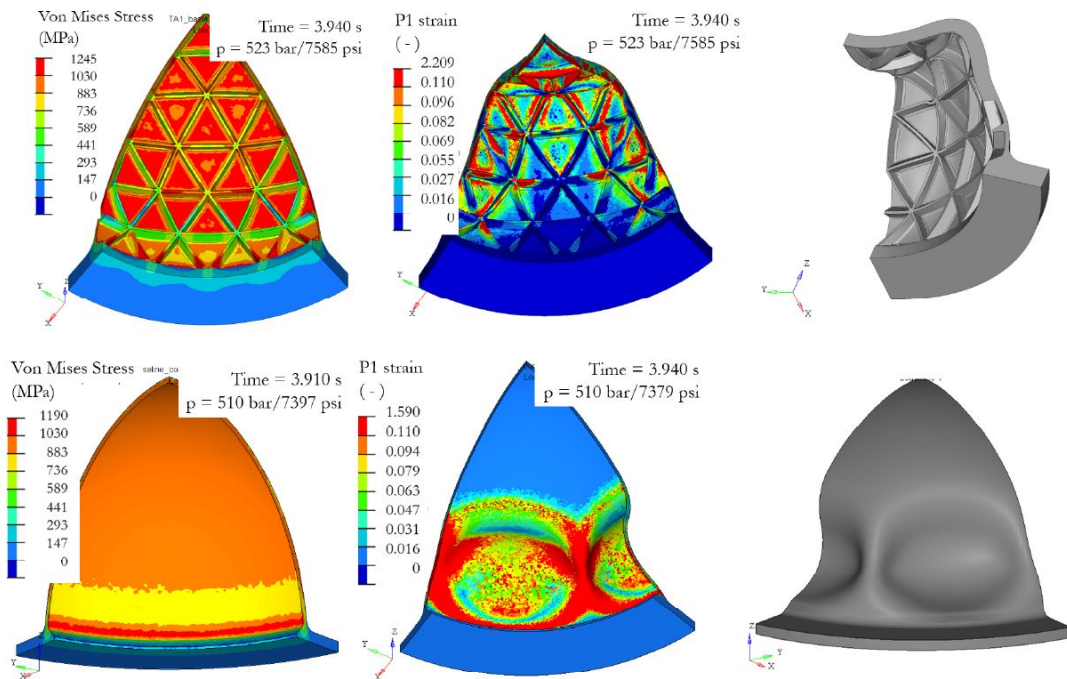
(b) 3D element FE model

Figure 6.8: Ambient temperature hydrostatic test: Non Linear FEA

6.3.3 Results and discussion

The tests were performed at the DeepSea Power & Light facility in San Diego, CA. Some pictures of the test set up are reported in Fig.6.9 and [**fig:2.hydro_test2**].
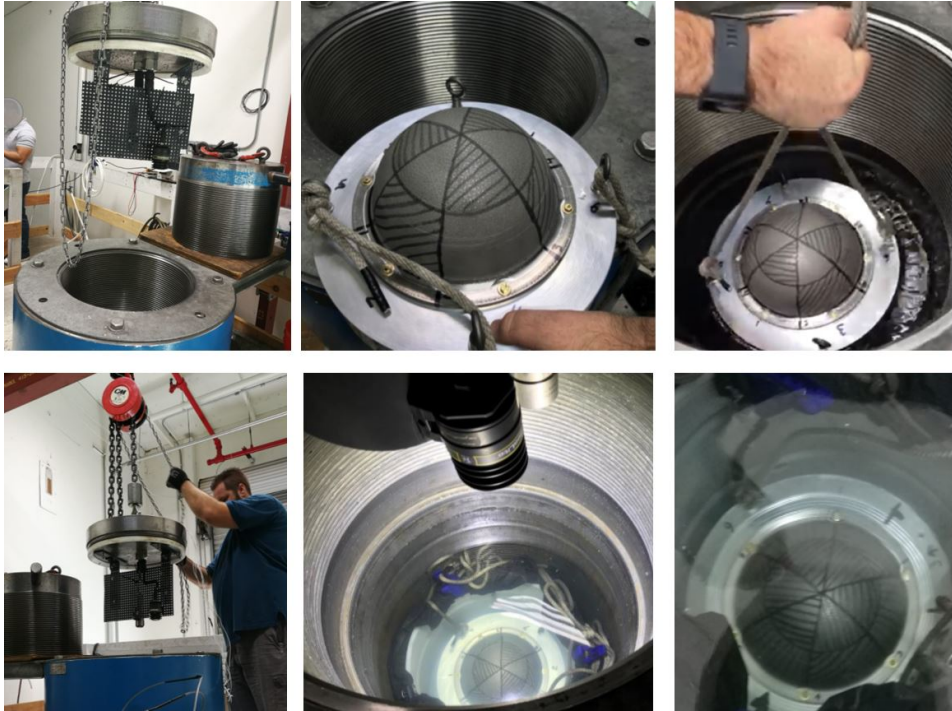
Figure 6.9: Hydrostatic test: test preparation
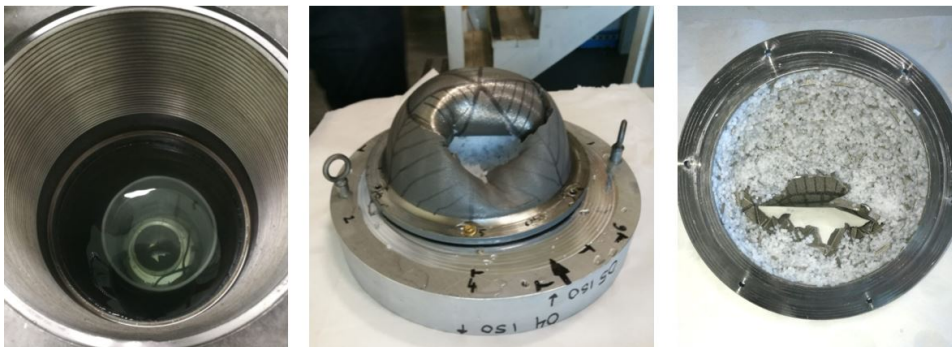
Figure 6.10: Hydrostatic test: test article after testing

The plain shell (SN00) suddenly collapsed at 317 bar. The failure started from the manufacturing imperfection (as visible in Fig.6.11 - first row). The three isogrid hemispheres (SN01, SN04, SN05) failed at 410.3 ± 4.0 bar (414, 411, 406 bar).

Similarly to the plain shell, the failure consisted in a sudden and violent implosion of the shell (Fig.6.11 - second row), starting near the most critical manufacturing imperfection and propagating in the upper part.
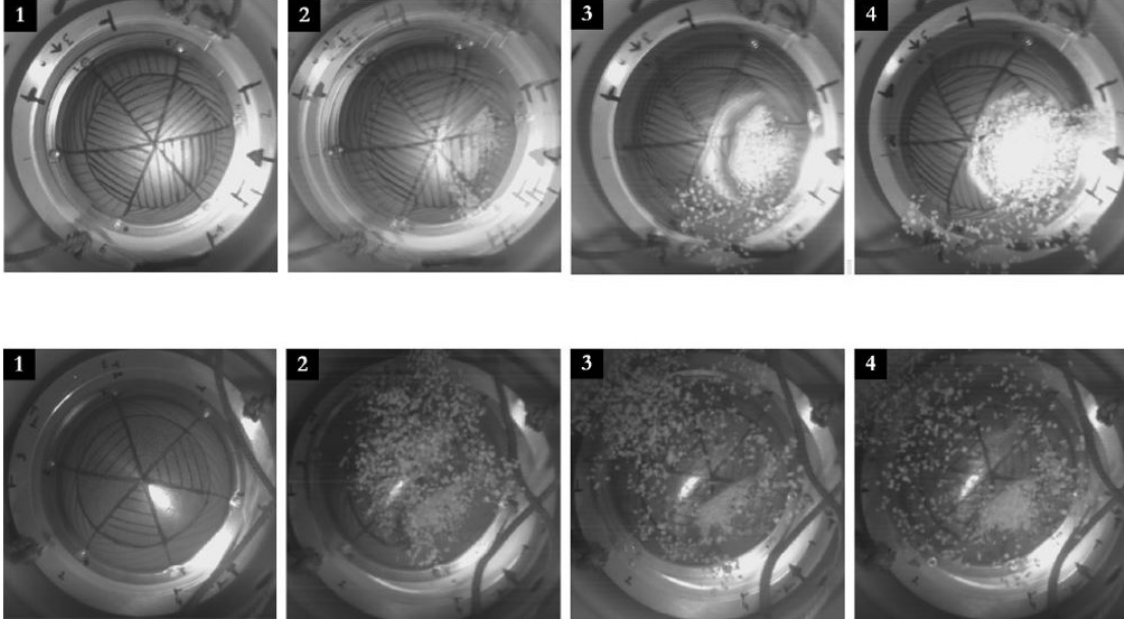
Figure 6.11: Hydrostatic test: frames from the video recording for the plain shell (first row) and one od the isogrid shell (second row)

Table 6.5 compares the experimental failure pressure to the predictions made by the linear and non linear analysis, reporting the KF and *err* value, calculated as follow:

$$\texttt{KF} = \frac{p_{exp}}{p_{\texttt{LFEA}}} \tag{6.1a}$$

$$\texttt{err} = \frac{p_{\texttt{NL, 2D}} - p_{exp}}{p_{exp}} \tag{6.1b}$$

It is possible to observe that:

- the failure mode of the isogrid shells is very repeatable and the failure pressure are consistent over the test articles,

- the KF of the plain sphere (33%) is accordance to the values suggested by Roark's [62] (30%) for traditionally manufactured shells,

- the KF of the isogrid sphere is higher than the plain one, being 44%,

89

Table 6.5: Comparison between experimental results and predictions

			Plain	Isogrid	
Mass	Hemisphere w/o flange	m	0.731	0.833	kg
Experimental	Failure pressure	p_{exp}	317	410	bar
Linear Analysis	LFEA buckling pressure	p_{LFEA}	971	934	bar
	LFEA Knocdown factor	KF	33%	44%	
Non Linear Analysis	NLFEA buckling pressure	$p_{\mathrm{NL,\ 2D}}$	507	448	bar
	Error	err	60%	9%	

- the non linear predictions overestimated the failure pressure of the plain shell by 60%,

- the mismatch of non linear predictions in respect to the experimental result as low as 9% in the case of the isogrid shells.

Linear predictions overestimated the failure pressure in both the cases. This could be related to the presence of the imperfection, which may act as a trigger for buckling instability. The higher discrepancies found for the plain shell may be suggest that the isogrid stiffening made the shell less sensitive to imperfections.

Furthermore, the videos recorded by the camera inside the chamber have been analyzed. Prior to the collapse, both plain and isogrid shells seemed to exhibit local buckling in the region near the manufacturing imperfections. However, it must also be noticed that the global failure mode was not clearly identified as buckling or yielding, being the latter a potential option, because of the high stresses predicted by analysis.
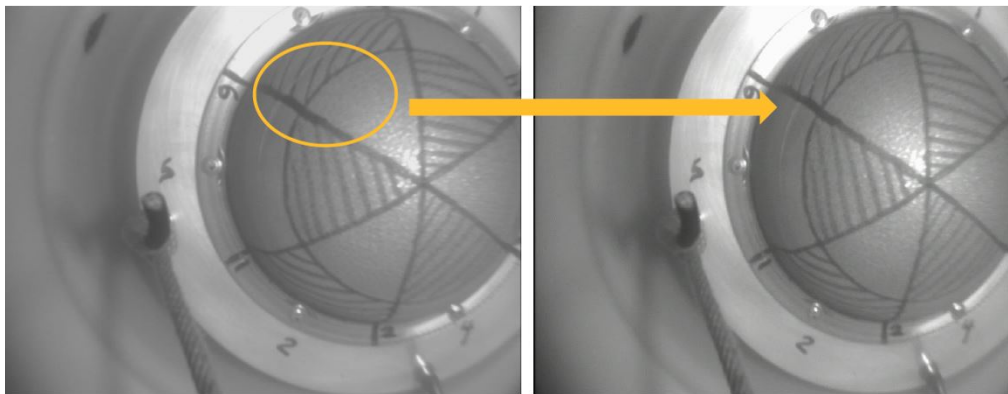
Figure 6.12: Hydrostatic test: detail of the manufacturing flaw just prior to collapse
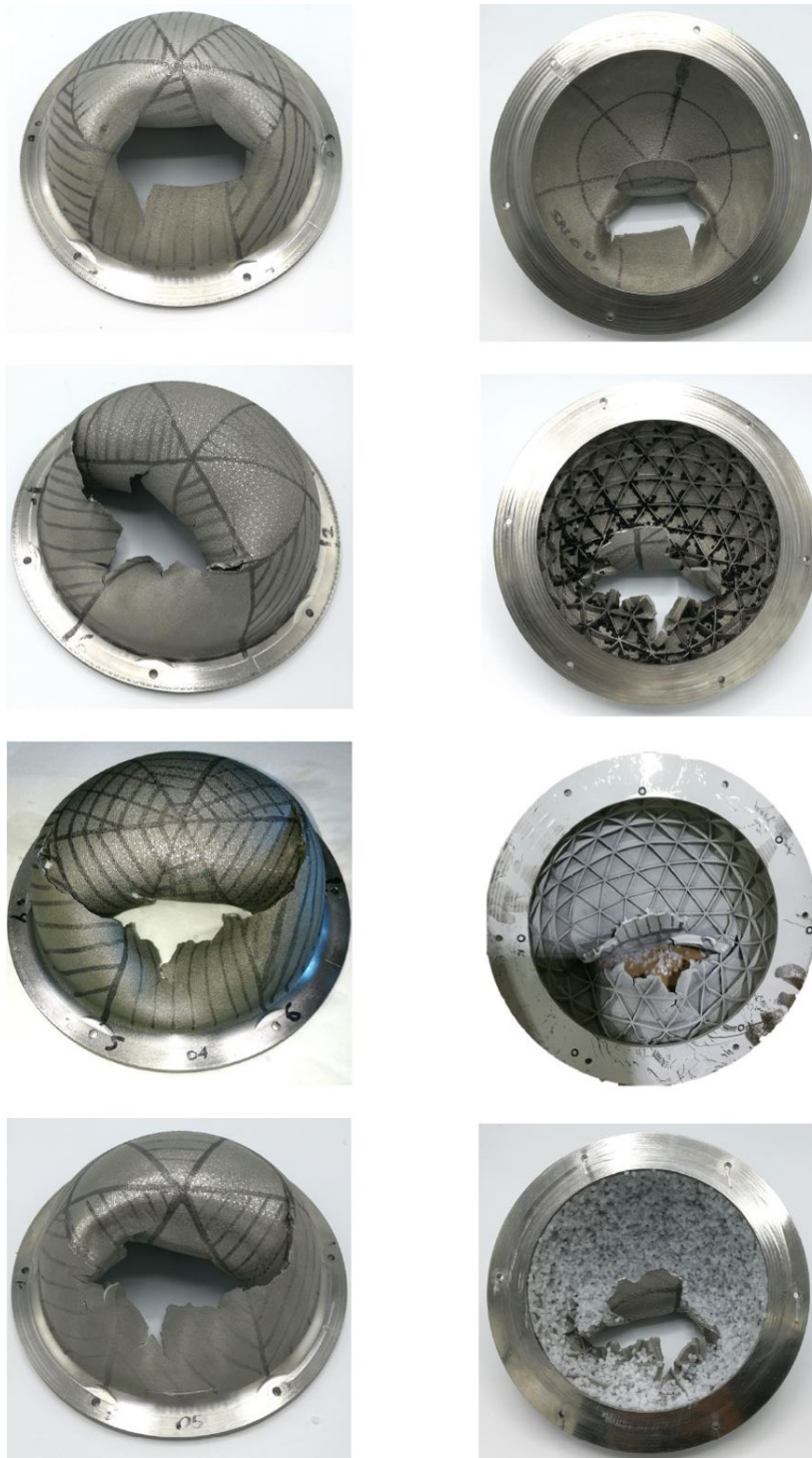
Figure 6.13: Tested components: plane-SN00 (first row), iso-SN01 (second row), iso-SN04 (third row), iso-SN05 (third row)

6.4   Relative environment test

6.4.1   Test procedure

A complete isogrid sphere has been tested at Venus-like conditions (p≈100 bar, T≈500 C) in a Hot Isostatic Pressure (`HIP`) facility. The two hemispheres have been sealed using a nickel-plated Inconel c-seal, bolted together with a set of six fasteners and set on a support. Ceramic beads were previously inserted inside the test article to reduce the eventual shock impact inside the chamber, in case of failure. During testing, Argon has been pumped in the `HIP` chamber to increase the pressure up to 98 bar ± 7 bar and electric resistances have been used to increase the temperature up to 494 C ± 14 C; these conditions have been hold for 1 hour. After pressure and temperature have been reduced to ambient, the sphere has been disassembled and inspected.

Aim of the test is investigating the behavior of the isogrid shell at high pressure and temperature, investigating possible local permanent deformations. It must be noted that the component was designed to survive in a more severe environment and no failure was expected during this experiment.

Figure 6.14: Relative environment test: test article preparation

6.4.2 Predictions

Non linear analyses have been performed using the 2D element model and considering the material properties at 500 C. Fig.6.15 show the results of the simulations.

The predicted failure pressure of the isogrid shell is approximately twice the testing pressure, being the Factor of Safety:

$$\texttt{FoS} = \frac{p_{\texttt{NL,2D}}}{p_{expt}} = \frac{198 bar}{98 bar} \approx 2 \tag{6.2a}$$

Therefore, no failure, nor plastic deformations were expected.
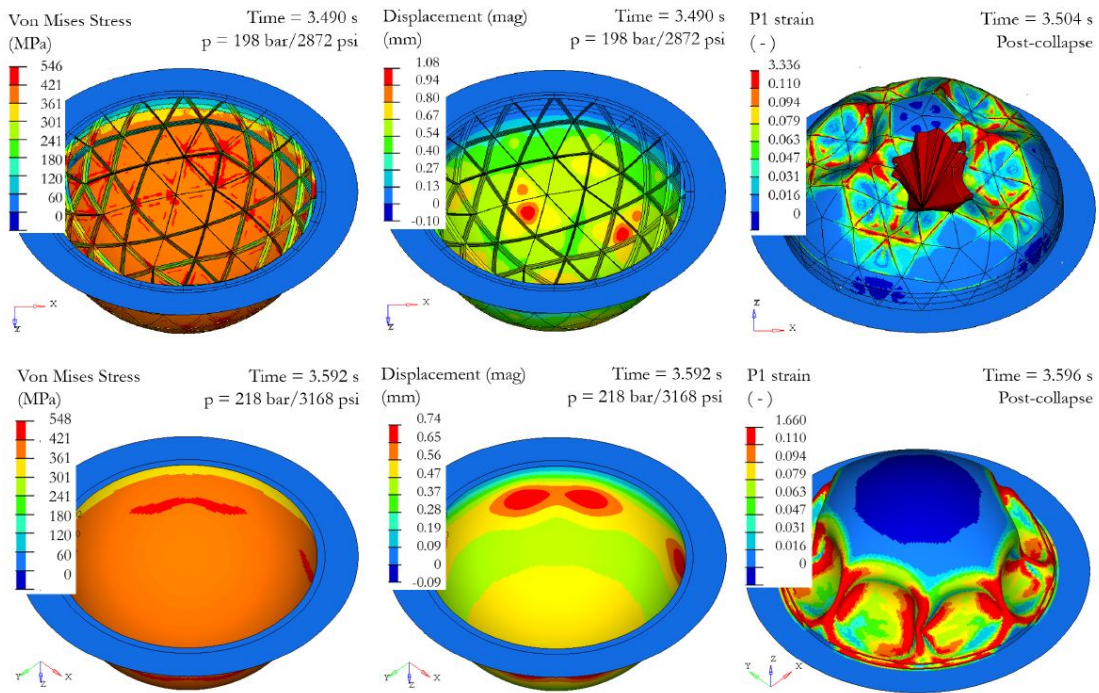
Figure 6.15: Relative environment test - shell element model

6.4.3 Results and discussion

The test was performed at the KittyHawk facility in Garden Grove, CA.

After testing, the sphere was disassembled; the ceramic beads resulted broken or damaged as visible in Fig.6.17, with a slight change of color. A change of color was also observed in the internal surface of the test article. Discoloration was observed in the flange too, but it stopped before the grove, suggesting that the c-seal worked properly. No plastic deformation was detected, as predicted by the numerical analysis.

93
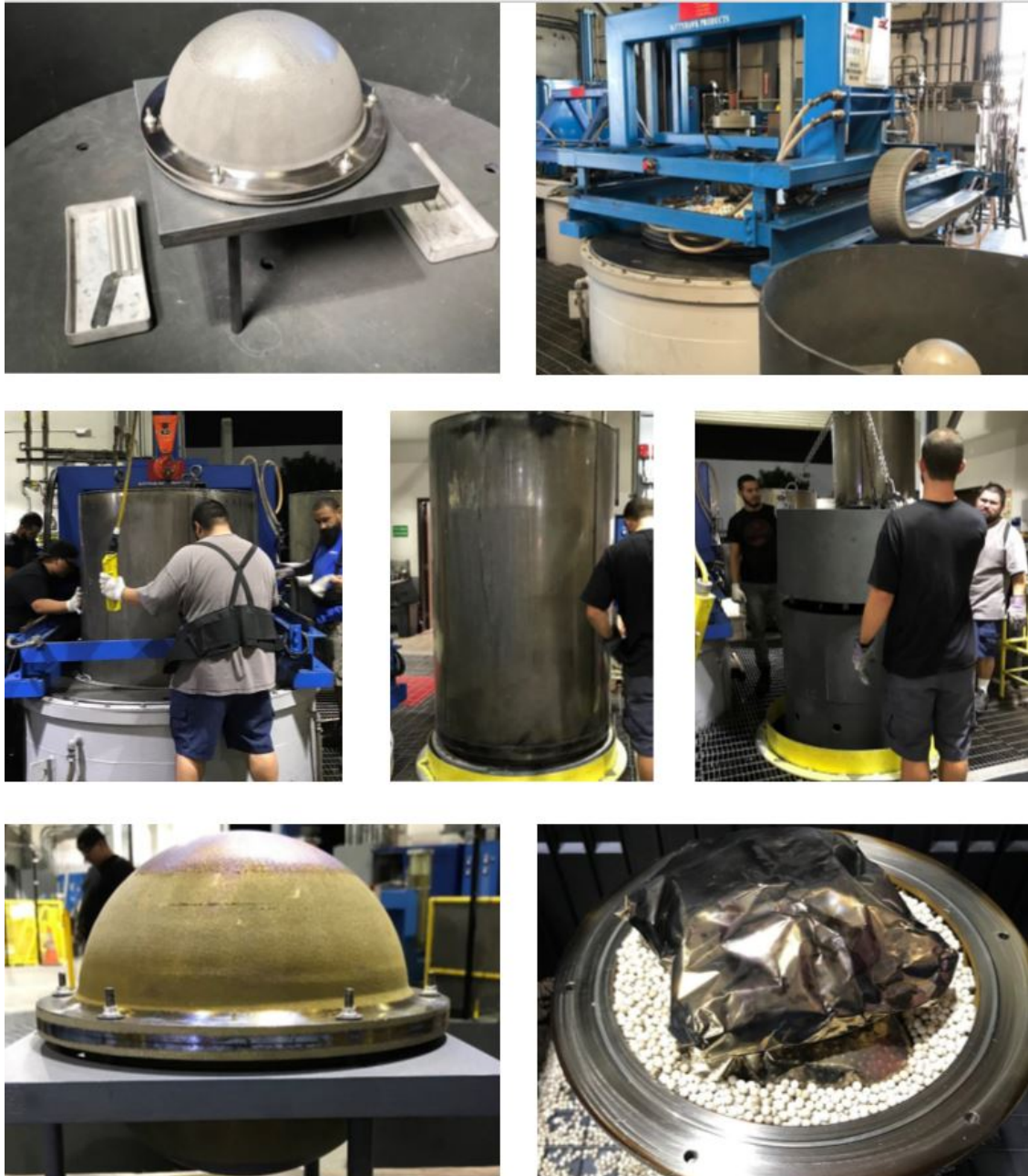
Figure 6.16: Relative environment test: test article assembled, `HIP` chamber during loading and unloading operations, test article after the test

Figure 6.17: Component after testing: external surface, damaged ceramic beads, oxidized bottom and top hemispheres.

6.5   Design Synthesis

The previous sections described the experimental campaign conducted on sub-scale components. A good agreement between the behavior of the `AM` plain shell and the literature about conventional manufacturing techniques was found, showing that `AM` can be a suitable manufacturing process for these applications. Interesting results came from the tests on the isogrid shells, which provided repeatable results in terms of both failure pressure and failure mode, and resulted in a higher buckling knockdown factor and a low mismatch with the numerical predictions.

The experimental evidence showed that isogrid-reinforced spherical shells are characterized by a repeatable and predictable behavior, even when structural instability phenomena are involved. This is crucial when designing primary structures and critical items, where reliability is fundamental. Moreover, predictable and repeatable results can also allow less conservative approaches, potentially leading to further mass reductions.

A re-design of the full scale shell, according to the lessons learned from the experimental campaign has been finally performed. A brief comparison between plain and isogrid-stiffened shells, and traditional manufacturing and `AM` will be reported as well, considering also potential fabrication cost and schedule savings.
The final section will summarize the main outcomes and will present a manufacturing demonstrator of an isogrid-reinforced shell, with an integrated porous wick, to be used as a part of a thermal control system.

95

6.5.1 Re-design of the full-scale structure

The full-scale model (R=560 mm) of the concept of a Venus lander has been re-designed considering the results of the experimental activities performed on the sub-scale components, in order to assess the potential mass savings related to the adoption of the isogrid layout.

In the re-design process, the buckling `KF` has been assumed to be the same as the sub-scale shells. According to the literature about plain shells, `KF` varies as a function of R/t ratio. For this reason, the R/t ratio of the sub- and full-scale configurations has been finally compared to check the validity of the assumption. Therefore, the full-scale geometry has been re-designed considering a `KF` of 30% for the plain shell and 44% for the isogrid one, applied to the linear buckling `FEA`. The details are shown in the following Table. The ratio R/t is equal to 53 and 75 in the case of the plain and isogrid shell respectively; hence, the hypothesis of constant `KF` can be considered as reasonable. Further experimental activities should be conducted to assess the validity of the assumptions.

Table 6.7 reports the comparison between the full scale isogrid and plain components. The mass values do not take into account the presence of the flange and neither chamfers or fillets for manufacturability improvements. As it is possible to see, mass saving due to the adoption of the isogrid layout is increased to 18% .

Table 6.6: Full scale: isogrid vs plain hemisphere

				Isogrid	Plain
Geometry	Radius	R	mm	560	560
	Skin thickness	t	mm	7.7	11.2
	Rib height	d	mm	27.0	-
	Rib thickness	b	mm	3.1	-
Linear Analysis	Buckl. Knockdown factor	KF		44%	30%
	Max stress	σ	MPa	704	399
Mass	Hemisphere w/o flange	m	kg	81	96
	Mass saving			18%	

6.5.2 Production analysis

The experimental campaign on the sub-scale components provided also the opportunity to compare traditional manufacturing techniques to `AM` processes for fabricating spherical structural shells. Quotes from an external vendor for producing 7 isogrid hemispheres and 1 plain hemisphere are reported in the following table,

listing costs and schedule.

At this scale, it has been found `AM` provided a cost and schedule saving of 26% and 79%. Savings obviously may vary depending on the production lot size, as `AM` gets typically more convenient than conventional manufacturing for smaller lot size, which are more common in space engineering. A production analysis at the full scale can not be provided, as large `AM` machines are currently still under development.

Table 6.7: Cost and schedule comparison

		Cost ($)	**Lead time**
Traditional manufacturing	- Material (8 round billets)	19 840	
	- Non recurring engineering costs	10 200	
	- Machining (7 isogrid shells)	48 485	
	- Machining (1 plain shell)	17 480	
	Total cost	**96 005**	
	Total lead time		42 weeks
Additive Manufacturing	- Fabrication (7 isogrid and 1 plain)	49 890	
	- Finish machining	21 000	
	Total cost	**70 890**	
	Total lead time		9 weeks

6.6   Conclusion

Past landing missions to Venus used primary structures consisting in plain spherical shells, i.e. without internal ribbing, which were easy to fabricate by conventional manufacturing techniques, but sensitive imperfection-triggered structural instability. In recent years, `AM` opened a range of new opportunities, including complex internal stiffening systems.
In the previous chapters, plain and isogrid-stiffened shells have been investigated, describing analytical and numerical design methods and proposing an optimization method for the isogrid layout. `AM` sub-scale components have been designed, analyzed, fabricated and tested, providing evidence for model validation. The isogrid shells exhibited promising results, showing repeatable failure modes and limited mismatch with the numerical predictions, and providing buckling KFs higher than the ones recommended by `NASA` standards or industrial application for plain spheres. Considering the full-scale structure, AM isogrid shells could provide a significant mass reduction, in respect to plain shells, together with mass and cost savings, if compared to traditional manufacturing techniques.

The development of `AM` has made feasible and somehow affordable the fabrication of lightweight complex geometries that were extremely expensive and time consuming to produce by conventional techniques. As described in the introduction of this dissertation, another great opportunity given by `AM` is the possibility to fabricate multi-functional component, characterized by intricate features or multi-materials. In the case of the concept of the Venus lander under study, integrating a two-phase thermal control system within the structural shell could provide increased thermal performances, potentially resulting in an extended mission life.

As described in Chapter 3, the thermal device under study is an evaporator, in which the working fluid at the liquid state flows through a porous wick and evaporates absorbing heat. Thanks to `AM`, the porous wick can be fabricated by tuning the process parameters, so that the metal powder is not fully consolidated, but results in a stochastic foam. Hence, systems with full-solid and porous material can potentially be fabricated as a monolithic assemblies, by mapping the process parameters.

To prove the possibility of co-fabrication, a manufacturing demonstrator consisting in a spherical shell, reinforced with an isogrid stiffening system and integrating a porous wick has been fabricated, as shown in Fig. 6.18.
`AM` two-phase thermal control systems, although possible to be fabricated, are still characterized by a low technology readiness level and are currently under development. In this context, the two-phase technology Lab at `JPL` is developing a novel thermal system [33]. The following chapters will give an overview of the technology, focusing on the design of the evaporator.
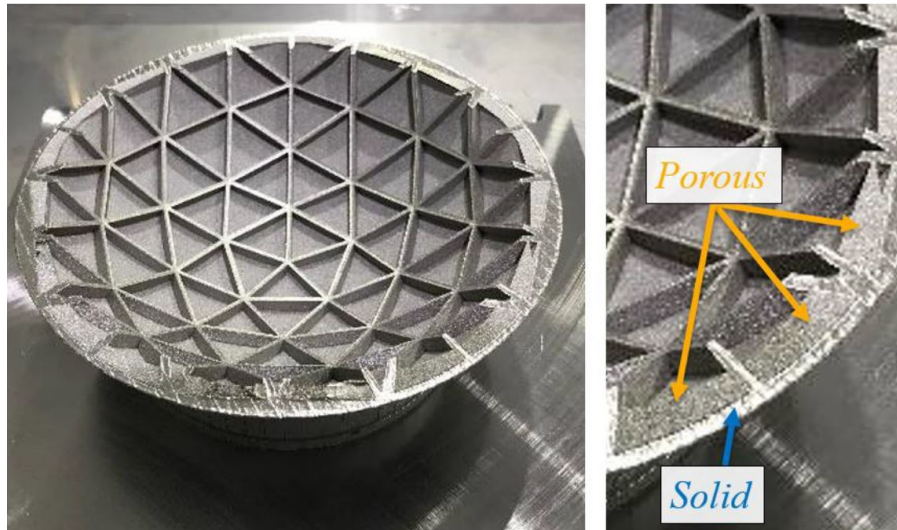
Figure 6.18: Manufacturing demonstrator of an isogrid-stiffened dome, with an integrated porous wick, to be used as part of a thermal control system

Chapter 7

Thermal control systems: two-phase AM evaporator

The surface of Venus is characterized by extreme conditions, such as very high pressure and temperature, which make the in-situ exploration really challenging. In the previous chapters, the high external pressure has been addressed by discussing the structural design of a conceptual primary structure for a Venus lander. On the other side, the extreme atmospheric temperature poses unique challenges for the thermal management. Advanced thermal control systems are currently under study, in order to enable long-lived probes and maximize the science return. AM technologies could enable the fabrication of integrated thermo-structural systems, with fluid channels running through the shell, or two-phase thermal control systems, characterized by heat pipes and/or porous wicks, to be fabricated within the primary structure, as a single monolithic component.
Among these new technologies, Two-Phase Mechanically Pumped Fuid Loop (2PMPFL) systems are currently under development at NASA Jet Propulsion Laboratory, to enable small-spacecraft missions in extreme environments [33].

This chapter will give a brief introduction to 2PMPFL systems, describing the main components, advantages and state of the art. Specific focus will be given to the Evaporator component, which is the heart of the system and will be object of the following chapters.

7.1 Overview

The thermal control system of Venus surface probes is probably one of the most critical subsystem, as described in Chapter 3. In fact, the electronic components need to be maintained within their operational temperature, typically lower than 70°C for conventional electronics; in the case of surface probes, this task is particularly challenging, as the external atmosphere is at about 462°C. Passive thermal control systems, such as multi-layer insulation materials, coatings, and Phase-Change materials, can be used to mitigate the effects of the extreme environmental conditions, and high temperature electronics, able to survive up to 120°C, can further extend the probe lifetime. However, advanced thermal control systems are needed, if the surface life of a Venus probes needs to be increased up to 24 hours.

In this frame, two-phase thermal control systems are currently under study. A working fluid, for instance water or ammonia, is used to absorb the heat generated by the electronics and shield the payload form the incoming heat leaks from the atmosphere, by evaporating, circulating and being vented outside. By using a two-phase system, it is possible to take the advantage of the latent heat of fusion of the working fluid, enabling the absorption, transport and dissipation of an increased amount of waste heat. Moreover, the high degree of isothermality typically achieved by two-phase systems makes these technologies particularly suited also for science instruments, which may require temperature-controlled platforms.

Advanced two-phase thermal control systems, such as Two Phase Mechanical Pumped Fluid Loop (2PMPFL) systems, are currently under development at NASA Jet Propulsion Laboratory, [117, 33, 34, 35]. 2PMPFL systems are two-phase thermal control systems in which a working fluid is used to absorb waste heat, generated for instance by electronic components, transport it and reject it outside. A scheme of a 2PMPFL system is shown in Fig. 7.1, together with the main components.

A mechanical pump is used to circulate the liquid fluid within the loop. At the evaporator, the fluid flows through a porous wick and absorbs the waste heat by changing its phase from the liquid to vapor and then flows to the condenser, where the heat is rejected to the outside and the vapor returns back to the liquid phase. The liquid then flows through a sub-cooler and an accumulator, used to control the pressure of the system, and finally goes back to the pump. A by-pass line is present as well, to provide an additional flow path to the liquid, so that the fluid flowing through the evaporator is regulated by the capillarity force of the wick, and not by the mechanical pump.

2PMPFL systems allow an increased flexibility in the design and in the thermal management [33]. Moreover, being the fluid mechanically pumped, multiple
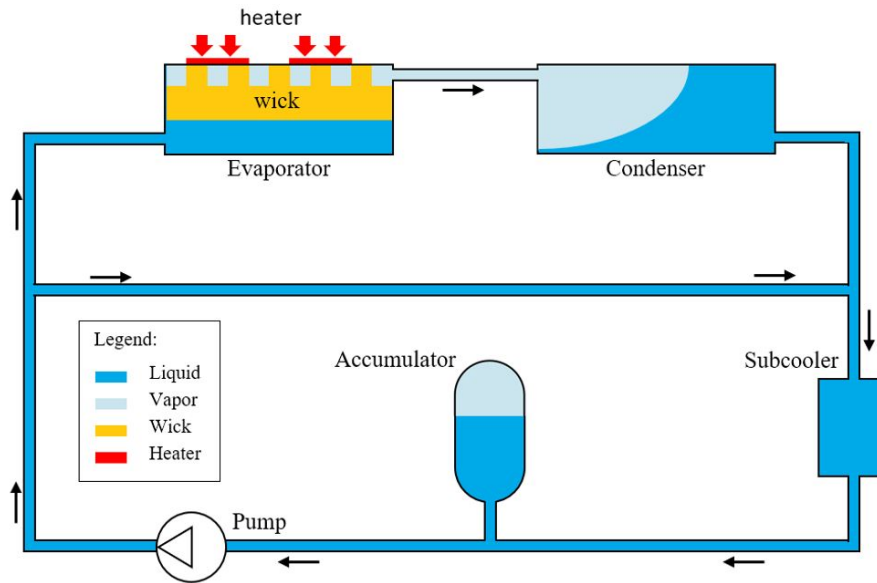
Figure 7.1: Schematic of a `2PMPFL` system

filling and draining operations are possible, making easier the integration of the system. `2PMPFL` systems may also provide mass and power savings, if compared to traditional two-phase loops [117].

7.2 JPL Testbed

A `2PMPFL` experimental testbed has been set up by the Two phase laboratory team at `NASA` Jet Propulsion Laboratory and experimental campaigns have already been performed, showing promising results [34]. A top view of the testbed at the Laboratory is shown in Fig.7.2, together with a schematic of the main components and regulation valves. Sensor and instruments, such as flowmeters, thermometers, infrared cameras and data acquisition system, are used to monitor and control the test bed.

Since the first prototype of the testbed, several hardware improvements have been performed, and different working fluids have been used, such as water, ammonia or FC-72. The main modifications regarded the evaporator, which is the core of the system. Heaters are located on the top surface of the evaporator, simulating, for instance, the waste heat provided by typical electronic components. The working fluid flows into the evaporator through the inlet port, evaporates absorbing the heat and flows to the outlet, as vapor. It must be noted that evaporation is an iso-thermal process, as the heat is absorbed as latent heat of evaporation, and the evaporation temperature is controlled by the saturation pressure of the fluid.
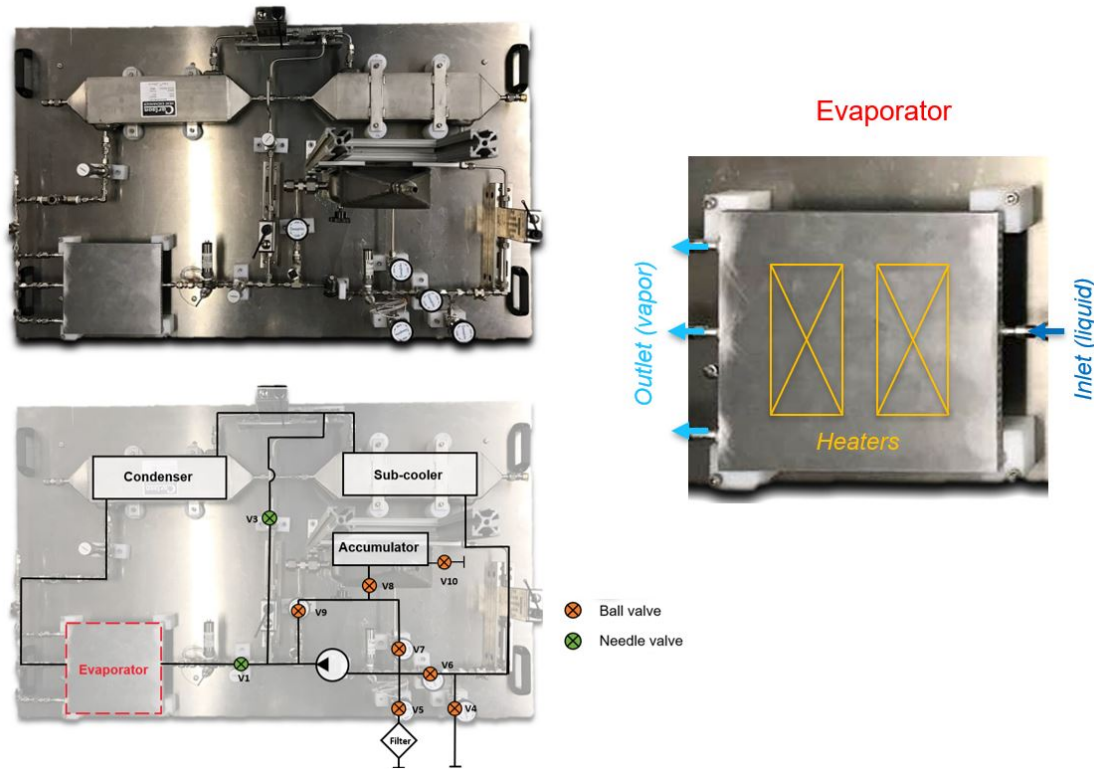
Figure 7.2: `2PMPFL` test bed set up at `JPL` - top view

Hence, by controlling the fluid pressure at the accumulator, it is possible to have a control on the temperature of the evaporator, i.e. the temperature of the electronic components. For instance, when ammonia is used as working fluid, the evaporation temperature can be controlled at 25C or 40 C, if the pressure of the fluid at the accumulator level is set at 10 bar or 15 bar respectively.

The evaporator structure will be described in the following section.

7.3 The evaporator

A schematic of the cross section of the evaporator is given in Fig. 7.3. Liquid and vapor chambers are located at the bottom and at the top of the evaporator respectively, divided by a wick, made of porous material. The wick geometry and material properties, such as porosity and pore size, are fundamental variables, that need to be optimized to improve the thermal performance of the evaporator. Thanks to the wick permeability, the liquid can be sucked by the capillary force up to the boundaries with the vapor groves, where it evaporates. Porous pillars connect the with to the top surface of the casing, while solid struts can be used to

connect top and bottom skin, limiting the deformations during operation, due to the internal pressure.
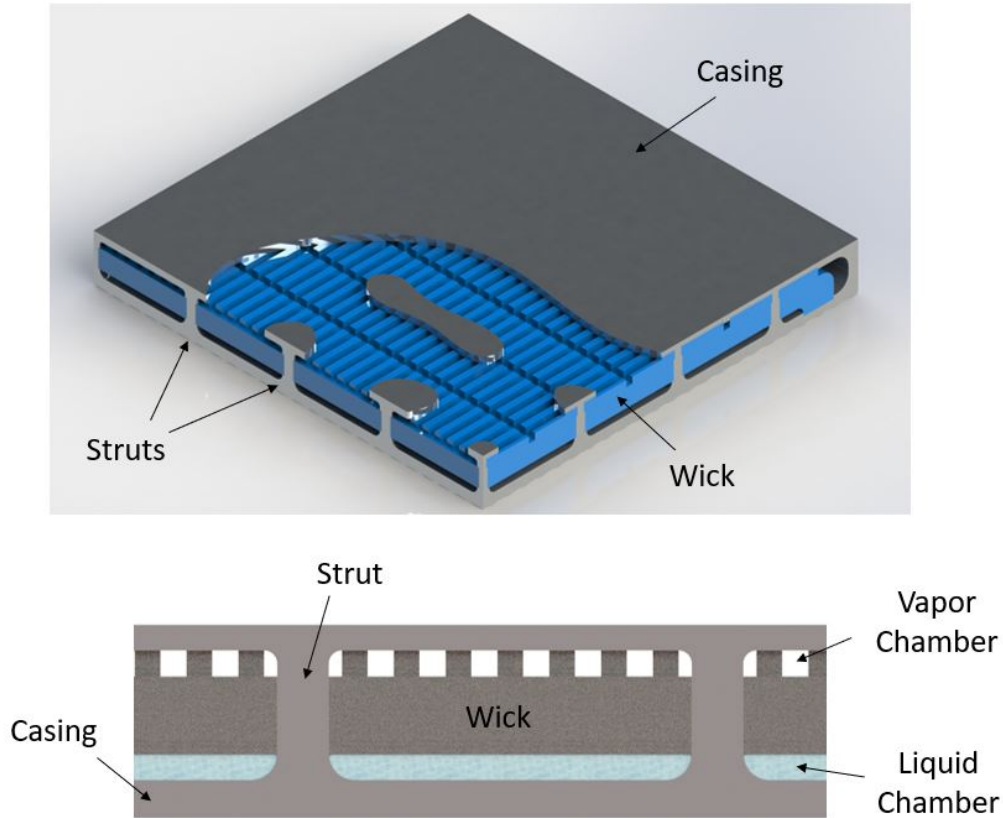
Figure 7.3: Scheme of the evaporator

The first prototype, described in [117], was fabricated as an assembly composed by three components: the base and the top of the casing, made of full-solid aluminum fabricated by conventional manufacturing techniques, and the wick, made of sintered porous steel. The three parts were finally sealed using an O-ring. On one side, conventional manufacturing techniques allow to obtain well known material properties, for both the solid and the porous part; on the other, they limit the design freedom, making necessary assembly and integration operations and requiring adequate sealing systems to contain the pressurized fluid and avoid leakages.
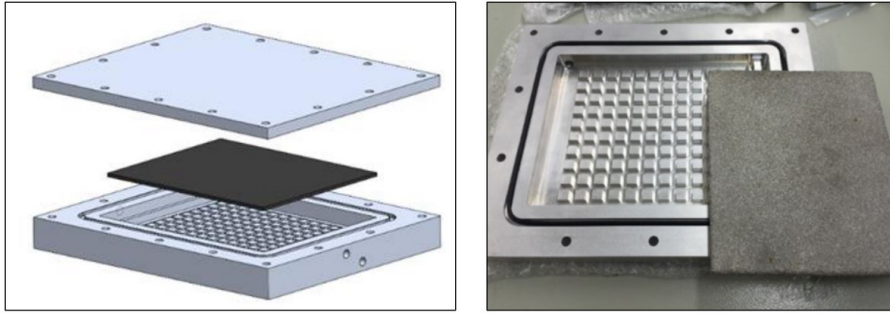
Figure 7.4: Evaporator 1 - scheme and component, adapted from [117]

`AM` has revealed as a game-changing technology. In fact, by tailoring the process parameters, it is possible to obtain full-solid, or porous material within the same component. In this way, no integration or sealing are needed and more complex geometries can be fabricated, including for instance internal lattice infill to help in withstanding the structural loads, or conformal vapor channels, or non-planar evaporators [36].

A new evaporator (2nd generation) was designed and fabricated by `L-PBF` as a monolithic component. Tests at low pressure with FC-72 fluid were performed and promising results led to the design of a new `AM` evaporator, to be used with ammonia with a maximum operational pressure of 13.9 bar. This 3rd generation was characterized by a significantly thinner form factor, accommodating an array of 25 square-section struts, equally spaced and linking the bottom surface to the top surface of the evaporator.
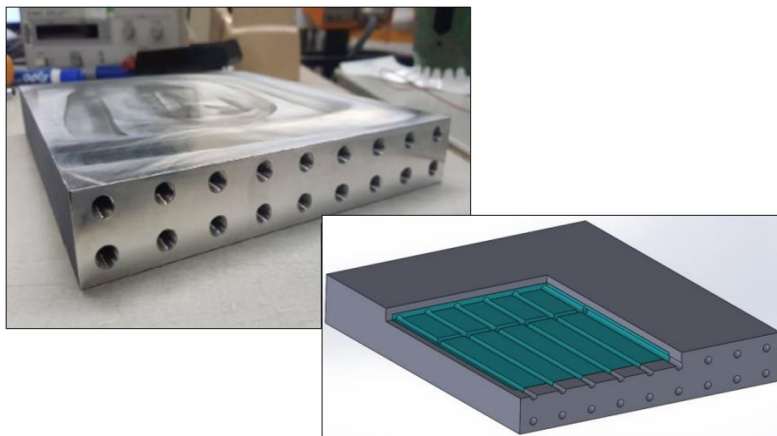
Figure 7.5: Evaporator 2 - scheme and component, adapted from [35]
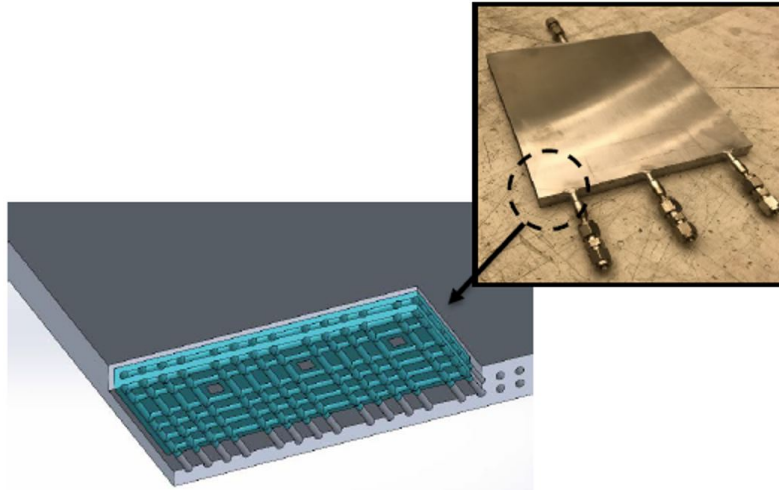
Figure 7.6: Evaporator 3 - scheme and component, adapted from [35]

Further improvements were achieved by Evaporator 4, in which 36 circular-section struts were used, to further reduce the mass and thickness of the casing, as it will be presented in the following chapters, together with Evaporator 5.
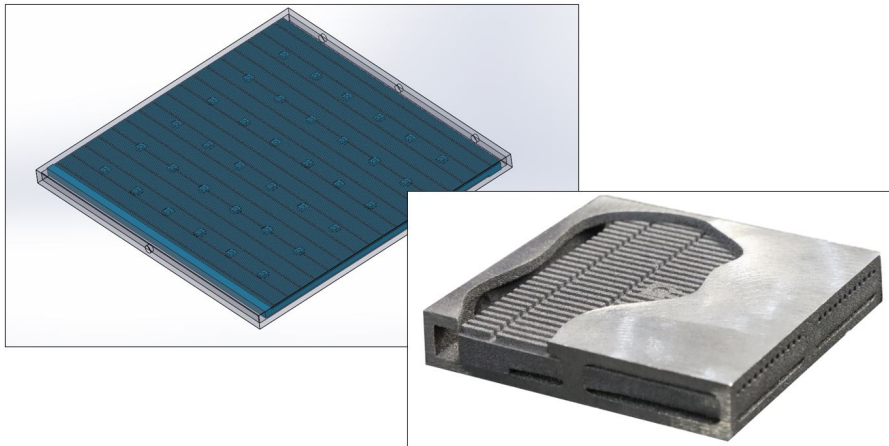
Figure 7.7: Evaporator 4 - scheme and showpiece

An outline of the evolution of the evaporators over time is summarized in Fig.7.8.

Researcher investigated `AM` of porous metals, including Titanium, Aluminum and Steel alloys, focusing on tuning the process parameters to achieve optimal thermal properties of porous wicks [36]. In the case of AlSi10Mg, it is possible to fabricate porous media with a porosity ranging from 2% to 55%, a pore size ranging from 5 to 150 μm, and permeability ranging from 10^{-11} to 10^{-18} m^2.
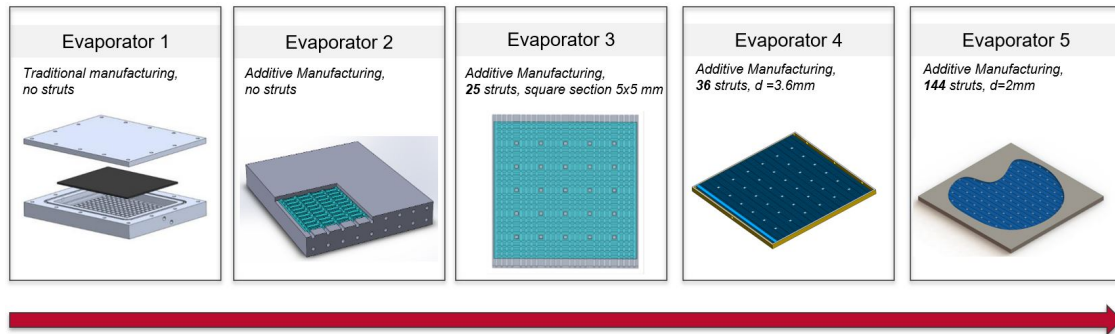
Figure 7.8: Evaporator design evolution, from generation 1 to 5, from [39]

In this context, the present work is focused on a concept of an optimized evaporator, considering the structural performance and possible manufacturing limitations. Hence, holding a pressurized fluid, the evaporator can be considered as a pressure vessel. Its unusual geometry, being square vessels not optimal in withstanding internal pressure loading, makes the design and the optimization an interesting structural problem, in which the main design variables are the casing thickness and the lattice infill. In fact, as mentioned in the previous pages, an array of vertical full-solid struts is integrated within the evaporator, to help in limiting the deformations during operations.

The third peculiarity of this component, beside the unusual shape and the internal struts, is obviously the non conventional fabrication technique. Hence, AM is a relatively new technology, for which process qualification procedures have been recently proposed [118] and still under development. Pressure vessels could probably be a very interesting application for AM, as non conventional shapes could be easily obtained, together with single-piece assemblies, with embedded valves or manifold, reducing the need of sealing or welding [119, 120]. In this context, researchers and industry are working to provide robust design procedures and criteria for AM pressure vessels, starting from the material characterization, to the non destructive inspection techniques [119, 121, 122]

Aim of the present work is to provide a new design of the evaporator (i.e. the 5th generation), focusing on the structural performance and assessing the typical manufacturing limitation of L-PBF. In particular, the work is focused on the small struts connecting top and bottom surface of the component. Previous evaporators already used struts to help in withstanding the internal pressure; however, the design was limited by the unknowns related to the manufacturing process, especially in fabricating thin struts. This resulted in configurations characterized by thick strut, sub-optimal from both the structural and thermal point of view.

The next chapter will describe some experimental activities performed on `L-PBF` AlSi10Mg lattice structures, aimed at assessing the manufacturability of small struts. The results of these activities have finally been used in the re-disgn of the evaporator, that will be presented in Chapter 10.

Chapter 8

AM technology and limitations

The design of the evaporator uses an internal matrix of small struts to improve the structural and thermal performances. This configuration can be obtained by Additive Manufacturing, which has already been chosen as manufacturing technique, as it enables the fabrication of the full solid casing and the porous wick as a monolithic part. However, some issues could arise in the fabrication of small struts.

This chapter gives a quick overview of the main manufacturing imperfections related to small struts fabricated by `L-PBF`. An experimental campaign aimed at assessing the typical manufacturing imperfections has been performed, in order to get some sensitivity of `AM` limitations, before designing the lattice infill for the evaporator. The goal of the activity is to characterize the imperfections in small AlSi10Mg struts, such as the deviations from the nominal geometry or the internal porosity, considering a range of orientations in respect to the building directions, as well as different process parameters. Hence, a procedure for quality inspection has been proposed, as a tool for qualitative and quantitative comparison during the development of the optimal process parameters.

8.1 Lattice structures

The evaporator object of the study is characterized by a number of struts infilling the case, aimed to provide additional structural stiffness and resistance. In fact, the expansion of `AM` boosted the development of components with complex internal features, such as channels, struts, or lattice structures, that are very difficult or even impossible to fabricate by conventional manufacturing techniques. In this context, lattice structures are formed by a spatial repetition of a simple unit cell, typically consisting in interconnected struts. They can be used, for instance, to infill shell structures, providing a significant increment of stiffness, by adding a few mass. Potential fields of application can range from lightweight structures, to shock absorbers, to pressure vessels and heat exchangers [23, 123]. They are also referred to as "architected materials", as it is possible to tune the structural, thermal or electrical properties by varying the strut diameter, or by changing the dimension or the type of the unit cell. Optimization methods based on analytical formulations are under study, aimed for instance at the design of truss cores for sandwich structures [124].

Even a small variation of the strut diameter can result in a variation of the behavior of the entire component; therefore, controlling the quality of the struts becomes crucial [125, 126]. This can get even more critical considering that `AM` processes are characterized by very high variability, depending on the process parameters, the hardware of the machine, the raw material and post-processes. For this reason, an increasing effort is being made by research laboratories to develop standard procedure and methodologies for inspection and quality control [22, 12], aimed at providing robust tools for improving the entire manufacturing cycle and for obtaining more accurate predictions of the behavior of the products, in both the verification and the design stage [127, 128, 129, 130]

8.2 Overview of typical imperfections of small struts

General recommendations for designing components to be produced by `AM` suggest to avoid small features and limit the unsupported overhang lengths, i.e. limit the surfaces forming low angles in respect to the building plate and being supported just by the unmelted powder. In fact, the difference between the thermal conductivity of powder and solid material can strongly affect the thermal behavior during melting and solidification, typically causing imperfections [131]. Moreover, the machine hardware and the process parameters influence the laser spot and the minimum feature that can be successfully fabricated. Hence, the fabrication

of lattice structures can be extremely challenging, as they are typically characterized by thin struts having different orientations in respect to the building direction which may often results in large imperfections, causing the rejection of the product.

Fig.8.1 shows disconnected struts and very large internal pores generated during the fabrication of small struts using not optimal process settings. Indeed, the main types of defects typically observed are geometric imperfections and internal porosities.
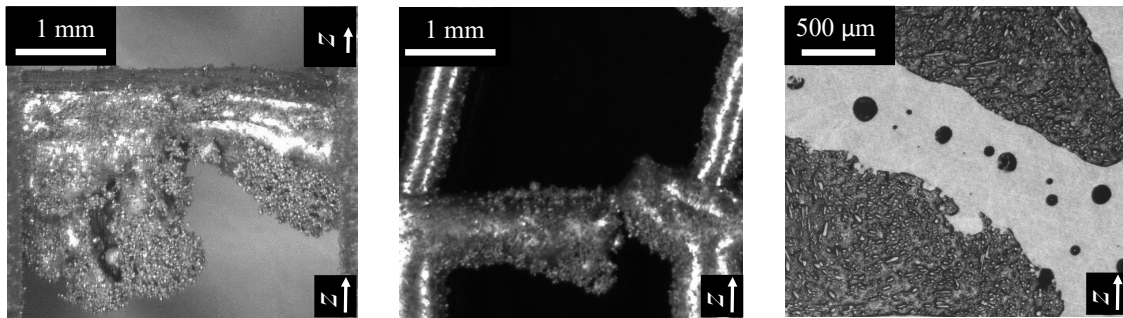
Figure 8.1: `L-PBF` AlSi10Mg struts: fabrication failures (specimens from the experimental activities described in the following)

Geometric imperfections can range from surface roughness to large deviations from the nominal geometry [132]. At the small scale, partly-melted parasitic particles can result in very high surface roughness, which can also be triggered by the staircase effect typical of `AM` processes. At a larger scale, too high energy can cause over melting, resulting in over-sized struts and flashing in the unsupported overhangs, so that circular struts might become oval [133]. Controlling both small scale and large scale imperfections is necessary, as they can strongly affect the behavior of the final component: for instance, high surface roughness can significantly reduce the fatigue life, triggering crack initiation; moreover, smaller strut dimensions result in lower stiffness and resistance.

Several researches have been published and are in progress about the characterization of geometric imperfections [131, 134, 135], as a function of process parameters, strut size and strut orientation in respect to the building direction, by using different experimental techniques, such as optical microscopy, profilometry, or computed tomography [136, 132] Moreover, researchers are investigating different strategies to reduce the imperfections by optimizing the process parameters [133, 125, 137], mitigating their effect by post-processing [138], or compensate them before fabrication, during the design stage [139].

The second critical class of imperfections is porosity. `L-PBF` AlSi10Mg struts typically suffer of different types of porosity, being mainly lack of fusion (`LoF`),

with irregular shape and mainly caused by process settings with insufficient energy density, and keyholes, preferentially located at the edges and characterized by an elongated shape. Oxide particles and supersaturated gas absorbed may also cause internal large and small pores, respectively. Other classifications of internal pores have also been proposed. For instance, Sola et al. [140] classified porosity in 3 types, based on its origin:

1. equipment related: misalignments of the optical hardware of wrong calibration may result in imperfect fusion,

2. powder related: incorrect handling and storage of the powder may results in moisture absorption and hydrogen pores,

3. process related: not optimal process settings may result in imperfect fusion; for instance, excessive energy may cause keyholes, and insufficient energy may cause `LoF`.

Internal porosity can be particularly detrimental, especially for structural applications subjected to fatigue loadings, as internal pores reduce the load carrying section, act a stress raiser, and trigger cracks initiation, reducing the static strength and fatigue life [10, 141]. Hence, assessing the porosity of components characterized by lattice structures is mandatory, by recurring to non destructive testing, or by estimate the porosity using statistical methods. The overall density of the part can be easily performed by using experimental techniques, based on the Archimedean principle, but they can not provide indications about size, shape and location of the defects, which for instance is fundamental for predicting fatigue life [19, 22]. Hence, Computer Tomography (`CT`) must be used, or, in case of sacrificial specimens, metallography.

8.3 Experimental activities

Some experimental activities have been performed, aimed at:

- assessing the capabilities and limitations of `L-PBF` in fabricating small AlSi10Mg struts,

- developing a quality inspection procedure for small struts,

- comparing strut obtained by using different process settings, as a part of the development of process parameters optimized for fabricating small struts.

To this end, dedicated specimens have been designed, fabricated and inspected, to assess both qualitatively and quantitatively the quality of the parts. In addition, quasi-static compression tests have been performed, as a first step in the characterization of the mechanical proeperties.

8.4   Preliminary assessment

A first assessment has been performed by recurring to bridge-like specimens, in which the circular struts under investigation are connected to thick, square pillars, as shown in Fig.8.2, so that for each specimen, different strut orientations (0°, 22°, 30°, 45° , 90°) and different unsupported overhang lengths up to 4 mm have been obtained. The thick, square pillars, although redundant, make the design more robust and appropriate for the early stages of the assessment.
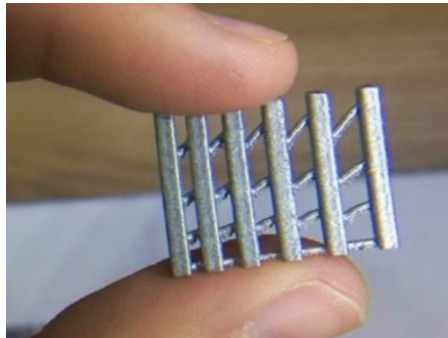
Figure 8.2: Bridge-like specimen

Two sets of specimens having strut diameters ranging from 0.5 mm to 1.2 mm have been fabricated in AlSi10Mg with an EOS® M290 `L-PBF` machine with two different process parameters, being the reference settings (*Ref*), and higher energy settings (*High-E*). No mechanical or thermal post-processing have been performed after the fabrication. Qualitative visual inspection has been performed with an optical microscope.

Considering the *Ref* specimens, it is possible to observe that strut diameters smaller than 1 mm can be successfully fabricated, although very small struts ($d_n <$ 0.8 mm) can show significant deviations from the nominal geometry, such as waviness or cylindricity errors. Moreover, decreasing the strut diameter, the influence of the surface roughness becomes more detrimental, representing a non negligible fraction of the total cross sectional area, as shown in Fig.8.3.
Secondly, low angled struts have been successfully fabricated, even with unsupported overhangs up to 4 mm. However, it must be noted that the down-facing surfaces showed higher roughness and more parasitic particles, as shown in Fig.8.4, having oval cross sections, with the larger diameter along the building direction.
Finally, the two process parameters have been compared. As shown in Fig.8.5, the higher energy density resulted in a better surface finish, especially in the case of vertical struts. However, as clearly visible in Fig.8.6, the high increment of the energy density caused also over-melting, resulting in oversized struts, large deviations from the perfect shape and flashing, in particular in angled struts.
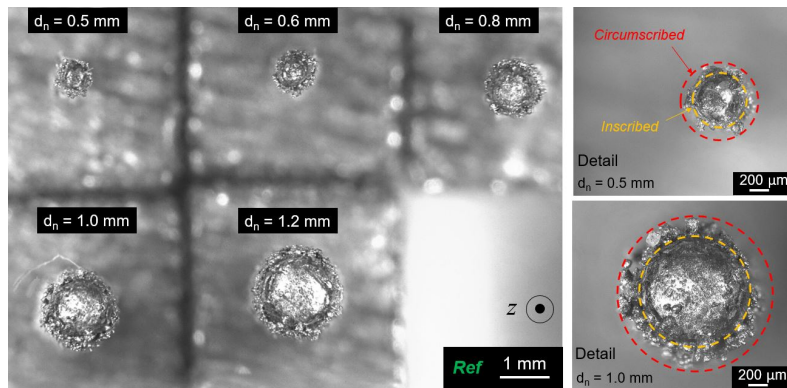
Figure 8.3: Top view of the vertical struts, *Ref* settings. The building direction is indicated as *z*
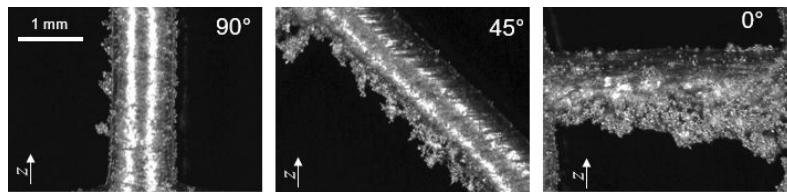
Figure 8.4: Comparison between different strut orientations: 90° (parallel to the building direction), 45°, and 0° (perpendicular to the building direction)
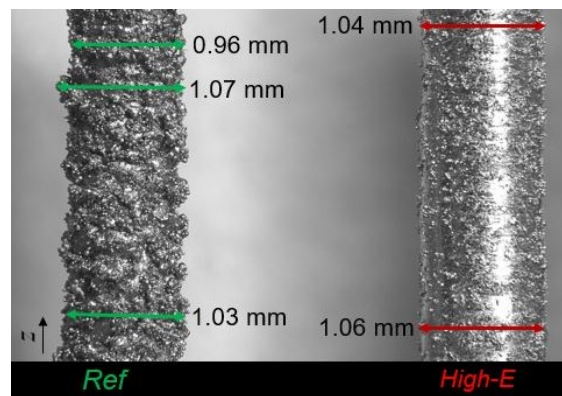
Figure 8.5: Vertical struts with a nominal diameter of 1 mm fabricated using the *Ref* settings (left) and the *High-E* settings (right)

114
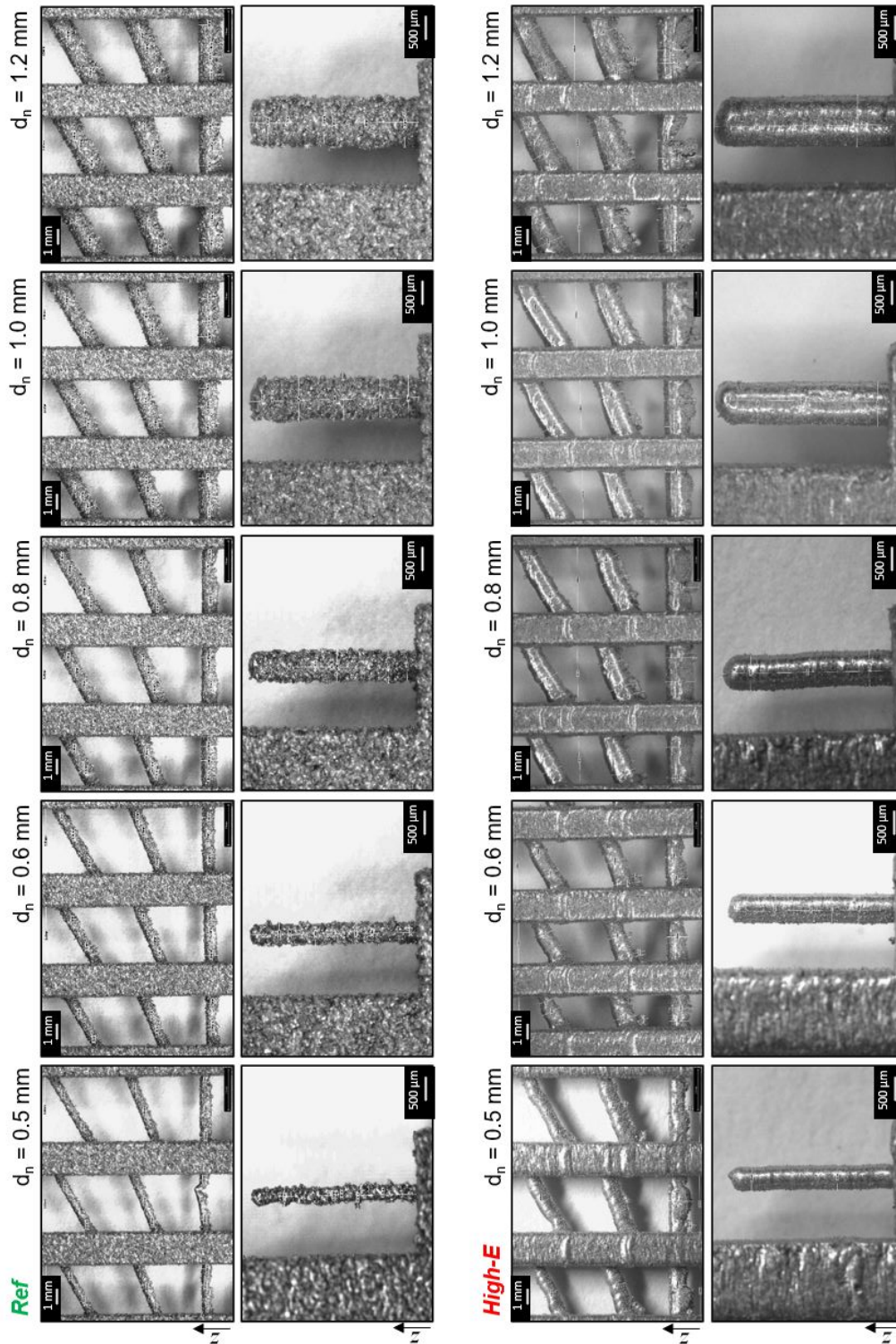
Figure 8.6: Microscope images of the bridge-like specimens, fabricated usign the *Ref* settings (first two rows) and the *High-E* settings (last two rows)

115

8.5 Quality inspection

A more detailed analysis has been then performed by recurring to a dedicated specimen, in order to quantitatively assess the strut quality, considering both the geometry deviations and the internal defects. The geometry of the specimen, adapted from Bagheri et al.[139], consists of a spider-web layout of circular struts having multiple orientations, as shown in Fig.8.7, in which a plane of symmetry allows to have to different measurements per strut orientation and overhang length. Compared to the bridge-like specimen, the spider-web is lighter, i.e. faster to fabricate, easier to inspect, and is more representative of a typical lattice structure, as the struts are connected together into nodes and not to bulk pillars. However, it must be noted that the spider-web specimens is more fragile, especially in case of very small struts and potentially subjected to be broken during the manufacturing process by the recoater blade, so that it may be not usable during the early stage of the optimization of the process parameters.

In this activity, a nominal strut diameter of d_n=1 mm have been considered, with a maximum overhang length *A* of 4.5 mm, as shown in Fig.8.7. The specimens have been fabricated in AlSi10Mg by using the *Ref* process parameters and by a second set of parameters, specifically developed, referred to as *Opt*, having higher laser power and lower scan speed. Details on process parameters cannot be disclosed. No mechanical or thermal post-processing have been performed after fabrication.
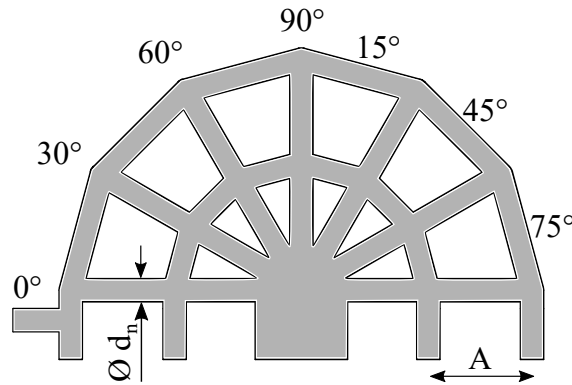
Figure 8.7: Spider-web or Peacock-tail specimen (on the left), bulk specimen for surface roughness measurements (on the right)

The specimens have firstly been inspected by optical microscopy; no macroscopic failures have been detected. The *Opt* samples showed improved surface finish, especially in the up-skin and lateral surfaces, while flashing and parasitic particles affected the down-skin surfaces. The *Ref*, instead, showed higher surface

116

roughness, more uniform in the different directions. Going from *Ref* to *Opt*, a significant improvement in surface finish is evident, as shown in Fig.8.13. However, the improvement affects especially the lateral and the up-skin surfaces, while the down-skin ones appears quite rough.
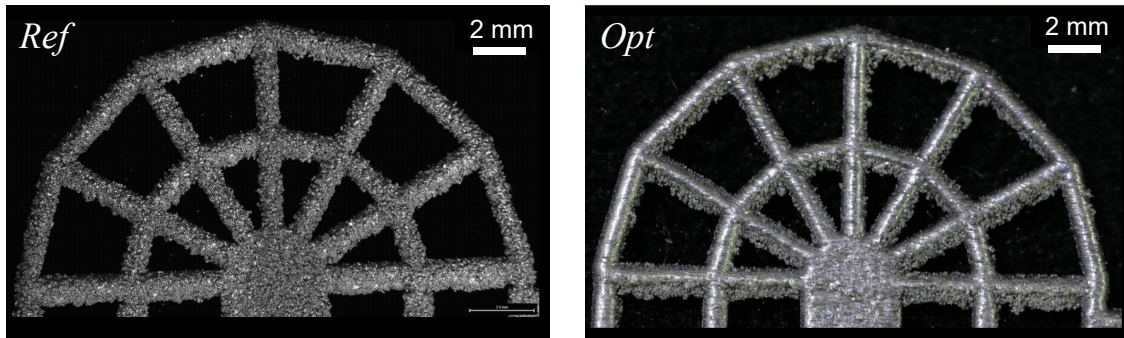
Figure 8.8: Images of *Ref* (left) and *Opt* (right) at the optical microscope

8.5.1 Dimensional check

After fabrication, dimensional inspection have been by three dimensional scanning using a Zeiss® Comet 5M and the software Geomagic Control X® to compare the measured points with the nominal `CAD` geometry. First, a three dimensional contour plot has been obtained, in which the deviations in respect to the nominal are highlighted with different colors, based on the error, as shown in Fig.8.9.
Then, each strut has been analyzed, by evaluating the smaller cylinder circumscribed to the experimental points, or Maximum Material (`MM`) cylinder, the largest cylinder inscribed into the experimental points, or Least Material (`LM`) cylinder, and the cylinder that best fitted the experimental data (`BF`). Despite the lack of a dedicated standard approach, the Geometric Dimensioning and Tolerancing (GD&T) is used, by recurring to the Cylindricity and Run out error, defined in respect to the best-fit axis and the nominal axis respectively, as shown in Fig.8.10.

Fig.8.11 shows the results of the inspection of *Opt* samples; two specimens have been inspected, so that 8 strut per orientations have been evaluated, for a better repeatability. According to the three dimensional contour map of the deviations from the nominal geometry, the specimens did not suffer from global distortions related for instance to residual stresses. However, local deviations up to ±0.2 mm can be observed, especially in the down-facing surfaces of the low-angled struts. The over material could be probably be related to over-melting, or to partly-melted parasitic particles. The plot on the right of Fig.8.11 shows the diameters of the `BF`, `MM`, and `LM` cylinders, as a function of the strut orientation. For small angles, i.e. horizontal or almost horizontal struts, a large difference between `MM` and `LM` diameters can

117
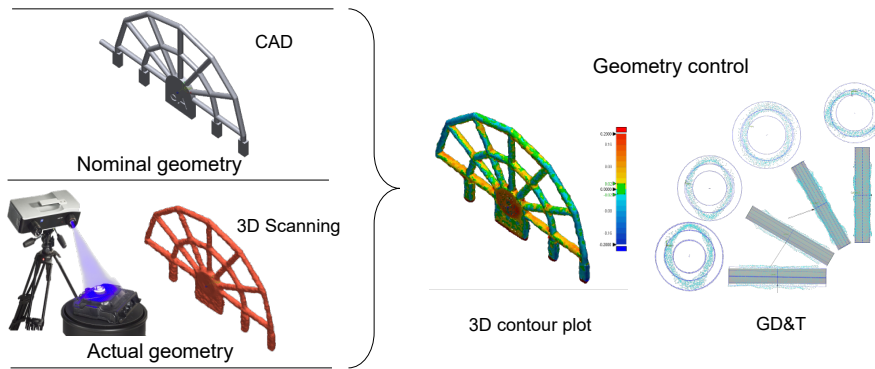
Figure 8.9: Deviations from the nominal geometry: inspection technique
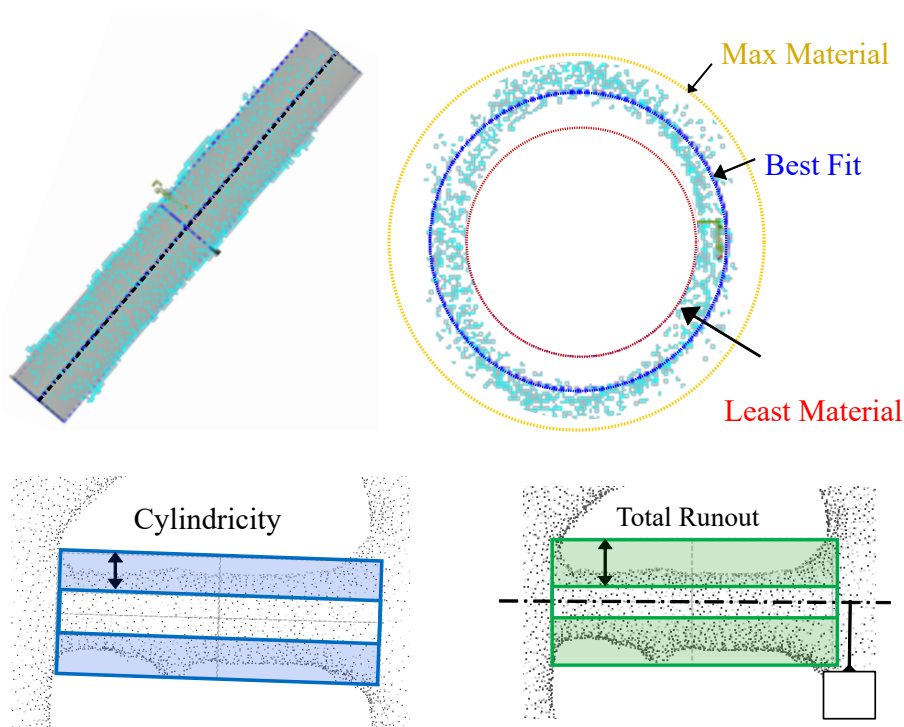
Figure 8.10: Deviation from the nominal geometry: definition of `MM`, `LM`, `BF` cylinders, cylindricity, and runout

be observed, suggesting that the over-melting made the cross section oval, as also visible from the contour maps. The large scattering of the results, especially for the `MM` diameter, could be related to the presence of local parasitic particles and flashing. Increasing the strut angle, from horizontal to vertical, the `MM` and `LM` diameters tend to converge to the `BF` diameter, also reducing the scattering between different struts and reaching plateau after 45°.
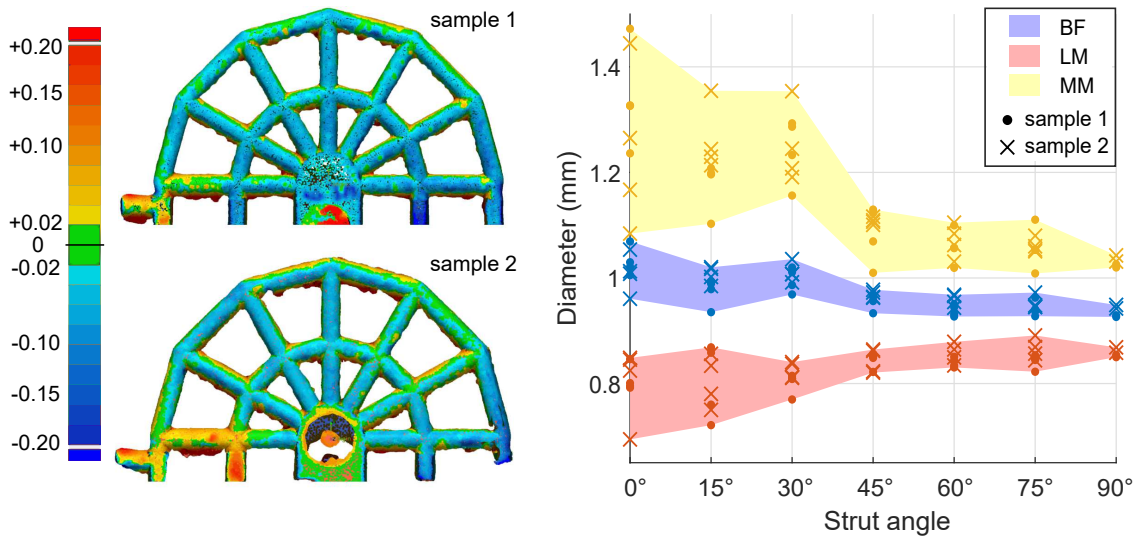
Figure 8.11: Deviation from the nominal geometry as a function of strut angle for *Opt* setting; two samples are analyzed

Finally, *Ref* and *Opt* specimens have been compared, as shown in Fig.8.12. Considering the best fit diameter, the *Ref* struts resulted undersized for all strut orientations, while the *Opt* struts were closer to the nominal diameter. *Opt* settings produced struts closer to the cylindrical shape, with lower cylindricity errors, except for the very low angles, probably because of the parasitic particles. Similar considerations apply also to the run out error, with *Opt* struts closer to the nominal shape.
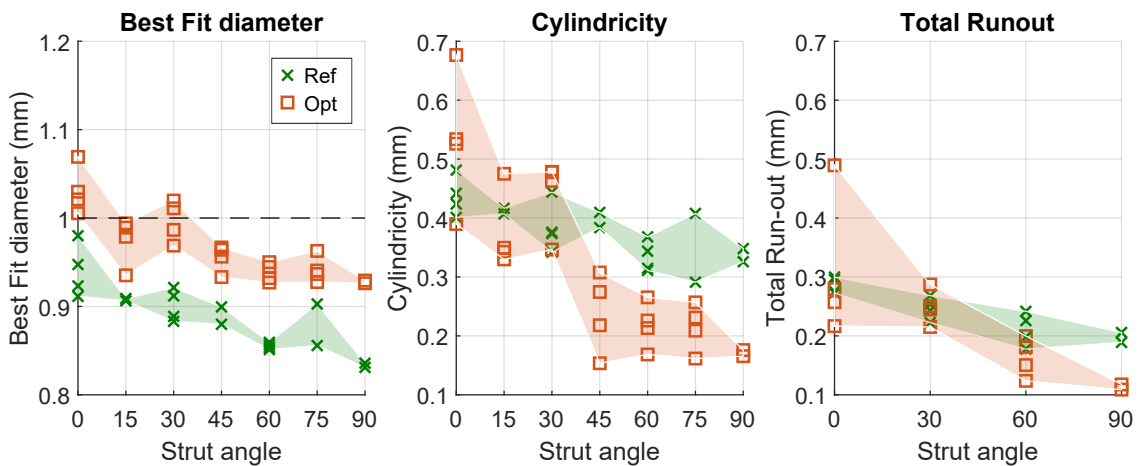
Figure 8.12: Deviation from nominal geometry: comparison between *Ref* and *Opt* settings

8.5.2   Internal defects

Then, the internal porosity has been assessed. The specimens have been prepared by being mounted onto bakelite puck, grounded to the mid-plane and polished by grits and diamond slurry. An optical microscope have been used to inspect the specimens and get images, to be inspected by Fiji Image J [142]. Number and size of pores have been quantified by analyzing each strut, as showin in Fig.8.14. A value of cross sectional density has been evaluated per each strut as well, as the complementary of the ratio between the cumulative pore area and the total cross sectional area. It must be noted that this is an index of the two dimensional porosity referred only to the specific cross section inspected.

The results relative to the *Ref* and *Opt* specimens have been reported in Fig.8.14. The cross sectional density increases increasing the strut angle, i.e. horizontal struts are more likely subjected to internal porosity, reaching a plateau for angle larger than 45°. The *Opt* struts show density levels higher and less scattered.
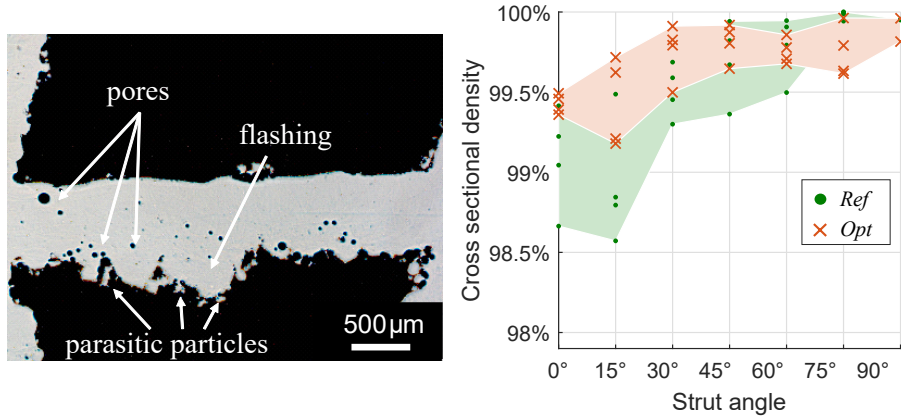
Figure 8.13: Image of a cross section of an horizontal strut processed by Fiji Image J [142] (left) and cross sectional density of *Ref* and *Opt* struts, as a function of the strut angle (right)

The results of the microscope inspections have also been used to study the distribution of the pore size, by recurring to the statistics of the extremes, applied to the square root of the area of the pores [143]. A peak-over-threshold approach [144] has been used, to cut the data below a threshold of $\sqrt{area} = 25$ μm and the Matlab® statistic tool has been used to compare different statistical distributions. The results of the Largest Extreme Value Distribution (LEVD) applied to $log_{10}\sqrt{area}$ have been reported in Fig.8.11, for both *Ref* and *Opt* struts having different orientations, up to 30°; strut angles above this value did not show a significant number of large pores. The LEVD distribution well fitted the results, resulting in a correlation factor R^2 greater than 0.94 in all the struts.

Increasing the strut angle, a decrease of the LEVD curves can be noted, i.e. less pores have been detected. Again, *Opt* struts performed better in respect to the *Ref* ones, being the curves lower and shifted to the left, i.e. having fewer large pores. A more detailed characterization of the internal porosity could be conducted by Computer Tomography, in order to inspect the entire volume of the specimens and to assess the three dimensional shape of the pores [22].
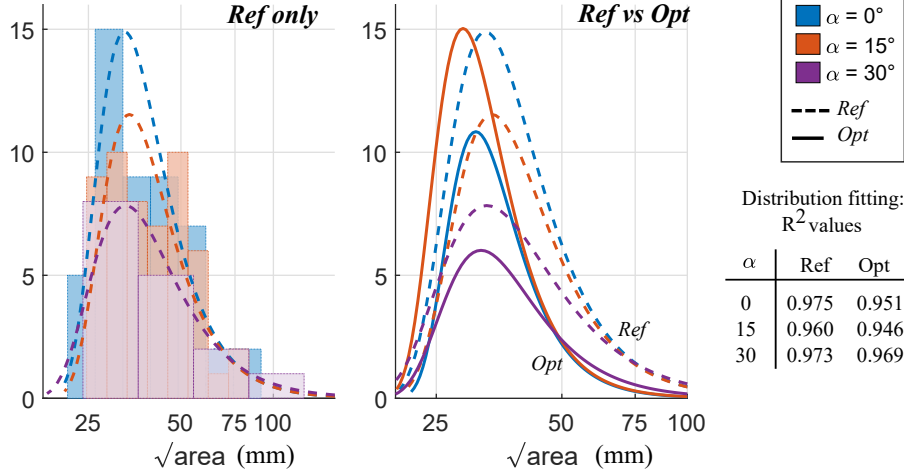
Figure 8.14: Pore size distribution - LEVD fitting

8.6   Compression testing

Finally, lattice structure specimens have been designed, fabricated and tested under compression loading, as an initial stage of the characterization of the mechanical properties of this kind of structures. Further experimental activities will be necessary to fully investigate the mechanical properties, considering different mechanical loadings, including fatigue.

The octet-truss unit cell has been chosen, based on its good structural performance and high isotropy level, that has made this type of lattice structures widely studied by researchers [131, 127, 145]. Specimens have been designed in order to obtain a repetition of 5 unit cells in each spatial direction, limiting the influence of the edge effects. Two geometries have been considered, having the same topology but different sizes: *Large* specimens are characterized by a strut diameter of d_n=1mm and a length of the cubic cell edge of v=6mm, while *Small* specimens are characterized by a strut diameter of d_n=0.8 mm and a length of the cubic cell edge of v=5mm. The cell size and strut diameter have been chosen so that both the geometries are characterized by similar Relative Density (RD), defined as:

$$\texttt{RD} = \frac{m^{exp}}{\rho v^3} \tag{8.1}$$

where m is the mass of the specimens, experimentally measured, and ρ is the density of the bulk material. The specimens have been fabricated in AlSi10Mg, using the EOS® M290 machine and the *Opt* process settings. After fabrication, Stress Relieving (`SR`) has been performed to all the samples, while only some of them have also been subjected to Hot Isostatic Pressing (`HIP`) and T6-like heat treatment. Quasi-static compression tests have finally been performed using an an Instron 5960 Series in displacement control, monitoring force (F) and vertical displacement (δ). To uniform the results derived from the two different geometries, equivalent stress and strain have been calculated as follow:

$$\begin{aligned} \sigma^* &= \frac{F_{exp}}{v^2} \\ \epsilon^* &= \frac{u}{v} \end{aligned} \tag{8.2}$$

where F_{exp} and u are the force and the displacement experimentally measured. Equivalent stress - strain curves have finally been plotted, as shown in Fig.8.15.
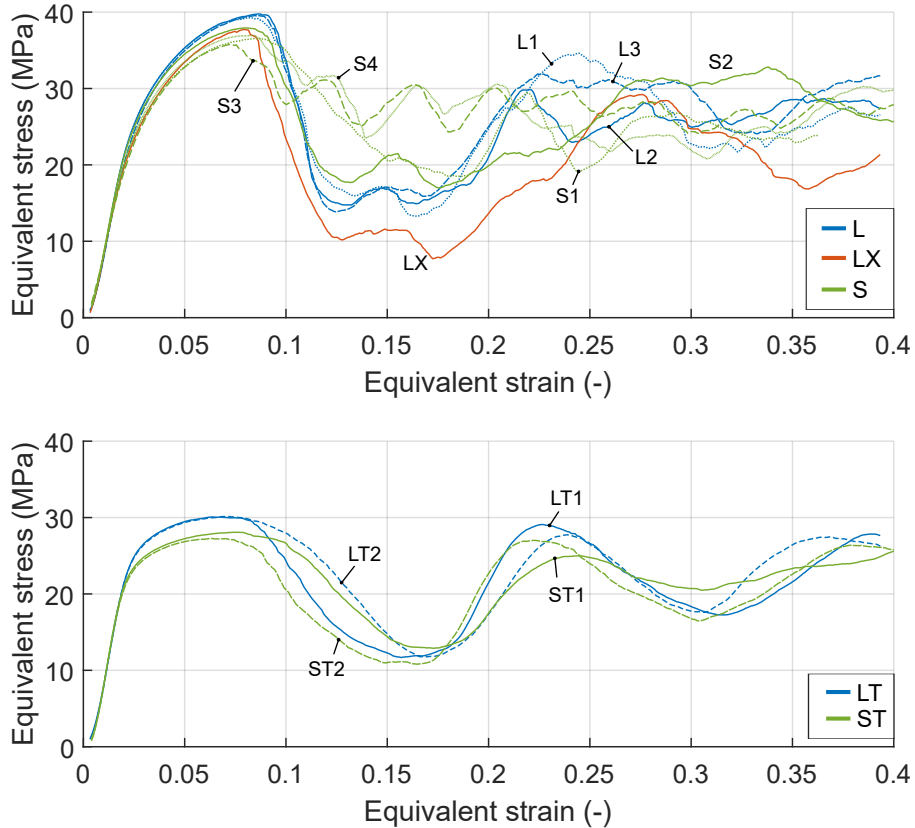
Figure 8.15: Compression testing: equivalent stress and strain curves

122

The equivalent Young's modulus (E^*) has been evaluated as the slope of the equivalent stress - strain curve in the first, linear region. Table 8.1 reports the list of the specimens, together with their characteristics and the main results.

Table 8.1: Compression tests: results. σ^*_{max} is the maximum equivalent stress, and E^* in the equivalent elastic modulus

Heat treatment	Unit cell size	ID	Testing direction	σ^*_{max} (MPa)	E^* (MPa)
SR	*Large*	L1	z	39.3	1388
		L2	z	39.8	1389
		L3	z	39.5	1299
		LX	x	37.7	1316
	Small	S1	z	36.5	1321
		S2	z	37.9	1410
		S3	z	35.8	1247
		S4	z	36.9	1277
SR+HIP+HT	*Large*	LT1	z	30.1	1383
		LT2	z	30.1	1449
	Small	ST1	z	28.1	1533
		ST2	z	27.7	1512

Fig.8.16 links the equivalent stress - strain curves to the relative frames obtained from video recording, regarding two of the samples L1 and S4. Some typical regions can be observed in all test, as also visible in the first plot of Fig.8.15.
Firstly, the load increases linearly with the displacement and an equivalent Young's modulus can be easily calculated.
Starting approximately from $\epsilon^* = 0.02$, the behavior is non-linear, until reaching a peak, where the equivalent stress is maximum (σ^*_{max}), after which shear bands develop, or an entire layer of lattice cells collapse, as shown by the second frames of Fig.8.16 and by Fig.8.17.
Then, the curves are characterized by a number of peaks and valleys, due to local failures, until a plateau region in observed. Finally, the load increases in a sort of densification stage. Similar trends have been observed in the literature[145, 127].

In particular, a very repeatable behavior has been observed in the SR *Large* specimens (blue curves in Fig.8.15). The stress - strain curves of the LX specimen, which was tested perpendicularly to the fabrication direction, resulted systematically lower the the equivalent samples tested along the building direction. This was not expected, as the octet truss unit cell has a cubic symmetry. However, the grade

Figure 8.16: Compression testing: most relevant frames of tests L1 and S4

Figure 8.17: Failure modes: shear bands and layer collapse

of anisotropy can be related to the anisotropy intrinsically related to the direction-ality of `AM` process, and above all, to the different distribution of the defects. In fact, as shown from the experimental activitie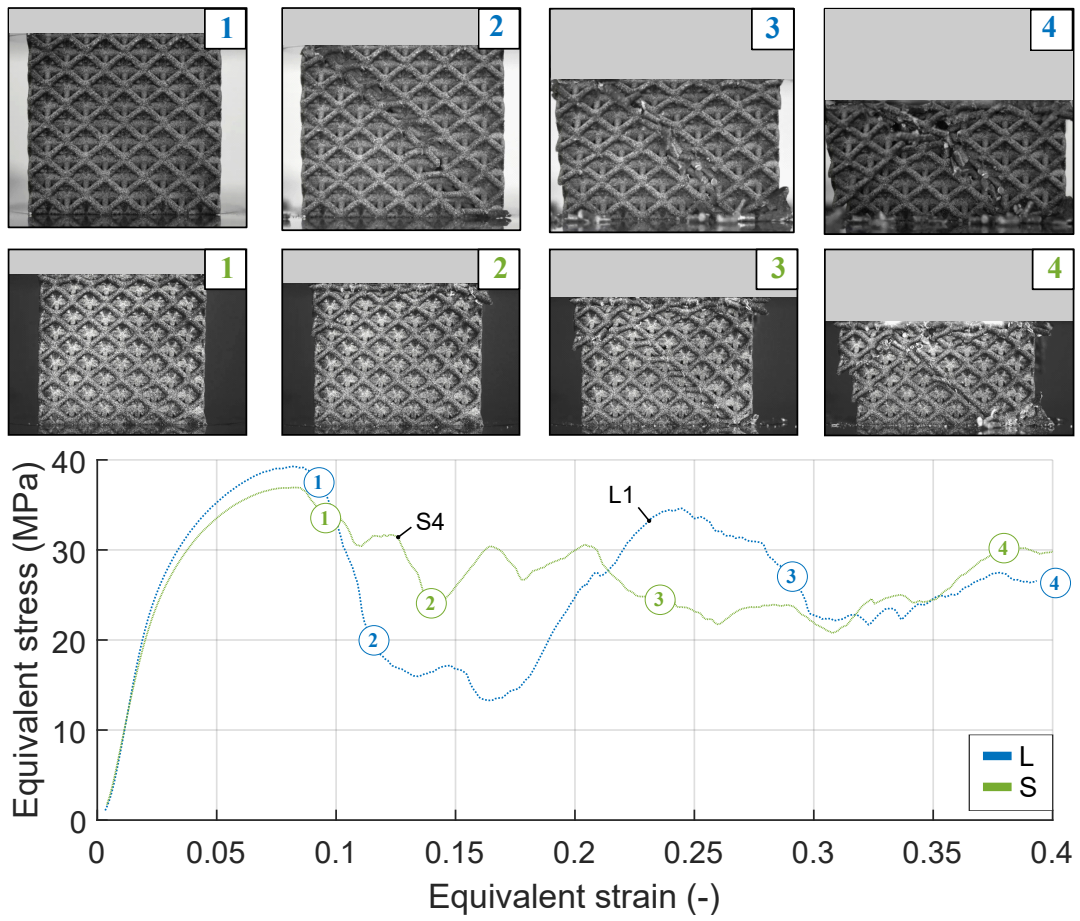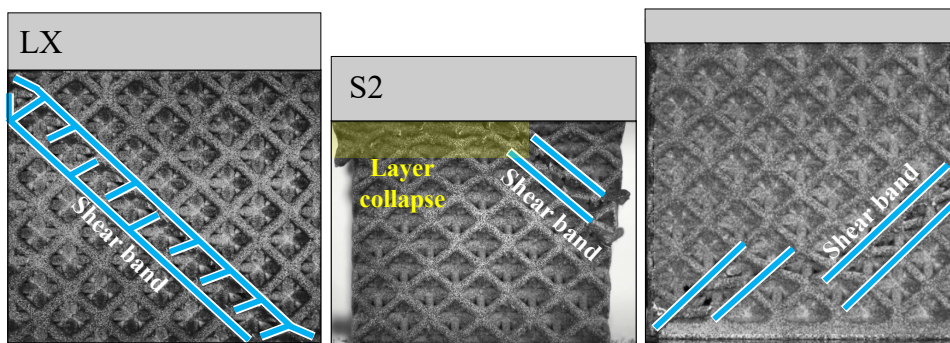s performed on the spider-web specimens, deviations from the nominal shape and internal defects are strongly influenced by the orientation of the struts in respect to the building direction.

Heat treatment strongly influenced the mechanical behavior of the specimens, as shown in the second plot of Fig.8.15, which reports the equivalent stress - strain curves of the specimens undergone to `SR`, `HIP` and T6-like treatment. The curves are smoother in respect to the `SR`-only specimens, and lower maximum stress values have been reached, as the heat treatment typically decreases the tensile strength of AlSi10Mg approximately by 25-30%[146, 17], improving the elongation at break.

8.7   Lessons learned

The experimental activities described in this chapter helped in assessing the capabilities and the limitations of `L-PBF` in fabricating small struts, which was essential for designing the lattice infill of the evaporator.

A methodology for quality control has been proposed, including a first step with robust bridge-like specimens for qualitative comparisons, and a second step with spider-web specimens, for the characterization of geometric imperfections and internal defects. In particular, the spider-web geometry has been found to be effective for investigating multiple strut orientations in a single specimen, providing also good accessibility for the 3D scanning.
The `GD&T`, based on the definition of best fit, maximum and minimum material cylinders, together with the cylindricity and run-out error, provided an effective tool for evaluating the deviations from the nominal geometry, such as over-sizing, under-sizing, irregular cross-sections and waviness.

The quality of strut has been found to be strongly dependent on the strut orientation in respect to the building direction, being the horizontal struts prone to be affected by internal pores and large deviations form the nominal shape. Hence, in the case of unsupported overhangs, the struts directly lay on the raw powder, that is characterized by thermal properties different from the solid material, resulting in imperfect melting and solidification [134, 135].
It must be noted that significant quality improvements have generally been observed for strut angles above 45°, above which imperfections are almost constant.

The proposed quality control procedure has been used for comparing specimens

fabricated with different process parameters, helping during the development of the optimal process settings, which have finally been used for fabricating lattice structure samples based on octet-truss unit cells. Quasi-static compression tests have finally been performed, as a preliminary step for the characterization of the lattice structural performance.

Chapter 9

Design of the new evaporator

The experimental activities performed in the previous task allowed to gain some experience about fabricating small struts, understanding the main capabilities and limitations of the manufacturing process. In this chapter, the structural behavior of the evaporator will be investigated, assessing the influence of the main design variables on the mechanical performances. The number of struts, together with their diameter and the skin thickness of the casing have been varied, monitoring the deformations and the stress state of the evaporator, obtained by Finite Element Analysis.

Based on the results of thermo-mechanical simulations, together with the lessons learned about the manufacturing limitations, a concept for a new evaporator will be finally proposed and compared to the previous generations. The research was carried out in a collaboration framework between NASA Jet Propulsion Laboratory, Politecnico di Torino and University of California at Los Angeles (UCLA) [39].

9.1 Sensitivity analysis

The baseline of the evaporator for the `2PMPFL` testbed developed at the Jet Propulsion Laboratory is a 200 mm by 200 mm square vessel made of `L-PBF` AlSi10Mg, composed by a full-solid casing and a porous wick, co-printed as a monolithic component. A scheme of the evaporator is given in Fig.9.1, together with a cutaway showpiece of the current version.
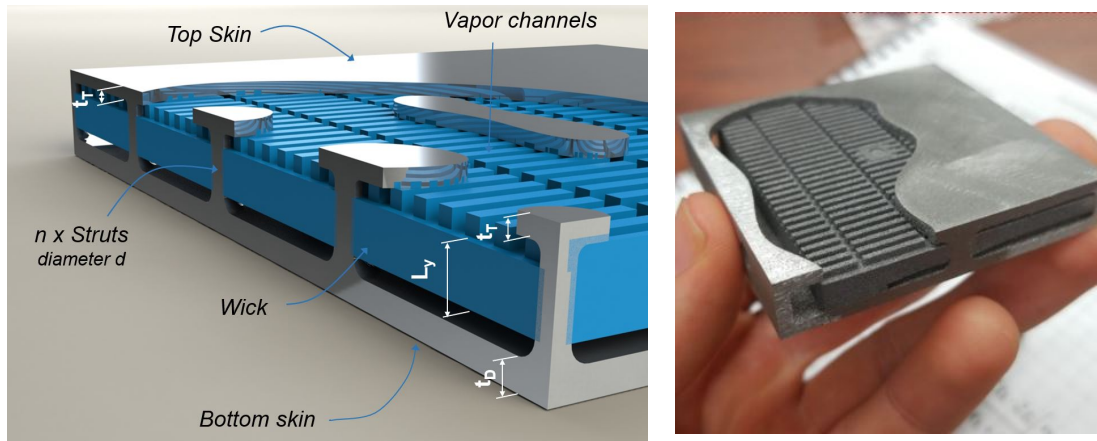
Figure 9.1: Schematic of the main design variables of the evaporator (left), Showpiece of Evaporator 4 (right)

From a mechanical point of view, the evaporator is a vessel subjected to internal pressure loading. It shall operate in the testbed described in Chapter 7, using ammonia as working fluid. In the nominal operational conditions, the pressure of the system is set at 10 bar, corresponding to an evaporation temperature of 25°C; however, in this early design stage, the maximum design pressure has been considered as 17.2 bar, value to which the relief valve of the testbed is set, in case of malfunctioning. As reported in Fig.9.1, the main design variables are the thickness of the casing (t), the number of the internal struts (n), their diameter (d), and the height of the porous wick (L_y).

When designing the evaporator, both thermal and structural aspects shall be taken into account, as structurally optimized configurations may result in poor thermal performance, and thermally optimized configurations may lead to heavy components. For instance, the thickness of the casing shall be reduced as much as possible, to reduce the thermal resistance between the vapor chamber of the evaporator and the electronics on the plate, maximizing the heat flux. On the other side, the evaporator needs to withstand the internal pressure of the fluid and shell of the casing shall be designed to provide an adequate margin of safety. This work has

been mainly focused on assessing the structural behavior of the evaporator, while thermal models and analysis have been provided by Valdarno et al. in [147, 39] and will be further discussed in future works.

First, a sensitivity analysis has been performed, to investigate the influence of the main geometric parameters on the structural behavior of the evaporator.
A simplified numerical model has been developed using Altair Hypermesh® as pre-processor, and Altair OptiStruct® as solver. In this preliminary stage, the influence of the wick on the structural performance has been neglected. Two-dimensional quadrangular elements (CQUAD4) have been used to model the casing and one-dimensional bar elements (CBAR) have been used for the struts. As the evaporator lies on the testbed on polymeric supports, the simply-supported case has been considered and symmetric boundary conditions around the three directions have been applied. Uniform internal pressure loading has been applied on the shell elements (PLOAD4). A homogeneous isotropic material model (MAT1) has been considered, considering the material properties derived from previous experimental activities performed on specimens, being the Young's modulus 70 000 MPa, the Poisson's ratio 0.33, and Yield and Ultimate strength 232 MPa and 379 MPa respectively. Even if L-PBF is a typical directional process, a low grade of anisotropy was detected on the specimens and, for seek of simplicity, the isotropic model has been adopted. Finally, linear static analysis have been run.

The influence of the strut number and the strut size on the structural behavior has been firstly assessed, by monitoring the stress state obtained by the Finite Element Analysis.
Due to the geometry of the component and the uniform pressure acting on the casing shell, to which the struts are connected, most of the internal struts are expected to work mainly in tension, so that it has been decided to monitor the structural behavior as a function of the cumulative cross sectional area of the all struts, which includes the information about both the strut number and diameter. Hence, the non dimensional variable δ has been defined as follow:

$$\delta = \frac{nA_{strut}}{A_{evap}} = \frac{n\pi d^2/4}{l^2} \tag{9.1}$$

where n is the strut number, d is the strut diameter, and L is the length of the evaporator. The maximum Von Mises stress on the shall and on the struts has been finally plotted as a function of δ in Fig. 9.2, for a number of struts of 64, 144, and 256 and a strut diameter ranging from 0.75 mm to 3 mm. Marker size and color have been used to highlight different cases, having different number of struts and strut size.

Considering a fixed number of struts n, low values of δ correspond to thin struts,
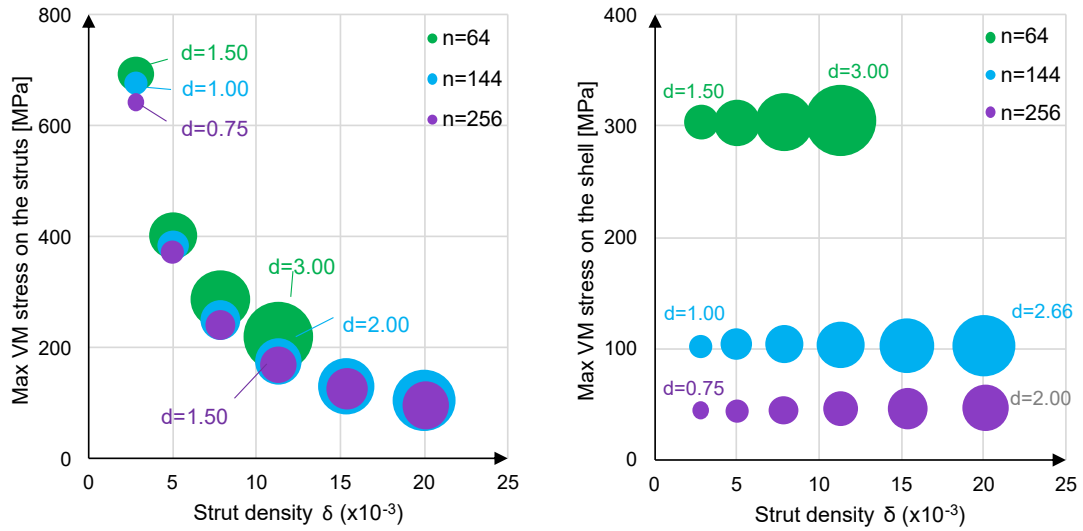
Figure 9.2: Maximum Von Mises stresses on the struts and on the shell, as a function of the geometric parameter δ

high values of δ to thicker struts. As expected, it is possible to limit the maximum stress on the struts by increasing the diameter of the struts. A small effect of the strut diameter on the maximum stress has been observed.

By varying both strut number and strut diameter, it is possible to observe that the maximum stress values on the struts collapse on one single curve, function of $1/\delta$. Therefore, in order to control the stress state on the struts, two strategies are possible, increasing the number of struts, or increasing the strut diameter. The first option is preferable, as an increased number of struts results in lower maximum stresses on the shell as well. In fact, reducing the spacing between the struts, it is possible to obtain a more uniform deformation of the shell, limiting the maximum stresses. It must be noticed that, even if the mass of the struts is very small, acting of the strut design may result in significant mass savings, as they strongly influence the overall stress state, eventually making possible reductions of the shell thickness.

A second set of analyses has been performed by fixing the number of struts n, and letting the thickness of the casing varying between 1.2 mm to 2.0 mm, as shown in Fig. 9.3. To provide further information, three cases have been analyzed, with a strut diameter of 2.00 mm, 2.33 mm, and 2.00 mm. As expected, the thickness of the casing shell directly affects the maximum stress on the shell itself. As shown in the previous plots, the influence of the strut diameter on the maximum shell stress is negligible. The maximum stress in the struts is affected by both the strut diameter and the shell thickness as well, so that increasing the shell thickness it it

130

possible to limit both the maximum stress on the struts and on the shell. Oblivi-
ously, increments of the shell thickness results in significant increments of the total
mass of the evaporator.
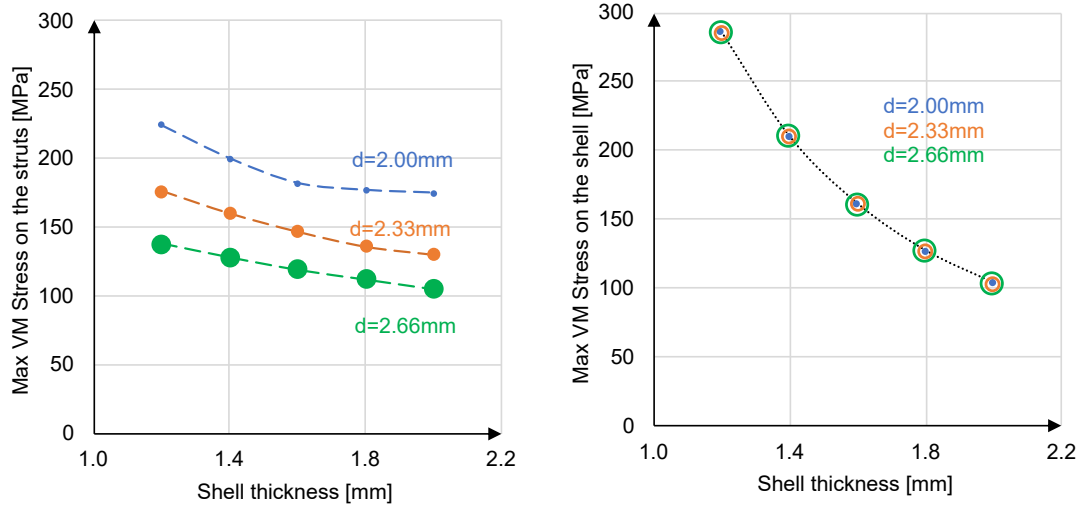
Figure 9.3: Maximum Von Mises stresses on the struts and on the shell, as a
function of the shell thickness

The influence of the wick height has finally been assessed by recurring to the
three dimensional element model that will be presented in the following section, in
which both the casing and the wick are modeled. In this model, the thickness of the
to and bottom surface are different, being respectively 1.00 mm and 1.66 mm. The
maximum Von Mises stress on the casing surfaces has been plotted in Fig. 9.4, for
three values of wick height. Being the wick connected to the top surface only, the
wick height affects mainly the stress on that surface, providing additional stiffness.

Thermal analyses have been performed by Valdarno et al.[147, 39], to assess the
influence of the design parameters on the thermal performance of the evaporator.
They found that the shell thickness has a limited effect on the transmission of heat
through the wick, but it can affect the maximum temperature on the surface of
the casing; therefore, reducing the thickness of the top skin can be beneficial to
better control the temperature of the payload. Wick height strongly affects the
evaporative heat load, so that short wicks allows to reduce the overall mass, but
they are not optimal from a thermal point of view, as more heat is transferred to
the liquid chamber and not absorbed by evaporation. Struts were found to affect
the heat transfer and temperature as well, but their influence was limited to the
area next to the strut themselves.

131
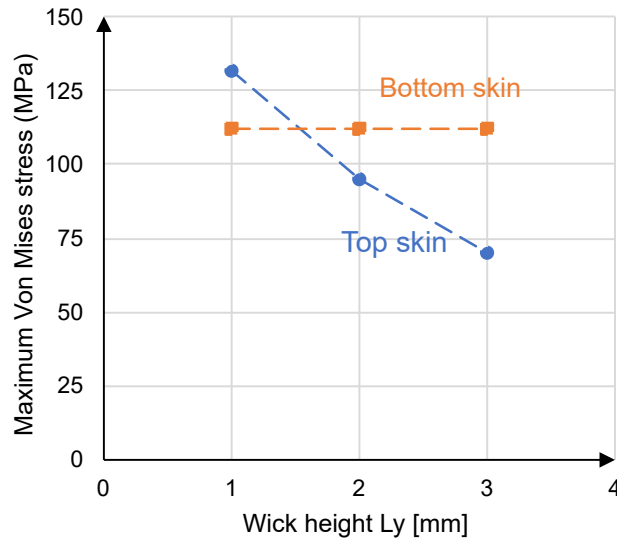
Figure 9.4: Maximum Von Mises stresses on the struts and on the shell, as a function of the wick height

The sensitivity analysis provided a preliminary map of the structural behavior of the evaporator as a function of the main design variables.

9.2   Evaporator 5

The trade-off analyses previously performed with the simplified model were used as guidelines for proposing a new optimized geometry of the evaporator. The baseline was represented by Evaporator 4, that was successfully fabricated and tested. Its geometry was characterized by a 2.2 mm thick casing, reinforced by an array of 25 struts, equally spaced and with a diameter of 3.6 mm. During the structural design process of generation 4, the contribution of the wick to the overall structural behavior of the evaporator was conservatively not taken into account, due to the lack of data about the mechanical properties of `L-PBF` porous AlSi10Mg. In addition, unknowns about manufacturing limitations lead to the adoption of relatively thick struts, to avoid possible failure during the fabrication process.

The experimental activities performed on small struts described in the previous chapter shown it is possible to fabricated good quality struts with smaller diameters. Moreover, `JPL` researchers conducted experimental tests on porous AlSi10Mg, to better characterize not only the thermal properties, but also the mechanical ones, such as Young's modulus, Yield and Ultimate Strength and elongation at break, as a function of the porosity. These activities allowed to incorporate also the wick

within the structural model of the evaporator.

A new Finite Element model has been created (Fig.9.5, second row), using solid elements (CHEXA) to model both the casing and the porous wick. A total number of approximately 390 000 nodes has been used to model a quarter of the evaporator, and symmetric boundary conditions have been applied. The internal pressure loading has been set at 17.2 bar, according to the maximum pressure allowed by the relief valve of the test bed. Isotropic homogeneous material models have been for both the full-solid and porous media, as summarized in Table 9.1, together with the material allowable.
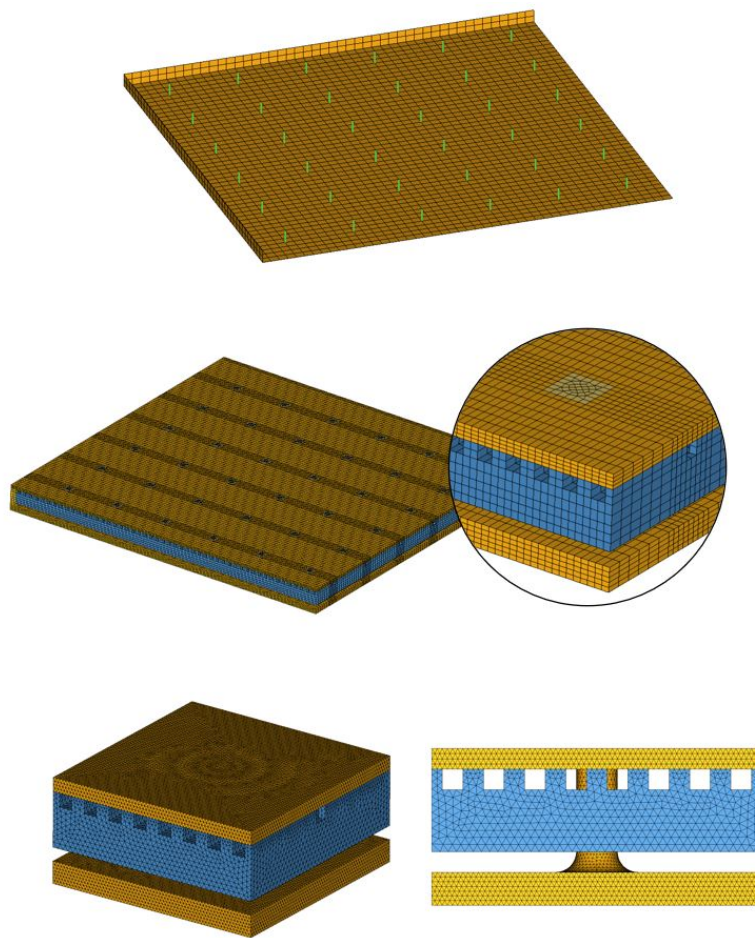

Figure 9.5: `FE` models: simplified shell model for the sensitivity analysis, not including the porous wick (first row), solid model (second row), and sub-model (third row)

A minimum safety factor of 1.4 in respect to yielding has been required. Goal of

Table 9.1: Material properties

Material	Density (kg/m³)	Young's Modulus (GPa)	Poisson's ratio -	Yield tensile strength (MPa)	Ultimate tensile strength (MPa)
Full solid	2670	70	0.33	232	379
Porous media	2029	6.2	0.33	47	60

the optimization process is to minimize the mass of the evaporator. As a reference, the mass breakdown of Evaporator 4 is shown in Fig. 9.6 , as a pie chart. About
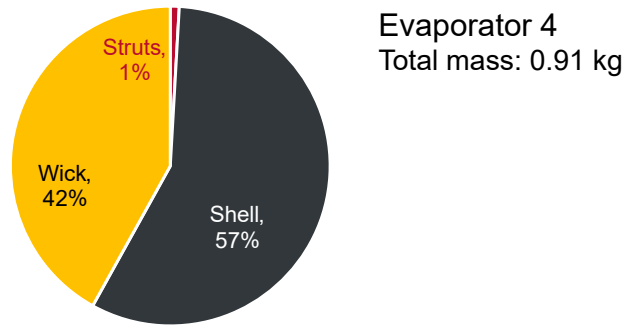
Figure 9.6: Mass breakdown of Evaporator 4

99% of the total mass is represented by the wick and the shell of the casing, while the struts make up only 1% of the mass. Therefore, a small reduction of the shell thickness, even if backed up by a large increment of size number and diameter, may lead to great mass savings. Hence, in respect to Evaporator 4, a significantly higher number of struts has been used, passing from 36 to 144. This allowed to reduce the skin thickness, according to the trend shown in Fig.9.3, and to reduce the strut diameter as well. The reduction of the strut diameter might also lead to improved thermal performances, as they can better fit in the space between the vapor groves, without blocking the continuous vapor flow, as shown in Fig.9.7. Even if the experimental activities on lattice manufacturing showed that struts diameters of 1 mm, or even smaller are possible to be fabricated, it was decided to limit the minimum strut diameter to 1.5 mm.

In addition, to further increase the mass savings and to achieve a thinner form factor of the evaporator, the wick height has been reduced as well, from 4 mm to 3 mm.

Several design iterations have been performed, to lighten the structure and to minimize the thickness of the top surface as well, in order to reduce the thermal resistance between the heater and the vapor chamber. To this aim, it has been decided to use different thicknesses for the top and the bottom surfaces. In fact,
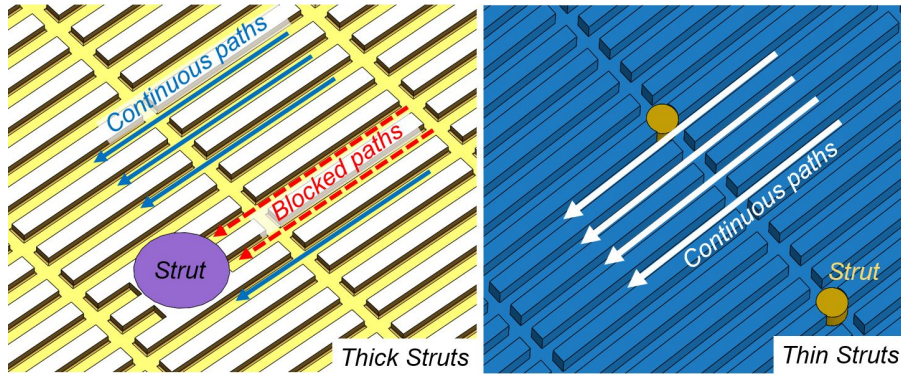
Figure 9.7: Effects of thick (left) and thin (right) struts on the vapor flow

the wick is directly connected to the top surface only, providing additional bending stiffness to that region. The main geometric parameters of the optimized evaporator have finally been listed in the following table.

Table 9.2: Geometric parameters of the optimized configuration

Parameter		Value	
Top skin thickness	tT	1.0	mm
Bottom skin thickness	tB	1.6	mm
Number of struts	n	144	-
Strut diameter	d	2.0	mm
Wick height	Ly	3.0	mm
Wick pillar height	Lyp	1.0	mm

A further investigation of the local stress state has been performed by recurring to a sub-model representing a single cell of the evaporator (Fig.9.5, third row). A more detailed geometry including the fillets between the struts and the casing, has been meshed with the 2nd order tetrahedral elements, using a total number of nodes of approximately 428 000. Symmetric boundary conditions, together with the displacements derived from the previous model have been imposed. Linear static analysis has been performed.

The results of the sub-model have been found in agreement with the full-model, as shown in Fig. 9.8. The refined mesh allowed to better investigate the stress distribution within the shell and at the interfaces. A localized stress peak has been observed at the base of the strut and at the intersection between the full-solid strut and the porous wick.
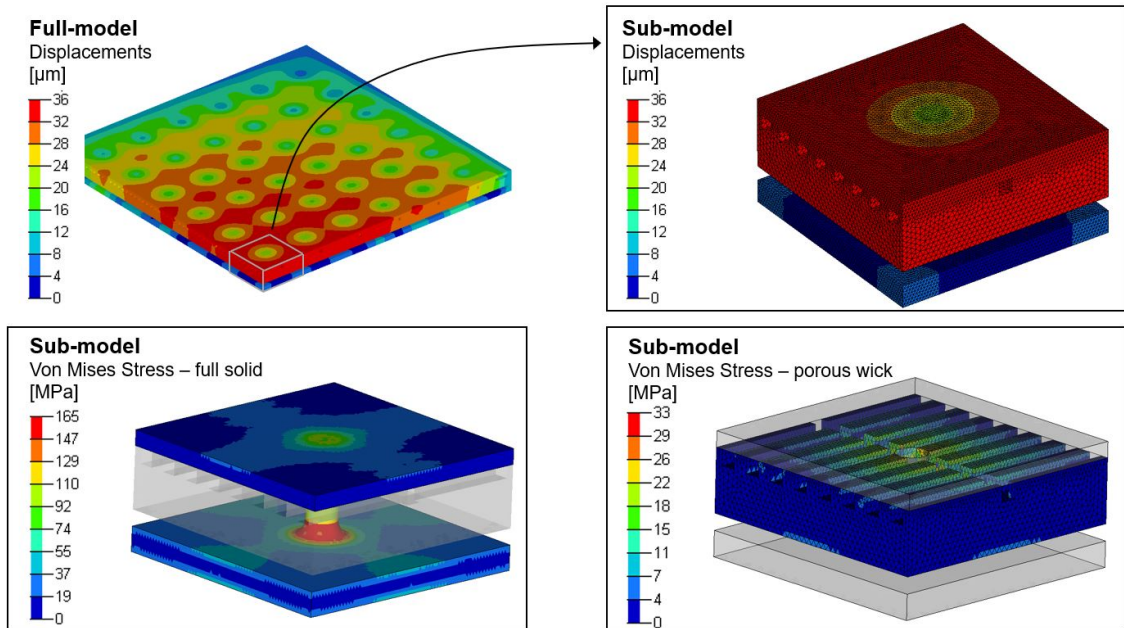
Figure 9.8: Stress analysis: full and sub-model

The new configuration resulted in mass savings higher than 30%. A comparison between the layout of Evaporator 5 and the previous generations is given in Fig.9.9.

Further activities should be performed, aimed to characterize the strength of the interfaces between solid and porous material and to assess the fatigue performance, considering also the typical imperfections related the manufacturing process.
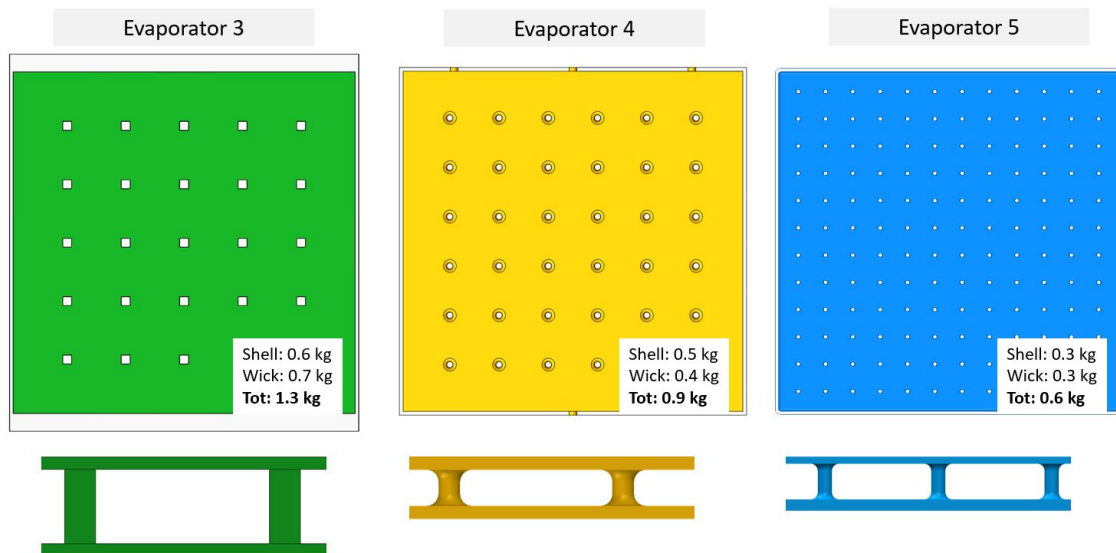
Figure 9.9: Comparison between generation 3, 4 and 5 - top view and cross section

9.3   Conclusion

Thermal management is one of the fundamental tasks of spacecraft, especially in the case of porbes for the exploration of harsh environments, characterized by extreme temperatures. Novel thermal control systems are currently under study, leveraging also the new fabrication technologies. In this frame, JPL is developing an innovative evaporator for two-phase thermal control systems, to be fabricated by Additive Manufacturing. AM could provide a game changing technology, as it allows to tune the material properties of the wick by varying the process parameters, to fabricate the full-solid casing together with the porous wick as a single monolithic component, and to obtain complex geometries, such as conformal shapes and spherical shells.

In this chapter, an innovative evaporator for laboratory testing has been proposed, based on the thermal and structural design activities performed during a collaboration between JPL, UCLA and Politecnico di Torino [39]. The activities of the PhD candidate focused on the latter.

A preliminary sensitivity analysis has been performed to assess the influence of the main design parameters on the structural behavior of the system. Based on the input of structural and thermal simulations, a design of an optimized evaporator has been proposed, resulting in significant mass reduction and a more compact shape, if compared to the previous generations.
Unfortunately, Covid-19 restrictions limited and delayed the planned experimental activities. Future development will need to consider a detailed characterization of full-solid and porous materials, in both static and fatigue conditions, considering also the detrimental effects of manufacturing imperfections. Specimen-level testing will also be necessary to assess the solid-to porous and strut-to-shell interfaces. The validation of thermal and structural models will be performed at component level, before evaluating the thermal performance at the system level, by integrating the evaporator in the test-bed.

Chapter 10

Conclusion

This work focused on the design of a novel lightweight shell for space probes for the exploration of harsh environments. The extreme environmental conditions that can be found, for instance, in the Europa's internal ocean, or on the surface of Venus, pose unique challenges for landers and probes, due to the simultaneous presence of very high external pressure loading and extreme temperatures. New technologies, such as Additive Manufacturing, could open unprecedented opportunities as they significantly extended the design freedom, enabling the fabrication of very complex geometries, like complex stiffening systems, or integrated thermostructural systems, made possible by the co-fabrication of full-solid and porous materials within the same product. Design procedures shall be updated accordingly, to fully exploit the potential of these new technologies.

The research activity started with the design case of a melt-probe for the exploration of Europa's ocean, which provided a testing ground for assessing the typical issues related to the design of structures for probes for harsh environments and for investigating the potential benefits related to the adoption of AM techniques.

The object of this dissertation has been provided by a research and technology development activity, regarding a concept for a Venus lander, in which the primary structure consists in a `AM` metallic spherical shell, stiffened by a system of internal ribs and potentially integrating a thermal control system within the shell itself. The PhD activity focused on the design of an `AM` structural shell reinforced by an isogrid stiffening layout, which could be difficult and expensive to be fabricated by conventional manufacturing techniques. Analytical and numerical approaches for the early design stage were investigated, for both shells without internal ribbing, and isogrid-stiffened shell, proposing a methodology for the optimization of the isogrid layout, based on analytical formulations.

For a better understanding of the behavior of AM spherical shells undergoing external pressure loading, and validating the optimization methodology, an experimental campaign was performed. Sub-scale components were designed accordingly, and fabricated by Laser-Powder Bed Fusion. Numerical predictions, simulating the test conditions, were performed and finally hydrostatic and relative environment tests were performed. During hydrostatic test, both plain and spherical shells were tested by increasing the external pressure up to failure.

The behavior of the plain shell was found to be in agreement with the literature data about conventional manufacturing techniques, showing that `AM` can be a suitable manufacturing process for this kind of application. The isogrid-reinforced shells provided repeatable results in terms of failure pressure and failure mode, with a low mismatch with the numerical predictions. By analyzing the buckling knockdown factor experimentally derived, isogrid shells were less sensitive to imperfections, if compared to plain shells.

The lessons learned from the experimental campaign were used during the design synthesis, in which the full-scale design was updated and a production analysis was performed. AM isogrid spherical shells were found to provide not only mass reduction, but also cost and schedule savings, if compared to conventional manufacturing techniques. Finally, a manufacturing demonstrator of an isogrid spherical shell integrating an evaporator porous wick was fabricated, proving the possibility to co-fabricate integrated thermal control systems, as a monolithic component.

For a better understanding of the `AM` evaporator, an overview on two-phase thermal control systems was given, focusing on a Two Phase Mechanical Pumped Fluid Loop system, a promising technology currently under development at `NASA JPL`. The activity focused on the design of a prototype of an AM evaporator for laboratory testing, in order to optimize the structure, by recurring to a lattice infill. As a first step of the optimization process, some experimental activities were performed on specimens, aimed at assessing the main `AM` limitations, especially when fabricating small struts. A methodology for the assessment of geometry imperfections and internal defects was proposed and two sets of process parameters were compared. The experimental activities allowed to get a better understanding of the manufacturing limitations, necessary for the design of the evaporator.

The mechanical behavior of the `AM` evaporator was explored, investigating the effects of the main geometric parameters on the structural performance. A novel optimized layout was proposed, showing a significant mass reduction, together with a more compact shape factor. Unfortunately, Covid-19 restrictions limited and delayed the planned activities, which would include experimental activities on specimens for better material characterization, and finally the fabrication and testing of the evaporator.

Through this dissertation, potential benefits of Additive Manufacturing were explored, and design methodologies were investigated, including analytical and numerical methods aimed at providing tools for the early design stages. The application, being space probes for the exploration of harsh environments, together with the collaboration with the Jet Propulsion Laboratory, provided a unique opportunity to address challenging problems, where systems are subjected not only to very high mechanical loadings, but also to multi-physical phenomena.

Acronyms and Symbols

Acronym		Meaning
2PMPFL	-	Two-Phase Mechanical Pumped Fluid Loop
AM	-	Additive Manufacturing
BF	-	Best Fit
CAD	-	Computer Aided Design
CT	-	Computed Tomography
EBM	-	Electron Beam Melting
ESA	-	European Space Agency
FEA	-	Finite Element Analysis
GD&T	-	Geometric Dimensioning and Tolerancing
GI	-	General Instability
HIP	-	Hot Isostatic Pressing
HP	-	Heat Pipe
JPL	-	Jet Propulsion Laboratory
KF	-	Knockdown Factor
LEVD	-	Largest Extreme Value Distribution
LFEA	-	Linear Finite Element Analysis
LM	-	Least Material
LoF	-	Lack of Fusion
L-PBF	-	Laser Powder Bed Fusion
MM	-	Maximum Material
MoS	-	Margin of Safety
NASA	-	National Aeronautics and Space Administration
NLFEA	-	Non Linear Finite Element Analysis
RC	-	Rib Crippling
SB	-	Skin Buckling
SF	-	Safety Factor
VM	-	Von Mises

Symbol		Meaning
α	-	Isogrid non dimensional parameter 1
β	-	Isogrid non dimensional parameter 2
γ	-	Correlation factor
δ	-	Isogrid non dimensional parameter 3
δ'	-	Strut density
ϵ	-	Strain
λ	-	Buckling load factor
ν	-	Poisson's Ratio
σ	-	Stress
σ_y	-	Yield strength
ρ	-	Density
A	-	Area
b	-	Rib thickness
c_0	-	Empirical parameter
d	-	Rib height, or strut diameter
D	-	Bending Stiffness
E	-	Young's modulus
F	-	Force
err	-	Error
h	-	Triangle height
h_{ring}	-	Ring height
I	-	Moment of inertia
k	-	Thermal conductivity
K	-	Extensional stiffness
KF	-	Knockdown Factor
l	-	Length
m	-	Mass
MoS	-	Margin of Safety
N	-	Load per unitary length
n	-	Number of struts
p	-	Pressure
p_{cr}	-	Buckling critical pressure
q	-	Heat flux
R	-	Radius
RD	-	Relative Density
SF	-	Safety Factor
t	-	Skin thickness
T	-	Temperature
u	-	Displacement
v	-	Length of the edge of the lattice cell

144

Subscript		Meaning
2D	-	Two-dimensional
3D	-	Three-dimensional
a	-	Axial
$analyt$	-	Analytical
$base$	-	Baseline
cl	-	Classical
cr	-	Critical
e	-	Equivalent
exp	-	Experimental
ext	-	External
FEA	-	Finite Element Analysis
GI	-	General Instability
h	-	Hoop
id	-	Ideal
LFEA	-	Linear Finite Element Analysis
n	-	Nominal
NL	-	Non Linear Finite Element Analysis
RC	-	Rib crippling
SB	-	Skin Buckling
r	-	Radial
x	-	Rectangular coordinate direction
y	-	Rectangular coordinate direction
θ	-	Polar direction
ϕ	-	Azimuthal direction

Bibliography

[1] Steven J Dick. "NASA and the search for life in the universe". In: *Endeavour* 30.2 (2006), pp. 71–75. DOI: 10.1016/j.endeavour.2006.02.005.

[2] Christopher P McKay. "Requirements and limits for life in the context of exoplanets". In: *Proceedings of the National Academy of Sciences* 111.35 (2014), pp. 12628–12633.

[3] Jonathan I. Lunine. "Ocean worlds exploration". In: *Acta Astronautica* 131.September 2016 (2017), pp. 123–130. DOI: 10.1016/j.actaastro.2016.11.017.

[4] Fredric W Taylor, Håkan Svedhem, and James W Head. "Venus: The atmosphere, climate, surface, interior and near-space environment of an Earth-like planet". In: *Space Science Reviews* 214.1 (2018), p. 35. DOI: 10.1007/s11214-018-0467-8.

[5] Jane S Greaves et al. "Phosphine gas in the cloud decks of Venus". In: *Nature Astronomy* (2020), pp. 1–10. DOI: 10.1038/s41550-020-1174-4.

[6] William Bains et al. "Phosphine on Venus Cannot be Explained by Conventional Processes". In: *arXiv preprint arXiv:2009.06499* (2020).

[7] VEXAG Roadmap Focus. *Roadmap for Venus Exploration.* Tech. rep. 2019.

[8] TIbo Balint, James Cutts, and Johnny H. Kwok. "Overview of Flagship Class Venus Mission Architectures". In: *6th International Planetary Probes Workshop.* Atlanta, Georgia, USA, 2006.

[9] *NASA SP-2007-6105 NASA Systems Engineering Handbook.* Tech. rep. 2007.

[10] Francesco Trevisan et al. "On the selective laser melting (SLM) of the AlSi10Mg alloy: Process, microstructure, and mechanical properties". In: *Materials* 10.1 (2017). DOI: 10.3390/ma10010076.

[11] *ISO/ASTM 52900: Additive manufacturing - General principles - Terminology.* Standard. 2015.

[12] Flaviana Calignano, Manuela Galati, and Luca Iuliano. "A metal powder bed fusion process in industry: Qualification considerations". In: *Machines* 7.4 (2019). DOI: 10.3390/machines7040072.

[13]   Dirk Herzog et al. "Additive manufacturing of metals". In: *Acta Materialia* 117 (2016), pp. 371–392. DOI: `10.1016/j.actamat.2016.07.019`.

[14]   Stéphane Gorsse et al. "Additive manufacturing of metals: a brief review of the characteristic microstructures and properties of steels, Ti-6Al-4V and high-entropy alloys". In: *Science and Technology of advanced MaTerialS* 18.1 (2017), pp. 584–610. DOI: `10.1080/14686996.2017.1361305`.

[15]   Abbas Razavykia et al. "An Overview of Additive Manufacturing Technologies—A Review to Technical Synthesis in Numerical Study of Selective Laser Melting". In: *Materials* 13.17 (2020), p. 3895. DOI: `10.3390/ma13173895`.

[16]   Diego Manfredi et al. "From powders to dense metal parts: Characterization of a commercial AlSiMg alloy processed through direct metal laser sintering". In: *Materials* 6.3 (2013), pp. 856–869. DOI: `10.3390/ma6030856`.

[17]   Luca Girelli et al. "Study of heat treatment parameters for additively manufactured AlSi10Mg in comparison with corresponding cast alloy". In: *Materials Science and Engineering: A* 739 (2019), pp. 317–328. ISSN: 0921-5093. DOI: `10.1016/j.msea.2018.10.026`.

[18]   Shunyu Liu and Yung C Shin. "Additive manufacturing of Ti6Al4V alloy: A review". In: *Materials & Design* 164 (2019), p. 107552. DOI: `10.1016/j.matdes.2018.107552`.

[19]   S. Romano et al. "Fatigue properties of AlSi10Mg obtained by additive manufacturing: Defect-based modelling and prediction of fatigue strength". In: *Engineering Fracture Mechanics* 187 (2018), pp. 165–189. DOI: `10.1016/j.engfracmech.2017.11.002`.

[20]   Joel C. Najmon, Sajjad Raeisi, and Andres Tovar. "Review of additive manufacturing technologies and applications in the aerospace industry". In: *Additive Manufacturing for the Aerospace Industry*. Ed. by Francis Froes and Rodney Boyer. Elsevier, 2019, pp. 7–31. DOI: `10.1016/B978-0-12-814062-8.00002-9`.

[21]   A. A. Shapiro et al. "Additive Manufacturing for Aerospace Flight Applications". In: *Journal of Spacecraft and Rockets* 53.5 (Sept. 2016), pp. 952–959. DOI: `10.2514/1.A33544`.

[22]   S. Romano et al. "Quality control of AlSi10Mg produced by SLM: Metallography versus CT scans for critical defect size assessment". In: *Additive Manufacturing* 28.May (Aug. 2019), pp. 394–405. DOI: `10.1016/j.addma.2019.05.017`.

[23]   Davoud Jafari and Wessel W Wits. "The utilization of selective laser melting technology on heat transfer devices for thermal energy conversion applications: A review". In: *Renewable and Sustainable Energy Reviews* 91 (2018), pp. 420–442. DOI: `10.1016/j.rser.2018.03.109`.

[24] GM Grover, TP Cotter, and GF Erickson. "Structures of very high thermal conductance". In: *Journal of Applied Physics* 35.6 (1964), pp. 1990–1991. DOI: 10.1063/1.1713792.

[25] Bengt Sundén and Juan Fu. "Chapter 7 - Heat Pipes for Aerospace Application". In: *Heat Transfer in Aerospace Applications.* Ed. by Bengt Sundén and Juan Fu. Academic Press, 2017, pp. 117–144. ISBN: 978-0-12-809760-1. DOI: https://doi.org/10.1016/B978-0-12-809760-1.00007-7.

[26] José Meseguer, Isabel Pérez-Grande, and Angel Sanz-Andrés. "11 - Heat pipes". In: *Spacecraft Thermal Control.* Ed. by José Meseguer, Isabel Pérez-Grande, and Angel Sanz-Andrés. Woodhead Publishing, 2012, pp. 175–207. DOI: https://doi.org/10.1533/9780857096081.175.

[27] Gajanana C. Birur, Georg Siebes, and Theodore D. Swanson. "Spacecraft Thermal Control". In: *Encyclopedia of Physical Science and Technology (Third Edition).* Ed. by Robert A. Meyers. Third Edition. New York: Academic Press, 2003, pp. 485–505. DOI: 10.1016/B0-12-227410-5/00900-5.

[28] Derek W Hengeveld et al. "Review of modern spacecraft thermal control technologies". In: *HVAC&R Research* 16.2 (2010), pp. 189–220. DOI: 10.1080/10789669.2010.10390900.

[29] C Figus et al. "Capillary fluid loop developments in Astrium". In: *Applied thermal engineering* 23.9 (2003), pp. 1085–1098. DOI: 10.1016/S1359-4311(03)00038-3.

[30] Masoud Ameli et al. "A novel method for manufacturing sintered aluminium heat pipes (SAHP)". In: *Applied Thermal Engineering* 52.2 (2013), pp. 498–504. DOI: 10.1016/j.applthermaleng.2012.12.011.

[31] Davoud Jafari, Wessel W Wits, and Bernard J Geurts. "Phase change heat transfer characteristics of an additively manufactured wick for heat pipe applications". In: *Applied thermal engineering* 168 (2020), p. 114890. DOI: 10.1016/j.applthermaleng.2019.114890.

[32] JR McDonough. "A perspective on the current and future roles of additive manufacturing in process engineering, with an emphasis on heat transfer". In: *Thermal Science and Engineering Progress* 19 (2020), p. 100594. DOI: 10.1016/j.tsep.2020.100594.

[33] Benjamin Furst et al. "A Comparison of System Architectures for a Mechanically Pumped Two-Phase Thermal Control System". In: *47th International Conference on Environmental Systems.* July. Charleston, South Carolina, 2017, p. 20.

[34] Benjamin I Furst et al. "An Additively Manufactured Evaporator with Integrated Porous Structures for Two-Phase Thermal Control". In: *48th International Conference on Environmental Systems*. July. Albuquerque, New Mexico, 2018.

[35] Takuro Daimaru et al. "Development of an Evaporator Using Porous Wick Structure for a Two-Phase Mechanically Pumped Fluid Loop". In: *49th International Conference on Environmental Systems*. July. 2019.

[36] Benjamin Furst, Ratnakumar Bugga, and Scott Roberts. "A Concept Demonstrator for an Additively Manufactured Li-ion Battery Case with Embedded Heat Pipes". In: *50th International Conference on Environmental Systems*. 2020.

[37] Enrico Ossola et al. "Design of Isogrid Shells for Venus Surface Probes". In: *Journal of Spacecraft and Rockets* Published online (2020). DOI: 10.2514/1.A34823.

[38] Enrico Ossola, Eugenio Brusa, and Raffaella Sesana. "Geodesic domes for planetary exploration". In: *Curved and Layered Structures* 7.1 (2020), pp. 215–225. DOI: 10.1515/cls-2020-0018.

[39] Luca Valdarno et al. "Thermo-mechanical Analysis and Design of an Additive Manufactured Evaporator for a Two-Phase Mechanically Pumped Loop". In: *50th International Conference on Environmental Systems*. July. 2021.

[40] Enrico Ossola et al. "Fabrication defects and limitations of AlSi10Mg lattice structures manufactured by Selective Laser Melting". In: *Proceedings of the Institution of Mechanical Engineers, Part L: Journal of Materials: Design and Applications* Accepted for publication (2021).

[41] Krishan K. Khurana et al. "Electromagnetic Induction from Europa's Ocean and the Deep Interior". In: *Europa*. University of Arizona Press, 2017, pp. 571–586. DOI: 10.2307/j.ctt1xp3wdw.30.

[42] L. Iess et al. "The Gravity Field and Interior Structure of Enceladus". In: *Science* 344.6179 (Apr. 2014), pp. 78–80. ISSN: 0036-8075. DOI: 10.1126/science.1250551.

[43] Konstantinos Konstantinidis et al. "A lander mission to probe subglacial water on Saturn's moon Enceladus for life". In: *Acta Astronautica* 106 (2015), pp. 63–89. DOI: 10.1016/j.actaastro.2014.09.012.

[44] Robert Gershman, Erik Nilsen, and Robert Oberto. "Europa Lander". In: *Acta Astronautica* 52.2-6 (2003), pp. 253–258. ISSN: 00945765. DOI: 10.1016/S0094-5765(02)00164-9.

[45] K.P. Hand et al. "Report of the Europa Lander Science Definition Team". In: (2017), p. 264.

[46] Hari Nayar et al. "Surface mobility on ocean worlds". In: *IEEE Aerospace Conference Proceedings* (2017), pp. 1–10. ISSN: 1095323X. DOI: 10.1109/AERO.2017.7943900.

[47] Mircea Badescu et al. "Sampling Tool Concepts for Enceladus Lander In-Situ Analysis". In: *IEEE Aerospace Conference Proceedings* 2019-March (2019), pp. 1–12. DOI: 10.1109/AERO.2019.8741568.

[48] Hari Nayar et al. "Long reach sampling for ocean worlds". In: *IEEE Aerospace Conference Proceedings* (2017), pp. 1–7. DOI: 10.1109/AERO.2017.7943680.

[49] W. Zimmerman et al. "A radioisotope powered cryobot for penetrating the Europan ice shell". In: *AIP Conference Proceedings* 552 (2001), pp. 707–715. ISSN: 0094243X. DOI: 10.1063/1.1357997.

[50] Marius Wirtz and Marc Hildebrandt. "IceShuttle teredo: An ice-penetrating robotic system to transport an exploration auv into the ocean of Jupiter's moon Europa". In: *Proceedings of the International Astronautical Congress, IAC* October (2016). ISSN: 00741795.

[51] William Stone et al. "Project VALKYRIE: Laser-Powered Cryobots and Other Methods for Penetrating Deep Ice on Ocean Worlds". In: *Outer Solar System*. Ed. by Viorel Badescu and Kris Zacny. Cham: Springer International Publishing, 2018, pp. 47–165. ISBN: 978-3-319-73844-4. DOI: 10.1007/978-3-319-73845-1_4.

[52] Thomas Cwik, Wayne Zimmerman, and Miles Smith. "An architecture for a nuclear powered Cryobot to access the oceans of icy worlds". In: *Nuclear and Emerging Technologies for Space, American Nuclear Society Topical Meeting* (2019).

[53] Ryan S. Park et al. "Improved detection of tides at Europa with radiometric and optical tracking during flybys". In: *Planetary and Space Science* 112 (July 2015), pp. 10–14. DOI: 10.1016/j.pss.2015.04.005.

[54] Sandra E. Billings and Simon A. Kattenhorn. "The great thickness debate: Ice shell thickness models for Europa and comparisons with estimates based on flexure at ridges". In: *Icarus* 177.2 (2005), pp. 397–412. DOI: 10.1016/j.icarus.2005.03.013.

[55] Louise M. Prockter and Robert T Pappalardo. "Europa". In: *Encyclopedia of the Solar System*. Third Edit. Elsevier, 2014, pp. 793–811. ISBN: 9780124158450. DOI: 10.1016/B978-0-12-415845-0.00036-0.

[56] Thomas M. Orlando, Thomas B. McCord, and Gregory A. Grieves. "The chemical nature of Europa surface material and the relation to a subsurface ocean". In: *Icarus* 177.2 (Oct. 2005), pp. 528–533. ISSN: 00191035. DOI: 10.1016/j.icarus.2005.05.009.

[57] Jean-pierre Fleurial et al. "Notional Concept of Operations and System Capability Definition for Enabling Scientific Ocean Access Missions on Icy Worlds Architectures". In: *EPSC-DPS Joint Meeting 2019*. Vol. 13. Geneva, Switzerland, 2019, pp. 4–5.

[58] HJ Melosh et al. "The temperature of Europa's subsurface water ocean". In: *Icarus* 168.2 (2004), pp. 498–502.

[59] *Structural design and test factors of safety for spaceflight hardware*. Tech. rep. Technical Report NASA-STD-5001, NASA, 1996.

[60] *NASA SP-8007 Buckling of Thin-Walled Circular Cylinders*. Tech. rep. 1968.

[61] Carl T.F. Ross. "Shell instability of pressure vessels". In: *Pressure Vessels*. Elsevier, 2011, pp. 100–164. DOI: 10.1533/9780857092496.100.

[62] Warren C Young and Richard G Budnyas. *Roark's formulas for stress and strain*. New York: McGraw-Hill, 2002.

[63] Alexander T Basilevsky and James W Head. "The surface of Venus". In: *Reports on Progress in Physics* 66.10 (2003), p. 1699. DOI: 10.1088/0034-4885/66/10/R04.

[64] M. J. Way et al. "Was Venus the first habitable world of our solar system?" In: *Geophysical Research Letters* 43.16 (2016), pp. 8376–8383. DOI: 10.1002/2016GL069790.

[65] Michael Amato and David Williams. "Accessing the Venus Lower Atmosphere and Surface - from Venera and Pioneer Venus to VISE and VITaL". In: *Inner Solar System: Prospective Energy and Material Resources*. Ed. by Viorel Badescu and Kris Zacny. Cham: Springer International Publishing, 2015, pp. 71–100. DOI: 10.1007/978-3-319-19569-8_4.

[66] Ralph D. Lorenz, David Crisp, and Lyle Huber. "Venus atmospheric structure and dynamics from the VEGA lander and balloons: New results and PDS archive". In: *Icarus* 305 (2018), pp. 277–283. ISSN: 0019-1035. DOI: https://doi.org/10.1016/j.icarus.2017.12.044.

[67] Asif A Siddiqi. *Beyond Earth: A Chronicle of Deep Space Exploration, 1958-2016*. NASA, Office of Communications, NASA History Division, 2018.

[68] VEXAG GOI Focus Group. *Venus Goals, Objectives, and Investigations*. Tech. rep. 2019.

[69] VEXAG GOI Technology Group. *Venus Technology Plan*. Tech. rep. 2019.

[70] Micheal L. Adams et al. *Venus Mobile Explorer*. Tech. rep. 2009.

[71] Martha S. Gilmore et al. *Venus Intrepid Tessera Lander*. Tech. rep. 2010.

[72] JL Hall et al. *Venus Flagship Mission Study: Final Report of the Venus Science and Technology Definition Team*. Tech. rep. 2012.

[73] MV Keldysh. "Venus exploration with the Venera 9 and Venera 10 spacecraft". In: *Icarus* 30.4 (1977), pp. 605–625. DOI: `10.1016/0019-1035(77)90085-9`.

[74] Kuan-Lin Lee and Calin Tarau. "24 Hour Consumable-based Cooling System for Venus Lander". In: 49th International Conference on Environmental Systems. 2019.

[75] Michael Pauken et al. "Pressure vessel technology developments". In: *4th International Planeatry Probe Workshop*. Pasadena, CA, 2006.

[76] David Bushnell. *Computerized buckling analysis of shells*. Vol. 9. Springer Science & Business Media, 2012.

[77] RL Carlson, RL Sendelbeck, and NJ Hoff. "Experimental studies of the buckling of complete spherical shells". In: *Experimental Mechanics* 7.7 (1967), pp. 281–288.

[78] L Berke and RL Carlson. "Experimental studies of the postbuckling behavior of complete spherical shells". In: *Experimental Mechanics* 8.12 (1968), pp. 548–553.

[79] J. Blachut, G. D. Galletly, and D. N. Moreton. "Buckling of near-perfect steel torispherical and hemispherical shells subjected to external pressure". In: *AIAA Journal* 28.11 (1990). DOI: `10.2514/3.10506`.

[80] Jan Blachut. "Buckling of multilayered metal domes". In: *Thin-Walled Structures* 47.12 (Dec. 2009), pp. 1429–1438. DOI: `10.1016/j.tws.2009.07.011`.

[81] Binbin Pan, Weicheng Cui, and YS Shen. "Experimental verification of the new ultimate strength equation of spherical pressure hulls". In: *Marine structures* 29.1 (2012), pp. 169–176. DOI: `10.1016/j.marstruc.2012.05.007`.

[82] Alessia Meschini et al. "Pressure hull design methods for unmanned underwater vehicles". In: *Journal of Marine Science and Engineering* 7.11 (2019). DOI: `10.3390/jmse7110382`.

[83] Anna Lee et al. "The geometric role of precisely engineered imperfections on the critical buckling load of spherical elastic shells". In: *Journal of Applied Mechanics* 83.11 (2016), p. 111005. DOI: `10.1115/1.4034431`.

[84] Jian Zhang et al. "Buckling of stainless steel spherical caps subjected to uniform external pressure". In: *Ships and Offshore Structures* 13.7 (2018). DOI: `10.1080/17445302.2018.1459358`.

[85] Jian Zhang et al. "Study on dented hemispheres under external hydrostatic pressure". In: *Marine Structures* 74.October 2019 (2020), p. 102819. ISSN: 09518339. DOI: `10.1016/j.marstruc.2020.102819`.

[86] Sang Rai Cho et al. "Ultimate Strength Assessment of Steel-Welded Hemispheres under External Hydrostatic Pressure". In: *Journal of Marine Science and Application* (2021). DOI: `10.1007/s11804-020-00178-8`.

[87] Robert Zoelly. "Ueber ein Knickungsproblem an der Kugelschale". PhD thesis. ETH Zurich, 1915.

[88] H.N.R. Wagner, C. Hühne, and S. Niemann. "Robust knockdown factors for the design of spherical shells under external pressure: Development and validation". In: *International Journal of Mechanical Sciences* 141.January (June 2018), pp. 58–77. DOI: `10.1016/j.ijmecsci.2018.03.029`.

[89] H. N.R. Wagner et al. "On the imperfection sensitivity and design of spherical domes under external pressure". In: *International Journal of Pressure Vessels and Piping* 179.October 2019 (2020), p. 104015. DOI: `10.1016/j.ijpvp.2019.104015`.

[90] Theodore. Von Karman and Hsue-Shen Tsien. "The Buckling of Spherical Shells by External Pressure". In: *Journal of the Aeronautical Sciences* 7.2 (Dec. 1939), pp. 43–50. ISSN: 1936-9956. DOI: `10.2514/8.1019`.

[91] Hsue-Shen Tsien. "A Theory for the Buckling of Thin Shells". In: *Journal of the Aeronautical Sciences* (1942). DOI: `10.2514/8.10911`.

[92] Warner T. Koiter. "On the stability of elastic equilibrium". PhD thesis. Delft, The Netherlands: Delft University of Technology, 1945.

[93] Leon Ru-Liang Wang. "Discrepancy of experimental buckling pressures of spherical shells." In: *AIAA Journal* 5.2 (Feb. 1967), pp. 357–359. ISSN: 0001-1452. DOI: `10.2514/3.3975`.

[94] J Michael T Thompson. "The elastic instability of spherical shells". PhD thesis. Clare College, Cambridge University, Cambridge, UK, 1961.

[95] *NASA SP-8032 Buckling of Thin-Walled Doubly curved shells*. Tech. rep. 1969.

[96] T Karman. "The buckling of spherical shells by external pressure". In: *Journal of the Aeronautical Sciences* (1939).

[97] John W. Hutchinson. "Buckling of spherical shells revisited". In: *Proceedings of the Royal Society A: Mathematical, Physical and Engineering Sciences* (2016). DOI: `10.1098/rspa.2016.0577`.

[98] Francisco López Jiménez et al. "Technical Brief: Knockdown Factor for the Buckling of Spherical Shells Containing Large-Amplitude Geometric Defects". In: *Journal of Applied Mechanics* 84.3 (Mar. 2017), pp. 1–4. DOI: `10.1115/1.4035665`.

[99] Dong Yan, Matteo Pezzulla, and Pedro M. Reis. "Buckling of pressurized spherical shells containing a through-thickness defect". In: *Journal of the Mechanics and Physics of Solids* 138 (2020), p. 103923. DOI: `10.1016/j.jmps.2020.103923`.

[100] Jian Zhang et al. "Elastic-plastic buckling of deep sea spherical pressure hulls". In: *Marine Structures* 57 (2018), pp. 38–51. DOI: `10.1016/j.marstruc.2017.09.007`.

[101] Yue-lin Zhang et al. "The buckling strength of plexiglass protective shield under static water pressure". In: *Engineering Failure Analysis* 99 (May 2019), pp. 169–179. ISSN: 13506307. DOI: `10.1016/j.engfailanal.2019.02.011`.

[102] Jan Blachut. "The use of composites in underwater pressure: Hull components". In: *Buckling and Postbuckling Structures II: Experimental, Analytical and Numerical Studies*. 2018. DOI: `10.1142/9781786344335_0004`.

[103] *Eurocode 3: Design of steel structures: Strength and Stability of Shell Structures*. Tech. rep. 2007.

[104] J Michael Rotter. "Shell buckling design and assessment and the LBA-MNA methodology". In: *Stahlbau* 80.11 (2011), pp. 791–803.

[105] M Tall et al. "Elastoplastic buckling and collapse of spherical shells under combined loadings". In: *Thin-Walled Structures* 123 (2018), pp. 114–125.

[106] Binbin Pan and Weicheng Cui. *An overview of buckling and ultimate strength of spherical pressure hull under external pressure*. 2010. DOI: `10.1016/j.marstruc.2010.07.005`.

[107] Binbin Pan et al. "Further study on the ultimate strength analysis of spherical pressure hulls". In: *Marine Structures* 23.4 (2010). ISSN: 09518339. DOI: `10.1016/j.marstruc.2010.11.001`.

[108] SB Pranesh et al. "Non-linear buckling analysis of imperfect thin spherical pressure hull for manned submersible". In: *Journal of Ocean Engineering and Science* 2.4 (2017), pp. 293–300.

[109] Asghar Khan et al. "Concept design of the underwater manned seabed walking robot". In: *Journal of Marine Science and Engineering* (2019). DOI: `10.3390/jmse7100366`.

[110] R R Meyer, O P Harwood, and M B Harmon. "Isogrid design handbook". In: *NASA CR-124075* (1973).

[111] R J Bellifante and R R Meyer. "Fabrication and experimental evaluation of common domes having waffle-like stiffening. Part I-program development". In: *Douglas Report SM-47742* (1964).

[112] Anthony Freeman. "Deep space nanosats–positioned for exponential growth". In: *Proc. Small Satellites, System & Services (4S) Symposium* (2016), pp. 1–15.

[113] D Bugby et al. "Novel Architecture for a Long-Life, Lightweight Venus Lander". In: *AIP Conference Proceedings* 1103 (2009), pp. 39–50.

[114] RM Baitimerov et al. "An investigation of high temperature tensile properties of selective laser melted ti-6al-4v". In: *Proceedings of the 3rd International Conference on Progress in Additive Manufacturing.* Vol. 439. 2018, p. 444. DOI: 10.25341/D4HG6J.

[115] Anatoliy Popovich et al. "Microstructure and mechanical properties of Ti-6Al-4V manufactured by SLM". In: *Key Engineering Materials.* Vol. 651. Trans Tech Publ. 2015, pp. 677–682.

[116] Jun-Ren Zhao et al. "The relationship of fracture mechanism between high temperature tensile mechanical properties and particle erosion resistance of selective laser melting Ti-6Al-4V alloy". In: *Metals* 9.5 (2019), p. 501.

[117] Eric Sunada et al. "A Two-Phase Mechanically Pumped Fluid Loop for Thermal Control of Deep Space Science Missions". In: *46th International Conference on Environmental Systems.* July. Vienna, Austria, 2016.

[118] Richard Russell. "NASA's Plans for Development of a Standard for Additively Manufactured Components". In: *Journal of Materials Engineering and Performance* 28.4 (Apr. 2019), pp. 1924–1928. DOI: 10.1007/s11665-019-03939-x.

[119] Walter Tam, Kamil Wlodarczyk, and Gary Kawahara. "Space Propulsion 2018 Additive Manufactured Pressure Vessel Shell". In: *Space Propulsion.* May. Seville, Spain, 2018.

[120] Abdul M Haque et al. "Development of an Additive Manufactured Mass , Volume and Cost Optimised Ti-6AL-4V Fuel Tank for Microsatellite Propulsion Systems MiniTANK". In: *36th International Electric Propulsion Conference.* Vienna, Austria, 2019, pp. 1–20.

[121] Walter Tam, Kamil Wlodarczyk, and Joseph Hudak. "Additive Manufactured Pressure Vessel Development: An Update". In: *Volume 3: Design and Analysis.* Vol. 3. October. American Society of Mechanical Engineers, July 2019. DOI: 10.1115/PVP2019-94033.

[122] Torsten Fischer et al. "Fatigue cracking of additively manufactured materials-process and material perspectives". In: *Applied Sciences (Switzerland)* (2020). DOI: 10.3390/app10165556.

[123] Oraib Al-Ketan and Rashid K. Abu Al-Rub. "Multifunctional Mechanical Metamaterials Based on Triply Periodic Minimal Surface Lattices". In: *Advanced Engineering Materials* 21.10 (Oct. 2019), p. 1900524. DOI: 10.1002/adem.201900524.

[124] Eugenio Dragoni. "Optimal mechanical design of tetrahedral truss cores for sandwich constructions". In: *Journal of Sandwich Structures & Materials* 15.4 (2013), pp. 464–484.

[125] Chunlei Qiu et al. "Influence of processing conditions on strut structure and compressive properties of cellular lattice structures fabricated by selective laser melting". In: *Materials Science and Engineering A* 628 (2015), pp. 188–197. DOI: 10.1016/j.msea.2015.01.031.

[126] Angela Ferrigno et al. "The mechanical strength of Ti-6Al-4V columns with regular octet microstructure manufactured by electron beam melting". In: *Materialia* 5 (2019), p. 100232. ISSN: 2589-1529. DOI: https://doi.org/10.1016/j.mtla.2019.100232.

[127] Lu Liu et al. "Elastic and failure response of imperfect three-dimensional metallic lattices: the role of geometric defects induced by Selective Laser Melting". In: *Journal of the Mechanics and Physics of Solids* 107 (2017), pp. 160–184. DOI: 10.1016/j.jmps.2017.07.003.

[128] Asma El Elmi et al. "Experimental and numerical investigation of selective laser melting–induced defects in Ti–6Al–4V octet truss lattice material: the role of material microstructure and morphological variations". In: *Journal of Materials Research* 35.15 (2020), pp. 1900–1912. DOI: 10.1557/jmr.2020.75.

[129] Ahmed Moussa et al. "Topology optimization of imperfect lattice materials built with process-induced defects via Powder Bed Fusion". In: *Additive Manufacturing* (2020), p. 101608. DOI: https://doi.org/10.1016/j.addma.2020.101608.

[130] Panwei Jiang, Mustafa Rifat, and Saurabh Basu. "Impact of Surface Roughness and Porosity on Lattice Structures Fabricated by Additive Manufacturing-A Computational Study". In: *Procedia Manufacturing* 48 (2020). 48th SME North American Manufacturing Research Conference, NAMRC 48, pp. 781–789. DOI: https://doi.org/10.1016/j.promfg.2020.05.114.

[131] M. Suard et al. "Mechanical equivalent diameter of single struts for the stiffness prediction of lattice structures produced by Electron Beam Melting". In: *Additive Manufacturing* 8 (2015), pp. 124–131. DOI: 10.1016/j.addma.2015.10.002.

[132] F. Cabanettes et al. "Topography of as built surfaces generated in metal additive manufacturing: A multi scale analysis from form to roughness". In: *Precision Engineering* 52.October 2017 (2018), pp. 249–265. DOI: `10.1016/j.precisioneng.2018.01.002`.

[133] Xuesong Han et al. "Investigation on Selective Laser Melting AlSi10Mg Cellular Lattice Strut: Molten Pool Morphology, Surface Roughness and Dimensional Accuracy". In: *Materials* 11.3 (Mar. 2018), p. 392. DOI: `10.3390/ma11030392`.

[134] Pauline Delroisse et al. "Effect of strut orientation on the microstructure heterogeneities in AlSi10Mg lattices processed by selective laser melting". In: *Scripta Materialia* 141 (2017), pp. 32–35. DOI: `10.1016/j.scriptamat.2017.07.020`.

[135] Zhichao Dong et al. "Orientation dependency for microstructure, geometric accuracy and mechanical properties of selective laser melting AlSi10Mg lattices". In: *Journal of Alloys and Compounds* 791 (2019), pp. 490–500. DOI: `10.1016/j.jallcom.2019.03.344`.

[136] Martin Leary et al. "Selective laser melting (SLM) of AlSi12Mg lattice structures". In: *Materials and Design* 98 (2016), pp. 344–357. DOI: `10.1016/j.matdes.2016.02.127`.

[137] Radek Vrána et al. "Selective Laser Melting Strategy for Fabrication of Thin Struts Usable in Lattice Structures". In: *Materials* 11.9 (2018), p. 1763. DOI: `10.3390/ma11091763`.

[138] Théo Persenot et al. "Enhancing the tensile properties of EBM as-built thin parts: Effect of HIP and chemical etching". In: *Materials Characterization* 143.November 2017 (2018), pp. 82–93. DOI: `10.1016/j.matchar.2018.01.035`.

[139] Zahra Bagheri et al. "Compensation strategy to reduce geometry and mechanics mismatches in porous biomaterials built with Selective Laser Melting". In: *Journal of the Mechanical Behavior of Biomedical Materials* 70 (2016), pp. 17–27. DOI: `10.1016/j.jmbbm.2016.04.041`.

[140] Antonella Sola and Alireza Nouri. "Microstructural porosity in additive manufacturing: The formation and detection of pores in metal parts fabricated by powder bed fusion". In: *Journal of Advanced Manufacturing and Processing* 1.3 (2019), pp. 1–21. DOI: `10.1002/amp2.10021`.

[141] Thomas Voisin et al. "Defects-dictated tensile properties of selective laser melted Ti-6Al-4V". In: *Materials and Design* 158 (2018), pp. 113–126. DOI: `10.1016/j.matdes.2018.08.004`.

[142] Johannes Schindelin et al. "Fiji: an open-source platform for biological-image analysis". In: *Nature Methods* 9.7 (July 2012), pp. 676–682. DOI: 10.1038/nmeth.2019.

[143] Yukitaka Murakami. *Metal Fatigue- Effects of Small Defects and Nonmetallic Inclusions*. Elsevier Ltd., 2002, pp. 35–55. ISBN: 0080440649. DOI: 10.4293/108680811X13125733356710.

[144] Simone Romano et al. "Qualification of AM parts: extreme value statistics applied to tomographic measurements". In: *Materials & Design* 131 (2017), pp. 32–48. DOI: 10.1016/j.matdes.2017.05.091.

[145] Oraib Al-Ketan, Reza Rowshan, and Rashid K. Abu Al-Rub. "Topology-mechanical property relationship of 3D printed strut, skeletal, and sheet based periodic metallic cellular materials". In: *Additive Manufacturing* 19 (2018), pp. 167–183. DOI: 10.1016/j.addma.2017.12.006.

[146] L.F. Wang et al. "Enhancement in mechanical properties of selectively laser-melted AlSi10Mg aluminum alloys by T6-like heat treatment". In: *Materials Science and Engineering: A* 734 (2018), pp. 299–310. ISSN: 0921-5093. DOI: 10.1016/j.msea.2018.07.103.

[147] Luca Valdarno et al. "Heat Transfer Modeling in the Wick Structure of an Innovative Evaporator for a Two-Phase Mechanically Pumped Loop". In: *International Conference on Environmental Systems*. July. 2020. URL: https://hdl.handle.net/2346/86305.

This Ph.D. thesis has been typeset by means of the T_EX-system facilities. The typesetting engine was pdfLaT_EX. The document class was `toptesi`, by Claudio Beccari, with option `tipotesi=scudo`. This class is available in every up-to-date and complete T_EX-system installation.